Modeling and Simulation of cracks and fractures with peridynamics in brittle materials

Dissertation

zur

Erlangung des Doktorgrades (Dr. rer. nat.)

der

Mathematisch-Naturwissenschaftlichen Fakultät

der

Rheinischen Friedrich-Wilhelms-Universität Bonn

vorgelegt von

Patrick Diehl

aus

Engen

Bonn 2016

Angefertigt mit Genehmigung der Mathematisch-Naturwissenschaftlichen Fakultät
der Rheinischen Friedrich-Wilhelms-Universität Bonn

1. Gutachter: Prof. Dr. Marc Alexander Schweitzer

2. Gutachter: Prof. Dr. Daniel Peterseim

Tag der Promotion: 27.01.2017

Erscheinungsjahr: 2017

To Sylvia, Astrid and Marisa

Zusammenfassung

Diese Arbeit behandelt die Modellierung und Simulation von Brüchen und Rissen in spröden Festkörpern mittels Peridynamik. Aus Sicht der Industrie sind spröde Materialien, wie z. B. keramische Werkstoffe, von großem Interesse. Diese Werkstoffe sind ein essentieller Bestandteil von Batterien, die in Elektroautos oder in modernen Flugzeugen Anwendung finden. Eine präzise Vorhersage von Brüchen und Rissen während eines Aufpralls oder Unfalls sind für die Sicherheit dieser Batterien von großer Wichtigkeit.

Als grundlegende Gleichung wird in dieser Arbeit die Peridynamik-Theorie (PD), eine nicht lokale Verallgemeinerung der Kontinuumsmechanik, untersucht. Im Gegensatz zu anderen Methoden der klassischen Kontinuumsmechanik wird das Materialversagen direkt in der grundlegenden Gleichung modelliert. Somit sind keine zusätzlichen externen Kriterien für die Initiierung und die Ausbreitung der Risse erforderlich. Gerade die Modellierung der Entstehung von Rissen ist eine Stärke dieses Modells.

Unter dem Aspekt der Modellierung der Entstehung und Ausbreitung von Rissen werden zwei verbindungsbasierte Peridynamik-Modelle für lineare isotrope elastische Materialien betrachtet. Ein wichtiger Aspekt ist die Bestimmung von Materialeigenschaften mittels Energiegleichheit gemäß der linearen Elastizitätstheorie.

Die Peridynamik beschreibt eine Modell, das für die Simulation diskretisiert werden muss. In der Literatur werden Verfahren wie die Galerkin-Finite-Elemente-Methode oder die Gauß-Quadratur postuliert. Unter Berücksichtigung der Komplexität und der einfachen Parallelisierbarkeit der Implementierung wird in dieser Arbeit ein Kollokationsansatz gewählt. Ein Bestandteil, der großen Einfluss auf die Komplexität hat, ist die Nachbarschaftssuche in Punktwolken. Ein Beitrag dieser Arbeit ist die effiziente auf Suchalgorithmen basierte Softwarebibliothek FNSG für die Nachbarschaftssuche in generischen Punktwolken auf Grafikkarten (GPU).

Um die volle Rechenleistung moderner Hochleistungsrechner komplett auszulasten, ist eine Kombination von Prozessoren und Beschleunigerkarten essentiell. Hierfür wurde das CUDA-Programmiermodell für GPU in das High-Performance-ParallelX-Framework integriert. Dies erlaubt eine nahtlose Synchronisation des Datenflusses und der Berechnung zwischen den Prozessoren und den GPUs.
Um die Simulationsdaten mit experimentellen Daten vergleichen zu können, ist die Extraktion von Fragmenten und Stresswellen von Interesse. Hierzu werden zwei

Nachbearbeitungstechniken für die Extraktion von Fragmenten und Stresswellen aus punktbasierten Simulationsdaten aufgeführt.

Abschließend werden drei numerische Resultate für die Entstehung und Ausbreitung von Rissen betrachtet. Erstens die Ausbreitung von Stoßwellen anhand des EOI-Experiments. Die in der Simulation extrahierte Geschwindigkeit der Wellenfront wird mit der gemessenen Geschwindigkeit im Experiment verglichen.
Zweitens wird für einen weitreichenden Bereich von Materialien die kritische Zugkraft für den Fall *I* der Rissöffnungsarten dem theoretischen Wert aus der linear-elastischen Bruchmechanik (LEBM) gegenübergestellt.
Drittens werden die elastischen Materialeigenschaften, wie diese im Experiment im Labor bestimmt werden, vergleichsweise in der Simulation bestimmt. Hier liegt der Fokus auf der Reproduktion des identischen Materialverhaltens.

Generell ist die verbindungsbasierte Peridynamik-Theorie mit der gewählten Diskretisierung für die Modellierung und Simulation von Brüchen und Rissen in spröden Festkörpern geeignet. Allerdings beeinflusst die Wahl der Diskretisierungsparameter, die Maschenweite und der Radius des Nachbarschaftsballs, insbesondere deren Verhältnisse, das Ergebnis signifikant. Für die ersten beiden numerischen Resultate konnten die Werte aus dem Experiment oder der LEBM bis auf kleine Fehler reproduziert werden. Im dritten Resultat war die Reproduktion des komplexen Materialverhaltens aus dem Experiment nicht mit dem simplen verbindungsbasierten erweichenden Materialmodell nicht möglich. Hier sollte die Anwendung von komplizierteren Materialmodellen oder die zustandsbasierte Peridynamik-Theorie in Betracht gezogen werden. Eine offene Frage bleibt die geeignete Wahl des Verhältnisses der Diskretisierungsparameter in der Simulation.

Contents

1.Introduction

Nowadays, ceramic materials are an essential component of batteries for electric cars and modern airplanes. Several fires after an accident or a crash where an electric car was involved have been reported [Gre16; Jen13; Ohn13]. One key element of this kind of battery is the safety of its ceramic core during a crash. Here, the precise approximation of the evolution of the damage after the impact and the wave propagation is important to analyze the safety of the battery. The initiation of cracks is especially essential, because the core is normally not damaged and thus has no initial cracks. The simulation of the initiation and growth of cracks is quite challenging.

Different approaches for the modeling and simulation of cracks and fractures can be found in literature. At the beginning of Chapter 2 a brief overview of approaches based on classical continuum mechanics (CCM) and non-local models is given. In Section 2.1 we quickly review CCM before we introduce peridynamics (PD), one of these non-local approaches, and identify the core difference between these two approaches.
One key difference is that for CCM-based approaches an external criterion is needed for the growth of cracks. In addition, the initiation of cracks is still an unsolved issue with regards to these approaches. Peridynamics includes a notion of failure directly in its governing equations and no external criterion is needed for the initiation and growth of cracks.

Figure 1.1 shows examples for the simulation of cracks (a) and wave propagation (b) with bond-based peridynamics material models. Note that in all simulations, the geometry had no pre-existing cracks. Due to the fact that no external criterion is needed for the initiation and growth of cracks, which is an important feature, we focus on bond-based material models in this thesis. Therefore, two bond-based materials models are introduced in Section 2.3. The bond-based peridynamic Prototype Microelastic Brittle material and the bond-based softening material model. Note, that both models demonstrate the notion of failure different, but for both models, the model material parameters can be related to material parameters from classical theory via energy equivalence.

Peridynamics is a model and needs to be discretized for the simulations. Different discretizations, which are quickly summarized at the beginning of Chapter 3 can

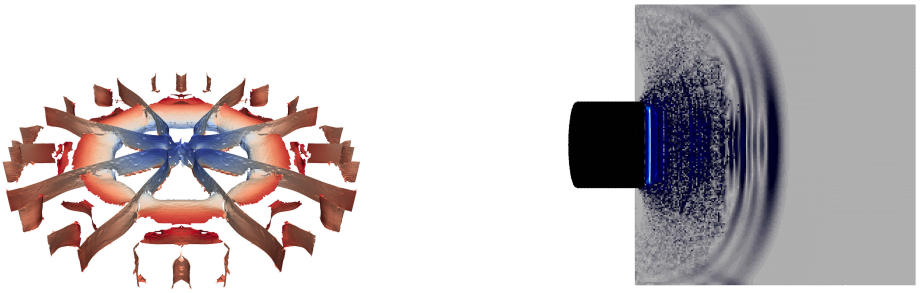

(a) Extracted crack surfaces in a thin plate. **(b)** Waves after impact damage in ALON.

Figure 1.1.: Examples for cracks and wave propagation in bond-based peridynamic simulations.

be found in literature. We focus on the EMU nodal discretization (EMU ND) in this thesis due to existing efficient load distribution schemes, see Section 3.1. In Section 3.3 the bond-based peridynamic Discrete Prototype Microelastic Material (DPMB) material models is introduced. Remember, that PD is a model, which can be discretized in various ways and the PMB material model was adjusted to the EMU ND.

Now, we have a discrete PD models, the focus is on the implementation of these models. One computational intensive part of the EMU ND is the neighbor search in node clouds. However, to deal with very large node clouds, which are necessary for accurate simulations, the neighborhoods need to be computed in parallel. In Section 4.1 an efficient sorting-based neighbor search algorithm is extended for general-purpose computing on graphics processing units (GPGPU) using the Compute Unified Device Architecture (CUDA).
One challenging part of GPGPU is the synchronization of the computing on the GPU and writing the simulation results to the hard disk with the GPU. Here, special care by the programmer has to be taken. To circumvent the data management between the host memory and the device memory, and the synchronization of kernel execution and data, we integrated CUDA into High Performance ParallelX framework. Within this framework, a CPU and a CUDA device have the same API and thus, all GPU operations are represented as a asynchronous task like the parallel tasks on the CPU, see Section 4.2.

Comparing node-based simulations with experimental data is rather challenging, because most experiments do not provide the measured data in detail at this level.

One example is the distribution of the fragment sizes or their volume. To compare node-based simulation additional information need to be extracted from the node-based simulation. For the comparison with fragmentation experiments, we extended a clustering algorithm for node-based simulations data. Here, our algorithm extracts fragments and the corresponding histograms for the fragment size or their volume, see Section 4.3.1. Therefore, comparison with these kinds of experiments is now possible. Another important aspect for understanding the damage after an impact is the propagation and reflection of waves. Here, we provide a technique for the visualization of stress waves in Section 4.3.2.

To verify the bond-based material models and our implementations, we compared them with experimental data and the LEFM theory. In Section 5.1 we compared the obtained speed at the wave front with the one measured in the Edge-On impact experiment for Aluminiumoxynitrid (ALON).
The critical traction for Mode *I* crack opening for a wide range of materials from polymethyl methacrylate (PMMA) up to titanium alloy was compared with the one prescribed by LEFM theory in Section 5.2.
Remember that the bond-based peridynamic softening model models damage with a new approach. For the PMB model, different studied are provided in literature. We numerically validated the softening model for small deformations in Section 5.3. Here, the material behavior of the Poisson ratio of PMMA is compared with the one measured in an actual tensile test.

The aim of this thesis is to study the applicability of bond-based peridynamic discretized with the EMU nodal discretization for modeling and simulating cracks and fractures in brittle materials, particularly, the initiation of cracks, which is a important feature of PD.

Summary of own contributions

- We present the energy equivalence for the bond-based peridynamic softening model with the classic elasticity theory.
- We provided two post-processing techniques for the extraction of fragments and stress waves of generic node-based simulation data.
- We adapted and extended an efficient and general sorting based approach for neighbor search for general-purpose computing on graphics processing units.

- We outlined the integration of the CUDA programming scheme to the High Performance ParallelX framework (HPX). For providing asynchronous data transfers and kernel execution on GPUs while tasks are concurrently executed on the main cores.
- We showed the comparison of simulations with experimental data, e.g. EOI experiment and tensile test, as well as, the comparison with the prescribed critical traction from Linear Elastic Fracture Mechanics.

Software

The following software packages are the results of this thesis:

- Fast neighbor search on GPU (FNSG) [DT16], a efficient and general sorting based approach for finding neighbors in large point clouds (see Section 4.1).
- HPXCL [Ste16], asynchronous integration of CUDA in the execution graph of High Performance ParallelX framework (HPX), a general purpose C++ run time system for parallel and distributed applications of any scale (see Section 4.2).
- PeriHPX, a generic implementation of the bond-based peridynamic using the EMU nodal discretization within HPX. All simulations in Chapter 5.3 for the softening model were carried out with this code.

Publications

Parts of this thesis are already published in these contributions:

- P. Diehl and M. A. Schweitzer. “Efficient Neighbor Search for Particle Methods on GPUs.” In: *Meshfree Methods for Partial Differential Equations VII*. ed. by M. Griebel and M. A. Schweitzer. Vol. 100. Lecture Notes in Computational Science and Engineering. Springer, 2014
- P. Diehl and M. A. Schweitzer. “Simulation of wave propagation and impact damage in brittle materials using peridynamics.” In: *Recent Trends in Computational Engineering – CE2014*. Ed. by Miriam Mehl, Manfred Bischoff, and Michael Schäfer. Lecture Notes in Computational Science and Engineering. Springer, 2015

- Patrick Diehl et al. “Bond-based peridynamics: a quantitative study of Mode I crack opening.” In: *International Journal of Fracture* (2016), pp. 1–14. ISSN: 1573-2673
- Patrick Diehl et al. “Extraction of fragments and waves after impact damage in particle-based simulations.” In: *Meshfree Methods for Partial Differential Equations*. Ed. by Michael Griebel and Marc Alexander Schweitzer. Springer, accepted

Acknowledgments

I would like to take this opportunity to thank all the people who have contributed to the completion of my thesis. Firstly, I would like to thank my advisor Prof. Dr. Marc Alexander Schweitzer for the opportunity to work on this topic and for the insightful discussions and advice. Furthermore, I would like to thank Prof. Dr. Daniel Peterseim for his advice as the second referee. For the work on the softening model, I would like to thank Prof. Robert Lipton for introducing me to this model and for his helpful discussions during my visit to Louisiana State University in the summer of 2015. I would also like to thank Hannes Schulz, Siggi Langauf, H.M., Dr. Tobias Mauck, and Monir Zouaoui for proofreading parts of the thesis. And not to forget all my collaborators, Fabian Franzelin, Prof. Dr. Dirk Pflüger and Eyad Said for the discussions and helpful remarks.

For the computational results, I would like to thank the operators at the INS for the great effort in providing the infrastructure to run all these simulations. Lastly, I would like to thank Sylvia and my family for their constant support and positive influence.

Outline

The remainder of this thesis is structured as follows:

- Section 2 **Model**: In Section 2.1 a brief introduction to classical continuum mechanics (CCM) and linear elasticity theory is given. In Section 2.2 the bond-based peridynamics (PD), a non-local generalization of continuum mechanics

is summarized. Next, in Section 2.3 two bond-based PD material models are introduced.

- Section 3 **Discretization**: A brief summary of possible discretization approaches for peridynamics, with the focus on the EMU nodal discretization (EMU ND) in Section 3.1. This discretization approach due to efficient load distributions schemes is used for all simulations in Section 5. In Section 3.2 a literature review for well-posed and consistent PD solutions and asymptotically compatible discretizations schemes is given. In Section 3.3 the bond-based peridynamics Prototype Microelastic Brittle (PMB) material model is adjusted to the EMU ND.
- Section 4 **Implementation and Post-processing**: In Section 4.1 a general sorting-based approach for the neighbor search on Graphics Processing Unit (GPU) is described. In Section 4.2 the implementation for a seamless integration of the Compute Unified Device Architecture (CUDA) into the High Performance ParallelX framework (HPX) is outlined. In Section 4.3 two techniques for post-processing of PD simulations are presented. First, in Section 4.3.1 a technique for the extraction of fragments from the node-based simulations is presented. Second, in Section 4.3.2 the visualization of stress waves after impact damage is shown.
- Section 5 **Numerical results**: In Section 5.1 the obtained speed at the wave front is compared with the measurements of the Edge-On impact (EOI) experiment. Here, the simulation results for the bond-based PMB material and the bond-based DPMB material are compared with experimental data. In Section 5.2 the critical traction for Mode I crack opening is compared with the critical traction prescribed by Linear Elastic Fracture Mechanics (LEFM) for a wide range for materials. In Section 5.3 a numerical verification for a bond-based softening model (SM) model for small deformations with respect to the theory in Section 2.3.2 is presented.
- Section 6 **Concluding remarks**: Summary of the presented results and some comments on areas of future research.

2.Model

The classical theory of continuum mechanics (CCM) is based on locality and assumes that a material point exchanges mass, momentum, and energy, only with its closest neighbors via contact forces. In CCM the so-called stress and strain are proportional to the spatial derivatives of the displacement. At cracks and fractures the displacement is discontinuous and thus the governing equations of CCM are not applicable there.

To model cracks and fractures with the classical continuum theory a pre-existing crack is essentially treated as an internal boundary. In addition, at the crack tip a supplementary equation is established to postulate a law for the crack growth. An essential work for this approach is the Linear Elastic Fracture Mechanics (LEFM) theory by Griffith [Gri21].

Employing the Finite Element Method (FEM) for the approximation [Arg+79; Red05], delivers robust solutions for the stress field even for complex geometries with general loading conditions. An issue is that FEM with traditional elements requires a re-meshing, the domain and its boundary become time-dependent, after each crack growth. As a result for the crack development being described with a priori criteria, the solution of the problem of multiple interacting cracks with traditional finite elements is challenging.

To overcome these difficulties the eXtended Finite Element Method (XFEM)[MDB99; BB99], a method for modeling and simulating cracks and fractures without re-meshing was introduced. In this approach, the classical FEM approximation is extended via so-called enrichment functions [MB96] that encode special features of the solution, such as discontinuities and singularities. For XFEM external criteria for the crack growth are required too, but the computationally expensive re-meshing is avoided.

Even with all these developments, the modeling and simulation of cracks and fractures is still a major challenge with CCM based approaches. Furthermore, the initiation of cracks remains an unsolved issue [MO14].

Another approach to deal with this challenging applications is in principle to model cracks with inter-atomic forces as in atomistic lattice models [ML93; MG95] or molecular dynamics (MD) [AW59]. In these models no external criterion is needed

for the crack growth. With respect to the discretization large-scale atomistic simulations are computationally expensive due to the very small time step size. Thus, it is presently not feasible to simulate large structures, e.g. the wing of an airplane, with atomistic techniques.

A connection between classical (local) continuum mechanics and molecular dynamics are the non-local theories [Krö67; EE72; Sel+09]. In these mathematical models the material points interact with all other material points within a finite interaction zone. The finite interaction zone is very important for modeling the branching of cracks tips [ZM02], because this phenomenon does not depend solely on the local deformation or local stress.

Peridynamics (PD) is one of these non-local theories [Sil00]. PD models non-linear materials using the displacement only. For the modeling of the governing equation, an integral equation instead of a partial differential equation as in CCM is used. Like molecular dynamics or atomistic lattice models, PD includes a notion of failure in the governing equations. Therefore, no external criterion is needed for the initiation and growth of cracks within peridynamics. This thesis focuses on modeling and simulating cracks and fractures in brittle materials with peridynamics. For more details about the overview of non-local models see [MO14; SP16].

In the following let us quickly review CCM before we introduce PD to identify the core difference of the approaches.

2.1. Classical continuum mechanics

The kinematics of a continuum [EGK11; Bra03; Red13] describe the temporal deformation of a continuum, without addressing the acting external forces which cause the deformation. The prerequisite for describing the kinematics of a continuum is that the continuum is defined as an open subset of $\mathbb{R}^3$. A material point in the continuum is identified with its position $X \in \mathbb{R}^3$ in the so-called reference configuration $\Omega_0 \subset \mathbb{R}^3$.

The reference configuration Ω_0 is open and coherent and refers to the shape of the continuum at rest with no internal forces.

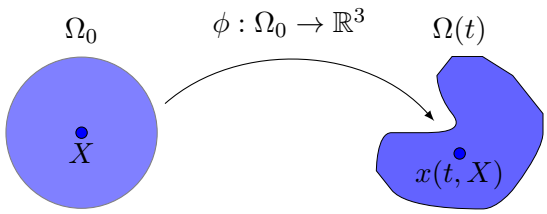

Figure 2.1.: The continuum in the reference configuration Ω_0 and after the deformation $\phi : \Omega_0 \to \mathbb{R}^3$ with $\det(\text{grad } \phi) > 0$ in the current configuration $\Omega(t)$ at time t.

The deformation $\phi : [0, T] \times \mathbb{R}^3 \to \mathbb{R}^3$ of a material point X in the reference configuration Ω_0 to the so-called current configuration $\Omega(t)$ is given by

$$\phi(t, X) := id(X) + u(t, X) = x(t, X) \tag{2.1}$$

where $u : [0, T] \times \mathbb{R}^3 \to \mathbb{R}^3$ refers to the displacement

$$u(t, X) := x(t, X) - X\,. \tag{2.2}$$

Figure 2.1 shows two different types of coordinates X, the so-called Lagrangian coordinate and $x(t, X)$, the so-called Eulerian coordinate. Here, the assumption $\det(\text{grad } \phi) > 0$ is made so that a positive volume of a subset of Ω_0 is still positive after the deformation ϕ. The deformation ϕ is locally injective.

The stretch $s : [0, T] \times \mathbb{R}^3 \times \mathbb{R}^3 \to \mathbb{R}^3$ between the material point X and the material point X' after the deformation ϕ in the configuration $\Omega(t)$ is defined by

$$s(t, X, X') := \phi(t, X') - \phi(t, X)\,. \tag{2.3}$$

Using a Taylor expansion of s yields

$$s(t, X, X') \approx \text{grad } \phi \cdot (X' - X) + o\,(X' - X) \tag{2.4}$$

and the Euclidean norm of the stretch $\|s\|$ between to material points X and X' can be written as

$$\begin{aligned} \|\phi(t, X') - \phi(t, X)\|^2 &\approx \|\text{grad } \phi \cdot (X' - X)\|^2 + o\left(\|(X' - X)\|^2\right) \\ &\approx (X - X')^T \text{grad } \phi^T \text{grad } \phi (X' - X) + o\left(\|(X' - X)\|^2\right)\,. \end{aligned} \tag{2.5}$$

The first term essentially determines the local changes of the length, which motivates the introduction of the right Cauchy–Green strain tensor $C \in \mathbb{R}^{3,3}$

$$C(\phi) := \text{grad } \phi^T \text{grad } \phi \,. \tag{2.6}$$

Moreover, the strain tensor $E \in \mathbb{R}^{3,3}$ is defined as

$$E(\phi) := \frac{1}{2} \left(C(\phi) - \mathbb{I} \right) , \tag{2.7}$$

which evaluates to zero in the case of no deformation, i.e. $\phi = id$. With (2.1) and (2.6) the strain E can be rewritten in matrix notation in terms of the displacement u

$$E_{ij} = \frac{1}{2} \left(\frac{\partial u_i}{\partial x_j} + \frac{\partial u_j}{\partial x_i} \right) + \frac{1}{2} \sum_k \frac{\partial u_i}{\partial x_k} \frac{\partial u_j}{\partial x_k} \,. \tag{2.8}$$

Assuming the most simple material model, the isotropic linear Hooke's law, the stress tensor T is given by

$$T(E) := \lambda tr(E) \mathbb{I} + 2\mu E \tag{2.9}$$

with λ and μ denoting the Lamé parameters, which are related to the Young modulus $\mathtt{E}$ and Poisson ratio ν of the considered material via

$$\begin{aligned} \nu &= \frac{\lambda}{2(\lambda + \mu)} \,, \qquad \mathtt{E} = \frac{\mu(3\lambda + 2\mu)}{\lambda + \mu} \,, \\ \lambda &= \frac{\mathtt{E}\nu}{(1+\nu)(1-2\nu)} \,, \quad \mu = \frac{\mathtt{E}}{2(1+\nu)} \,. \end{aligned} \tag{2.10}$$

Now, the stress tensor T (2.9) can be rewritten with respect to $\mathtt{E}$ and ν as

$$T(E) := \frac{\mathtt{E}\nu}{(1+\nu)(1-2\nu)} tr(E) \mathbb{I} + \frac{\mathtt{E}}{(1+\nu)} E \,. \tag{2.11}$$

Furthermore, the linear momentum

$$p := m \cdot \dot{X} \tag{2.12}$$

where m denotes the mass, and $\dot{X}$ the velocity of the material point X is a important object of interest in CCM. The force F applied to the material point X is proportional to the change of momentum

$$\mathrm{F} = \dot{p} = m \cdot \frac{d\dot{X}}{dt} = m \cdot \ddot{X} = m \cdot \ddot{u}\,. \tag{2.13}$$

This is Newton's second law: *force equals mass times acceleration*. The conservation of linear momentum with respect to the reference configuration Ω_0 is defined by

$$\frac{d}{dt} \int\limits_{\Omega_0} \varrho \frac{\partial}{\partial t} u \, dx = \int\limits_{\Omega_0} g \, dx + \int\limits_{\partial\Omega_0} \sigma n \, ds_x \tag{2.14}$$

where ϱ denotes the material density and g a volume force density and states that

$$\int\limits_{\Omega_0} \left(\varrho \frac{\partial^2}{\partial t} u - \operatorname{div} \sigma - g \right) dx = 0 \quad \text{for any } \Omega_0 \supset \Omega \tag{2.15}$$

which yields

$$\frac{\partial}{\partial t} u - \operatorname{div} \sigma = g \quad \text{in } \Omega\,. \tag{2.16}$$

Linear elasticity theory

For small deformations the quadratic terms in the strain (2.8) can be neglected to obtain the infinitesimal strain

$$\varepsilon_{ij}(u) := \frac{1}{2} \left(\frac{\partial u_i}{\partial x_j} + \frac{\partial u_j}{\partial x_i} \right) \tag{2.17}$$

and (2.11) becomes

$$\sigma_{ij}(u) = \lambda \, (\operatorname{div} u) \, \delta_{ij} + 2\mu \varepsilon_{ij}(u)\,. \tag{2.18}$$

The stress (2.18) can be written in a general tensor form with the so-called Hookean tensor $\mathbb{C} \in \mathbb{R}^{d,d,d,d}$ as

$$\sigma_{ij}(u) = \mathbb{C}_{ijkl} \varepsilon_{kl}(u) \tag{2.19}$$

with

$$\mathbb{C}_{ijkl} = \lambda\delta_{ij}\delta_{kl} + \mu(\delta_{ik}\delta_{jl} + \delta_{il}\delta_{jk})\,. \tag{2.20}$$

Now, with respect to (2.13) and (2.16) the force F in CCM is

$$\mathrm{F} = m \cdot \ddot{u} = \text{div}\ \sigma(u) = \text{div}\ \mathbb{C}(u)\,. \tag{2.21}$$

The hyperbolic system of partial differential equations for linear elasticity in its simplest form is given by

$$\varrho\frac{\partial^2}{\partial t}u - \mu\Delta u - (\lambda+\mu)\,\text{grad div}\ u = g \tag{2.22}$$

and with (2.10) the two Lamé parameters can be substituted with E and ν

$$\varrho\frac{\partial^2}{\partial t}u - \frac{\mathtt{E}}{2(1+\nu)}\Delta u - \frac{\mathtt{E}}{2(1+\nu)(1-2\nu)}\,\text{grad div}\ u = g\,. \tag{2.23}$$

Fore more details see [EGK11; Bra03]. One of the limitations of elasticity theory is the initiation of cracks that is still a major challenge of this theory. The governing equation (2.23) is a hyperbolic system of PDEs and the strain and stress, which are essentially derivatives of the displacement are undefined at discontinuities. For the growth of cracks additional external criteria, as in LEFM, are introduced as separate equations and are not part of the governing equation.

In an alternative formulation of continuum mechanics, the so-called peridynamics (PD), this issue is circumvented. PD includes a notion of failure directly in the governing equations and can thus model the initiation of a crack directly.

In the following, the governing equations of peridynamics are introduced and briefly reviewed, see [Sil00; Sil16a] for details.

2.2. Peridynamics

Peridynamics (PD) [Sil00] is a non-local generalization of continuum mechanics, with a focus on discontinuous displacements as they arise in fracture mechanics.

Peridynamics models cracks and fractures on a mesoscopic scale according to Newton's second law: *force equals mass times acceleration*

$$\mathrm{F} = m \cdot a = m \cdot \ddot{X}\,. \tag{2.24}$$

Peridynamics essentially "defines" force differently from classical continuum mechanics (CCM). In CCM the force at a point X of interest is $\mathrm{F}(t, X) = \operatorname{div} \sigma(u(t, X))$ (see (2.21)) whereas in PD a material point X exchanges forces with all other material points at a finite distance. Figure 2.2 sketches this principle, where a material point X in the reference configuration Ω_0 interacts with all other material points X' inside a finite interaction zone $B_\delta(X)$. Here, the quantity of interest is a "total" force instead of the local (contact) force where only the closest neighbors are considered.

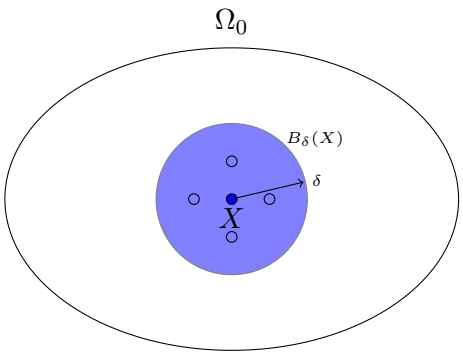

Figure 2.2.: The continuum in the reference configuration Ω_0 and the interaction zone $B_\delta(X)$ for material point X with the horizon δ.

Thus, by (2.24) the acceleration $a : [0, T] \times \mathbb{R}^3 \to \mathbb{R}^3$ of a material point at position X at time t is given by

$$\rho(X)a(t, X) := \int_{B_\delta(X)} f\left(t, x(t, X') - x(t, X), X' - X\right) dX' + b(t, X)\,, \tag{2.25}$$

where $f : [0, T] \times \mathbb{R}^3 \times \mathbb{R}^3 \to \mathbb{R}^3$ denotes a pair-wise force function, $\rho(X)$ is the mass density and $b : [0, T] \times \mathbb{R}^3 \to \mathbb{R}^3$ the external force. Note that in CCM, besides the force $\mathrm{F} = \operatorname{div} \sigma(u)$ an additional constitutive law is considered. In PD, the material law is part of the pair-wise force function f.

For simple bond-based PD the pair-wise force function evaluated for two material points X and X' (i.e. a single bond) is independent of all other material points

inside the interaction zone. This restricts the Poisson ratio ν of the isotropic linear elastic solid to $1/4$ [Kun11; Kun12]. According to [Sil16a] this restriction holds for a molecular dynamics (MD) system in which the atoms interact only through pair potentials. A more general response must be modeled using multibody potentials in MD and via so-called states in PD.

The state-based peridynamics [Sil+07] overcomes this restriction by introducing peridynamics states $\underline{T}$. A PD state is defined for each all material point X' in the interaction zone and all materials with an arbitrary Poisson ratio $\nu \in (0, 1]$ can be modeled with the state-based PD. Fore more details see [SL08]. The state-based PD equation of motion (2.25) reads as

$$\rho(X)a(t,X) := \int\limits_{B_\delta(X)} \{\underline{T}[t,X]\langle X'-X\rangle - \underline{T}[t,X']\langle X-X'\rangle\}\, dX' + b(t,X)\,. \quad (2.26)$$

In this thesis, however, we focus on the simple bond-based PD, because it is possible to link the bond-based PD with the classical linear elasticity theory, to obtain the model parameters from well-established material parameters, see Section 2.3. Thus, the material behavior of simple bond-based materials is comparable with experimental data and solutions from Linear Elastic Fracture Mechanics (LEFM), see Chapter 5. According to [Sil16b] three important fundamental assumptions of classical continuum mechanics are:

- The medium is continuous (a continuous mass density field exists).
- Internal forces are contact forces (material points interact only if they are separated by zero distance).
- The conservation laws of mechanics apply (conservation of mass, linear momentum, and angular momentum).

The first bullet point is also valid for PD. The second bullet point, that the internal forces are contact forces does not apply, because the exchange of forces via the pair-wise force function inside the interaction zone is normally not restricted to the nearest neighbors. To address the third bullet point, the following assumptions are made on the pair-wise force function that the conservation laws of mechanics apply.

To attain conservation of linear momentum, the pair-wise force function f must satisfy for all times t and arbitrary X' and X

$$f(t, -(x(t,X') - x(t,X)), -(X' - X)) = -f(t, x(t,X') - x(t,X), X' - X) \tag{2.27}$$

and for the conservation of angular momentum, it has to hold that

$$(x(t,X') - x(t,X) + X' - X) \times f\,(t, x(t,X') - x(t,X), X' - X) = 0\,. \tag{2.28}$$

2.3. Bond-based peridynamic material models

The simple bond-based PD is a general principle for the interaction of material points in a continuum. The constitutive material law is described within the pair-wise force function. Next, two specific bond-based models for isotropic materials are introduced.

2.3.1. Prototype Brittle Microelastic Material Model

The PMB model was introduced in [Par+08] as a non-linear micro elastic material model with a notion of failure. In this model the assumption is made, that the pair-wise force function f, which models the internal forces, depends only on the relative normalized bond stretch $s : [0,T] \times \mathbb{R}^3 \times \mathbb{R}^3 \to \mathbb{R}$

$$s(t, x(t,X') - x(t,X), X' - X) := \frac{||x(t,X') - x(t,X))|| - ||X' - X||}{||X' - X||}\,. \tag{2.29}$$

For a bond under tension the function s obviously attains positive values[1]. The stretch in PD is formulated with directly with the positions and not with the gradient (2.3) as in classical continuum mechanics. The pair-wise force function in the PMB model is defined as

$$f(t, x(t,X') - x(t,X), X' - X) :=$$

[1]Note, that in PMB an isotropic material is assumed due to the fact that s depends on $\|X' - X\|$.

$$c\, s(t, x(t, X') - x(t, X), X' - X) \frac{x(t, X') - x(t, X)}{\|x(t, X') - x(t, X)\|} \tag{2.30}$$

with a material dependent stiffness constant c. Figure 2.3 sketches the pair-wise force function f with the stiffness constant c as slope. Now the material model is linear and depends solely on the stiffness constant. The non-linearity for modeling damage via bond breaking is introduced later.

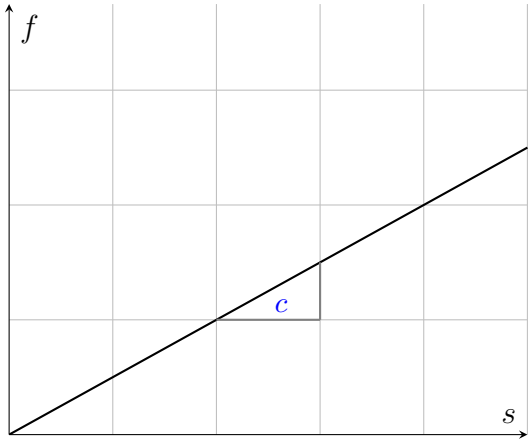

Figure 2.3.: Sketch of the pair-wise linear valued force function f with the stiffness constant c as slope.

To relate PD to the classical theory the interest is in equivalence of PD-energy to classical theory energy, e.g. the total energy density. This will also allow relating the material parameters of the PMB material models to classical ones. Next, a relation to the bulk modulus K, a well-established material parameter from classical theory, and the horizon δ for the stiffness constant via energy equivalence is done. The bulk modulus K, expresses the ratio of the increase of pressure with respect to the relative decrease of the volume.

For the relation to the classical theory the assumption is made, that the pair-wise force function for a micro elastic material is satisfies

$$\begin{aligned} &f(t, x(t, X') - x(t, X), X' - X) = \\ &\frac{\partial}{\partial \left(x(t, X') - x(t, X)\right)} \omega(t, x(t, X') - x(t, X), X' - X) \quad \forall X' - X, x(t, X') - x(t, X)\,, \end{aligned} \tag{2.31}$$

with a scalar micro potential $\omega : [0,T] \times \mathbb{R}^3 \times \mathbb{R}^3 \to \mathbb{R}$. For a large homogeneous body under isotropic tension a valid micro potential can be assumed as

$$\omega(t, x(t,X') - x(t,X), X' - X) := (1/2)cs^2(t, x(t,X') - x(t,X), X' - X)\,. \quad (2.32)$$

This micro potential can be seen as the energy stored in the bond between material point X and X' under the stretch s. Due to symmetry between the both material points, the micro potential is scaled with the factor $1/2$. This energy is the PD analogue of the strain energy in classical theory. Now, the total strain energy density $W_{\text{PD}} : [0,T] \times \mathbb{R}^3 \to \mathbb{R}$ of all bonds in the interaction zone is obtained by

$$W_{\text{PD}}(t,X) := \frac{1}{2}\int_{B_\delta(X)} \omega(t, x(t,X') - x(t,X), X' - X)dX'\,. \quad (2.33)$$

Next, the micro potential for a large homogeneous body under tension (2.32) is applied to the total energy density W_{PD} and the integral is calculated analytically. This results in the total energy density W_{PD}

$$\begin{aligned} W_{\text{PD}}(t,X) &= \int_0^\delta \frac{1}{4}cs(t, x(t,X') - x(t,X), X' - X)^2 dr \quad \text{with } r = X' - X \\ &= \frac{1}{4}\pi c\mathbf{s}^2\delta^4 \quad \text{with } \int_0^\delta s(t, x(t,X') - x(t,X), X' - X)^2 dr \equiv \mathbf{s}^2\,. \end{aligned} \quad (2.34)$$

In classical theory the strain energy density function, which relates the strain energy density to deformation $\mathbf{s}$, is $W(\mathbf{s}) = 9/2 K\mathbf{s}^2$. For obtaining the stiffness constant from the bulk modulus, the assumption is made, that W_{PD} is equivalent for the overall stretch $\mathbf{s}$ to the classical strain energy density W. This energy equivalence delivers

$$\begin{aligned} W_{\text{PD}} &\stackrel{!}{=} W \\ \frac{1}{4}\pi c s^2\delta^4 &= \frac{9}{2}Ks^2 \\ c &= \frac{18K}{\pi\delta^4}\,. \end{aligned} \quad (2.35)$$

Now, the stiffness constant $c_{K,\delta} = 18K/\pi\delta^4$ depends on the bulk modulus K and the length δ of the interaction zone $B_\delta(X)$.

Obviously, the PMB model is linear with respect to the stiffness constant. For modeling damage the concept of a critical bond stretch (for failure) s_c is introduced.

Figure 2.4 sketches the pair-wise force function, where the force jumps to zero as the stretch s exceeds the critical stretch s_c.

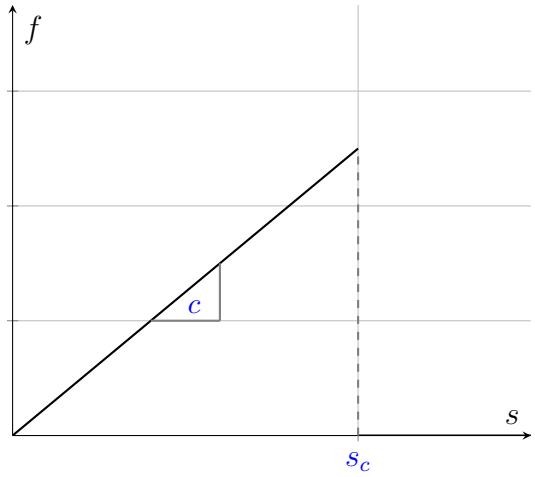

Figure 2.4.: Sketch of the pair-wise linear valued force function f with the stiffness constant c as slope and the critical bond stretch s_c.

Furthermore, the linear pair-wise force function (2.30) is extended with a scalar valued history dependent function $\mu : [0,T] \times \mathbb{R}^3 \times \mathbb{R}^3 \to \mathbb{N}$

$$f(t, x(t,X') - x(t,X), X' - X) := \\ cs(t, x(t,X') - x(t,X), X' - X)\mu(t, x(t,X') - x(t,X), X' - X)\frac{x(t,X') - x(t,X)}{\|x(t,X') - x(t,X)\|}. \tag{2.36}$$

To this end, the function

$$\mu(t, x(t,X') - x(t,X), X' - X) := \begin{cases} 1 & s(t, x(t,X') - x(t,X), X' - X) < s_c \\ 0 & \text{otherwise} \end{cases} \tag{2.37}$$

indicates if the bond between X and X' is broken, which means the bond between them is stretched over the critical value for bond failure. With the scalar valued

history dependent function μ (2.37) the notion of damage $d(t, X) : [0, T] \times \mathbb{R}^3 \to \mathbb{R}$ can be introduced via

$$d(t, X) := 1 - \frac{\int\limits_{B_\delta(X)} \mu(t, x(t, X') - x(t, X), X' - X) dX'}{\int\limits_{B_\delta(X)} dX'} . \tag{2.38}$$

To obtain the critical bond stretch for failure s_c, a large homogeneous body is considered. The energy for breaking the body (i.e. $B_\delta(X)$) horizontally into two halves U_δ and L_δ is considered. Thus, the bonds of all material points along the dashed line $0 \leq z \leq \delta$ in L_δ to any material point in U_δ inside the interaction zone must be stretched beyond the critical bond stretch for failure s_c (see Figure 2.5).

To compute the total energy $G_{\text{PD}} : [0, T] \times \mathbb{R}^3 \to \mathbb{R}$ to break all bonds between

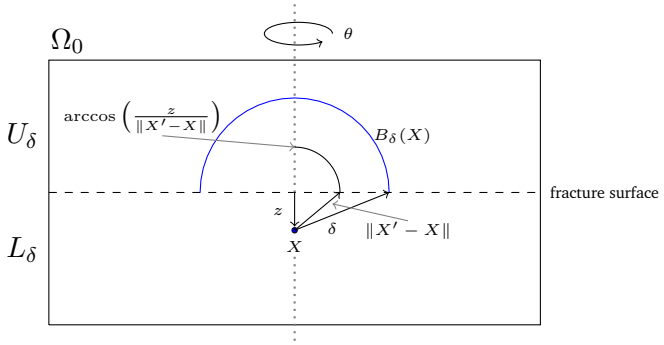

Figure 2.5.: A cross section of the continuum in the reference configuration Ω_0 is horizontally divided in U_δ and L_δ. To obtain the critical stretch for bond failure s_c, the energy to break all bonds between the material points along the dashed line $0 \leq z \leq \delta$ and blue semi-circle of the interaction zone $B_\delta(X)$ is considered.

all material points along the dashed line $0 \leq z \leq \delta$ in L_δ and the blue semi-circle, first all material points along the vertically direction need to be considered and this yields to the first integral in Equation (2.39).

$$\begin{aligned} G_{\text{PD}}(t, X) := \frac{1}{2} \int_0^\delta \int_0^{2\pi} \int_z^\delta \int_0^{\arccos(z/\|X' - X\|)} & cs(t, x(t, X') - x(t, X), X' - X)^2 (X' - X)^2 \\ & \sin\phi \, d\phi \, d(X' - X) \, d\theta \, dz \\ = & \frac{\pi c \mathbf{s}^2 \delta^5}{10} . \end{aligned} \tag{2.39}$$

The second integral is is the rotation with the angle θ, the third one along the dashed line, and the last one along the circular segment. Again, here $\mathbf{s}$ is the overall stretch in the integration.

The energy to break all bonds between the two halves can be related to the strain energy release rate G from classical theory. The strain energy release rate G in classical theory expresses the energy, which is dissipated during the fracture per unit, to create the newly generated fracture surface area. To obtain the critical bond stretch s_c the energy equivalence for the PD strain energy release rate G_{PD} and the classical strain energy release rate $G = {}^{K_{\text{Ic}}^2(1-\nu^2)}/_{\mathtt{E}}$ 2D plane strain, with $\nu = 1/4$ and the Young modulus $\mathtt{E} = 3K(1-2\nu)$ [Hah76], is assumed. Thus, this ends up with

$$\begin{aligned} G &\stackrel{!}{=} G_{\text{PD}} \\ \frac{K_{\text{Ic}}^2(1-\nu^2)}{\mathtt{E}} &= \frac{\pi c \mathbf{s}^2 \delta^5}{10} \\ \frac{K_{\text{Ic}}^2(1-\nu^2)}{3K(1-2\nu)} &= \frac{\pi c \mathbf{s}^2 \delta^5}{10} \\ \mathbf{s} &= \frac{5}{12}\sqrt{\frac{K_{\text{Ic}}}{K^2\delta}}\,. \end{aligned} \tag{2.40}$$

From Equation (2.40) it can be assumed that the critical stretch s_c is equal to $\mathbf{s}$. Table 2.1 shows the stiffness constant and the critical stretch related to the bulk modulus and the critical stress intensity factor. Note, that here the stiffness constant c and the critical stretch for bond failure s_{c} are independent of the position X in the reference configuration Ω_0, because the interaction zone of each material point is identical. Thus, these parameters are "homogeneous" for all material points.

Stiffness constant	Critical stretch for bond failure
$c_{K,\delta} = \dfrac{18K}{\pi\delta^4}$	$s_{c_{K,K_{\text{Ic}}^2,\delta}} = \dfrac{5}{12}\sqrt{\dfrac{K_{\text{Ic}}}{K^2\delta}}$

Table 2.1.: Material parameters for the PMB model related to the bulk modulus K and the critical stress intensity factor K_{Ic}.

2.3.2. Softening Model

The stiffness constant and the critical stretch for bond failure in the PMB bond-based material model (Table 2.1), depend on the horizon δ of the interaction zone $B_\delta(X)$. The commonly named softening model (SM) [Lip14; Lip15] is a different approach, where no bond breaking is modeled but the force softens to zero after passing a inflection point. The energy of bond-based softening model (SM) converges to the classical theory via Γ-convergence for the horizon going to zero [Lip14]. Thus, the length scale δ of the non-local interaction zone describes a length scale associated with the process zone of the material. In the limit of a decreasing horizon δ the associated process zone shrinks to a crack tip with a singularity.

The model is briefly introduced here. In Section 3.1.1 the discretized softening model is validated numerically and in Section 5.3 the obtained Young modulus and Poisson ratio in the simulations is compared with the ones from classical theory.

This mesoscopic model is characterized through a non-local peridynamic potential $\underline{W} : [0,T] \times \mathbb{R}^d \times \mathbb{R}^d \to \mathbb{R}$. The generic form of these potentials is given by

$$\underline{W}(t, x(t,X') - x(t,X), X' - X) := \frac{1}{\delta^3} J\left(\frac{\|X' - X\|}{\delta}\right) \cdot \underline{F}(t, x(t,X') - x(t,X), X' - X)\,, \quad (2.41)$$

with $\underline{F} : [0,T] \times \mathbb{R}^d \times \mathbb{R}^d \to \mathbb{R}$ as a smooth, positive and concave potential function with the limit $\underline{F}_\infty$. Note, that the potential $\underline{F}$ depends on the shear strain $\underline{s}$ (2.42) with the power of two. Figure 2.6a shows the energy per unit bond length per unit area due to a shear strain of magnitude $|\underline{s}|$. The shear strain $\underline{s} : [0,T] \times \mathbb{R}^d \times \mathbb{R}^d \to \mathbb{R}$ is defined by

$$\underline{s}(t, x(t,X') - x(t,X), X' - X) := \frac{(x(t,X') - X') - (x(t,X) - X)}{\|X' - X\|} \bullet \frac{X' - X}{\|X' - X\|}\,. \quad (2.42)$$

Note, that in this model a small deformation with respect to the reference configuration Ω_0 is focused on. The assumption is made that for a small deformation $|\underline{s}| \ll {}^{r}/\sqrt{\|X' - X|}$ holds and the force $\underline{f}$ stays in the linear regime. Figure 2.6b shows the elastic and then softening constitutive law for the bond force $\underline{f}$. Instead of a critical stretch for bond failure s_c (2.37). The softening model has an inflection point ${}^{r}/\sqrt{\|X' - X\|}$ and the shear strain $\underline{s}$ exceeds after this point the force starts to

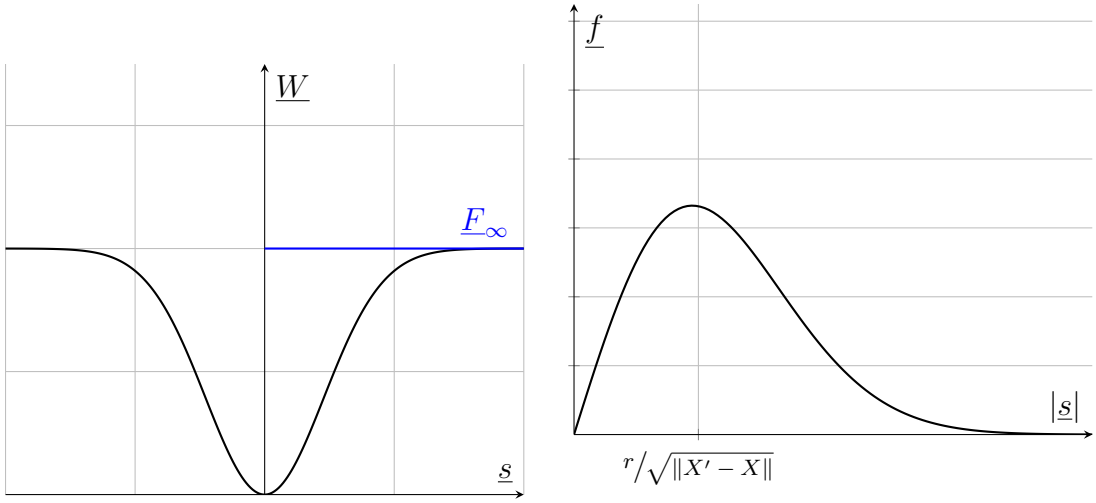

(a) A generic non-local PD potential $\underline{W} : [0,T] \times \mathbb{R}^d \times \mathbb{R}^d \to \mathbb{R}$ with the associated positive, smooth and concave potential function $\underline{F} : [0,T] \times \mathbb{R}^d \times \mathbb{R}^d \to \mathbb{R}$ with the properties $\lim_{r \to 0^+} \underline{F}(r)/r = \underline{F}'(0) > 0$ and $\lim_{r \to \infty} \underline{F}(r) = \underline{F}_\infty < \infty$.

(b) The elastic and then softening constitutive law for the bond force $\underline{f}$, derived by the potential $\underline{W}$, with the inflection point $|\underline{s}| > r/\sqrt{\|X'-X\|}$, where the bond starts to soften.

Figure 2.6.: A generic non-local PD potential $\underline{W}$, a smooth and concave function (a) and the derived elastic and then softening constitutive law for the bond force (b).

"soften" to zero. The force is given by the derivation of the generic potential $\underline{W}$ with respect to the shear strain $\underline{s}$

$$\underline{f}(t, x(t,X') - x(t,X), X' - X) := \frac{\partial}{\partial \underline{s}} \underline{W}(t, x(t,X') - x(t,X), X' - X) = \frac{2}{\delta} J\left(\frac{\|X' - X\|}{\delta}\right) \underline{F}'(t, x(t,X') - x(t,X), X' - X) \underline{s}(t, x(t,X') - x(t,X), X' - X)\,. \tag{2.43}$$

Next, the peridynamics fracture toughness $\underline{G}_{\text{PD}} : [0,T] \times \mathbb{R}^d \to \mathbb{R}$, which is the property of a material containing a crack for resisting fracture, is obtained. The

energy to soften all bonds $\underline{s} \to \infty$ of the initial length $\|X' - X\|$ per unit area inside the interaction zone in the area U_δ (Figure 2.5) is given by

$$\begin{aligned}
\underline{G}_{\text{PD}}(t, X) &:= \frac{2}{\mathbf{V}_d} \int\limits_{B_\delta(X) \cap U_\delta} \frac{1}{\delta} J\left(\frac{\|X' - X\|}{\delta}\right) \|X' - X\| \underbrace{\underline{F}(t, x(t, X') - x(t, X), X' - X)}_{\lim\limits_{\underline{s} \to \infty} \underline{F} = \underline{F}_\infty} dX' \\
&\overset{d=2}{=} 2 \left(\frac{2}{\pi \delta^2} \int\limits_0^\delta \int\limits_z^\delta \int\limits_0^{\arccos(z/\|X' - X\|)} \frac{1}{\delta} J\left(\frac{\|X' - X\|}{\delta}\right) \|X' - X\| \underline{F}_\infty d\phi d\|X' - X\| dz \right) \\
&= \frac{4}{\pi \delta^3} \underline{F}_\infty \left(\int\limits_0^\delta \int\limits_z^\delta J\left(\frac{\|X' - X\|}{\delta}\right) \|X' - X\| d\|X' - X\| dz \right) \\
&= \frac{4}{\pi \delta^3} \underline{F}_\infty \left(\int\limits_0^\delta J\left(\frac{\|X' - X\|}{\delta}\right) \|X' - X\|^2 d \underbrace{\|X' - X\|}_{\leq \delta r} \right) \\
&= \frac{4}{\pi} \underline{F}_\infty \int\limits_0^1 J(r)\, r^2 dr\,.
\end{aligned} \tag{2.44}$$

For the three dimensional case the calculation for $\underline{G}_{\text{PD}_3} : [0, T] \times \mathbb{R}^d \to \mathbb{R}$ is the same calculation with $\mathbf{V}^3 = {}^{4\pi\delta^3}/_3$ and yields

$$\underline{G}_{\text{PD}_3}(t, X) := \frac{6}{4} \underline{F}_\infty \int\limits_0^1 J(r) r^3 dr. \tag{2.45}$$

In both dimensions the fracture toughness depends on the limit of $\underline{F}_\infty$ and the influence function $J(r)$ and there is no relation to the process zone δ of the material.

For calibrating the shear modulus μ, the ratio of shear strain to shear stress, to the non-local PD potential two steps need to be done. First, the assumption is made that for a small homogeneous deformation, where $x(t, X)$ is sufficiently small across the interaction zone, a symmetric strain matrix $D_t \in \mathbb{R}^d \times \mathbb{R}^d$, such that $x(t, X) \approx D_t X$ exists. Thus, the shear strain $\underline{s}$ (2.42) is rewritten with respect to the symmetric strain matrix D_t as

$$\underline{s}(t, x(t, X') - x(t, X), X' - X) = \frac{x(t, X') - x(t, X)}{\|X' - X\|} \bullet \frac{X' - X}{\|X' - X\|}$$

$$= \underbrace{\frac{D_t(X'-X)}{\|X'-X\|}}_{D_t\left(\frac{X'-X}{\|X'-X\|}\right)} \bullet \frac{X'-X}{\|X'-X\|}$$
$$= D_t \frac{X'-X}{\|X'-X\|} \bullet \frac{X'-X}{\|X'-X\|}. \tag{2.46}$$

Second, the pair-wise force $\underline{f}$ (2.43) is approximated by a Taylor Series of the potential function $\underline{F}$ (2.41) centered at $\underline{s}$ equals zero. The Taylor Series until the second term delivers the pair-wise force function $\underline{f}_T : [0,T] \times \mathbb{R}^d \times \mathbb{R}^d \to \mathbb{R}$

$$\underline{f}_T(t, x(t,X') - x(t,X), X'-X) \approx \overbrace{\underline{F}''(0,0,X'-X)}^{=\underline{F}_0''} \|X'-X\| \cdot \underline{s}^2(t, x(t,X') - x(t,X), X'-X). \tag{2.47}$$

The density $\underline{W}_T : [0,T] \times \mathbb{R}^d \to \mathbb{R}$ of the non-local PD potential $\underline{W}$ (2.41) is rewritten with the Taylor Series for $\underline{f}_T$ (2.47) and the strain matrix D_t (2.46) as

$$\underline{W}_T(t,X) \approx \frac{1}{\delta} \frac{\underline{F}_0''}{\mathbf{V}_d} \int_{B_\delta(X)} J\left(\frac{\|X'-X\|}{\epsilon}\right) \|X'-X\| \left(D_t \frac{X'-X}{\|X'-X\|} \bullet \frac{X'-X}{\|X'-X\|}\right)^2 dX'. \tag{2.48}$$

Now, the density $\underline{W}_T$ with the interaction zone $B_\delta(X)$ is normalized to the interaction zone $B_1(\mathbf{0})$. Where $B_1(\mathbf{0})$ is in three dimensions a ball with radius 1 centered at $\mathbf{0} = (0,0,0)^T \in \mathbb{R}^3$ and in two dimensions a circle with radius 1 centered at $\mathbf{0} = (0,0)^T \in \mathbb{R}^2$. With the normalization to $B_1(\mathbf{0})$ following expressions change to $X'-X = \delta\xi$, $\|X'-X\| = \delta\|\xi\|$ and $dX' = \delta^d$. This yields for the normalized density $\underline{W}_T^1 : [0,T] \to \mathbb{R}$ with the interaction zone $B_1(\mathbf{0})$

$$\underline{W}_T(t,X) \approx \frac{\underline{F}_0''}{\delta \mathbf{V}_d} \int_{B_\delta(X)} J\left(\frac{\|X'-X\|}{\delta}\right) \overbrace{\|X'-X\|}^{\delta\|\xi\|} \left(D_t \frac{\overbrace{X'-X}^{\delta\xi}}{\|X'-X\|} \bullet \frac{X'-X}{\|X'-X\|}\right)^2 \overbrace{dX'}^{\delta^d}$$

$$\begin{aligned}\underline{W}_T^1(t,\xi) &\approx \frac{\underline{F}_0''}{w_d \delta^{d+1}} \int\limits_{B_1(\mathbf{0})} J\left(\frac{\delta\|\xi\|}{\delta}\right) \delta\|\xi\| \left(D_t \frac{\delta\xi}{\delta\|\xi\|} \bullet \frac{\delta\xi}{\delta\|\xi\|}\right)^2 d\delta^d\xi \\ &\approx \frac{\underline{F}_0''}{w_d} \int\limits_{B_1(\mathbf{0})} J\left(\|\xi\|\right) \|\xi\| \left(D_t \frac{\xi}{\|\xi\|} \bullet \frac{\xi}{\|\xi\|}\right)^2 d\xi\,, \end{aligned} \tag{2.49}$$

with $w_2 = \pi$ and $w_3 = {}^4\!/_3\pi$. Next, the normalized density $\underline{W}_T^1$ with respect to a Cartesian coordinate system $\mathbb{R}^d$ is transformed to a Polar coordinate system $P(r,\theta)$. The transformation of the coordinate system following expresses change $d\xi = r dr d\Theta$ and $e = {}^{X'-X}\!/_{\|X'-X\|}$. The normalized density $\underline{W}_T^1$ in Polar coordinates yields

$$\begin{aligned}\underline{W}_T^1(t,e) &\approx \frac{\underline{F}_0''}{w_d} \int\limits_{B_1(\mathbf{0})} \int\limits_0^{2\pi} J\left(r\right) r^d (D_t e \bullet e)^2 d\Theta dr \\ &\approx \frac{\underline{F}_0''}{w_d} \int\limits_{B_1(\mathbf{0})} J\left(r\right) r^d dr \underbrace{\int\limits_0^{2\pi} (D_t e \bullet e)^2 d\Theta}_{} \\ &\qquad \approx \int\limits_0^{2\pi} \left(\sum_{i,j=1}^d D_{t_{ij}} e_i e_j\right) \left(\sum_{k,l=1}^d D_{t_{kl}} e_k e_l\right) d\Theta \\ &\qquad \approx \sum_{i,j=1}^d \sum_{k,l=1}^d \int\limits_0^{2\pi} D_{t_{ij}} D_{t_{kl}} e_i e_j e_k e_l d\Theta \\ &\qquad \approx \sum_{i,j=1}^d \sum_{k,l=1}^d \left(\int\limits_0^{2\pi} e_i e_j e_k e_l d\Theta\right) D_{t_{ij}} D_{t_{kl}} \\ &\approx \sum_{i,j=1}^d \sum_{k,l=1}^d \left(\frac{\underline{F}_0''}{w_d} \int\limits_0^1 J\left(r\right) r^d dr\right) \int\limits_0^{2\pi} e_i e_j e_k e_l d\Theta D_{t_{ij}} D_{t_{kl}} \\ &\approx \mathbb{C}_{\text{PD}} D_t : D_t \\ &\approx \sum_{i,j,k,l=1}^d \mathbb{C}_{\text{PD}_{ijkl}} D_{t_{ij}} D_{t_{kl}}\,. \end{aligned} \tag{2.50}$$

Now, transforming into polar coordinates and using the strain matrix D_t (2.46), instead of the point-wise displacement delivers, the peridynamic strain energy density tensor for an isotropic elastic material for $d = 2$ and $d = 3$. Table 2.2 shows how to write the material constants from classical theory depending on the

dimension d, with respect to the shear modulus μ and the bulk modulus K [Mil02]. For classical theory the stress tensor for isotropic materials is given by

Shear modulus	μ	–
Bulk modulus	K	–
Lame modulus	λ	$K - 2\mu/d$
Young modulus	E	$2d^2K/(2\mu + d(d-1)K)$
Poisson ratio	ν	$(dK - 2\mu)/(2\mu + d(d-1)K)$

Table 2.2.: Material parameters from classical theory depending on the dimension d with respect to the shear modulus μ and the bulk modulus K.

$$T := 2\mu\varepsilon + (\underbrace{K - 2\mu/d}_{=\lambda})tr(\varepsilon)\mathbb{I} = 2\mu\varepsilon + \lambda tr(\varepsilon)\mathbb{I} \tag{2.51}$$

with the strain tensor E. Now the energy of an isotropic elastic materials is defined by

$$T_{ij}\varepsilon_{ij} = \underbrace{\mathbb{C}_{ijkl}}_{=\mu(\delta_{ik}\delta_{jl}+\delta_{il}\delta_{jk})+\lambda\delta_{ij}\delta_{kl}} \varepsilon_{ij}\varepsilon_{kl} = 2\mu|\varepsilon|^2 + \lambda(tr(\varepsilon)\mathbb{I})^2\,. \tag{2.52}$$

With Lemma 4.3 in [JLL90] the isotropic elastic tensor $\mathbb{C}_{ijkl}$ (2.20) can be divided into the so-called "bulk trace" $\mathbb{C}_{iijj}$ (2.53) and the so-called "shear trace" $\mathbb{C}_{ijij}$ (2.54).

$$\begin{aligned}\mathbb{C}_{iijj} &= \sum_{i=1}^{d}\sum_{j=1}^{d}\mu\left(\delta_{ij}\delta_{ij} + \delta_{ij}\delta_{ij}\right) + \lambda\delta_{ii}\delta_{jj} \\ &= \mu(d+d) + \lambda d^2 \\ &= d(2\mu + \lambda d) \qquad (2.53)\end{aligned} \qquad \begin{aligned}\mathbb{C}_{ijij} &= \sum_{i=1}^{d}\sum_{j=1}^{d}\mu\left(\delta_{ii}\delta_{jj} + \delta_{ij}\delta_{ji}\right) + \lambda\delta_{ij}\delta_{ij} \\ &= \mu(d^2+d) + \lambda d \\ &= d(2\mu + \lambda d) \qquad (2.54)\end{aligned}$$

Table 2.3 shows the bulk trace and the shear trace for two dimensions and three dimensions. Now, the assumption is made, that the bulk modulus from classical theory is the same as the PD bulk trace. Thus, the shear modulus of the bond-based softening material model is calculated for two dimensions and three dimensions by

Dimension	Bulk trace	Shear trace
2	$\mathbb{C}_{iijj} = 2(2\mu + 2\lambda)$	$\mathbb{C}_{ijij} = 2(3\mu + \lambda)$
3	$\mathbb{C}_{iijj} = 3(2\mu + 3\lambda)$	$\mathbb{C}_{ijij} = 3(4\mu + \lambda)$

Table 2.3.: The so-called "bluk trace" $\mathbb{C}_{iijj}$ and the so-called "shear trace" $\mathbb{C}_{ijij}$ of the isotropic elastic tensor $\mathbb{C}$ depending on the dimension d respective to [JLL90].

$$\mathbb{C}_{PD_{ijij}} = \mathbb{C}_{ijij} \qquad \mathbb{C}_{PD_{ijij}} = \mathbb{C}_{ijij}$$

$$2\underline{F}_0'' \int_0^1 J(r) r^2 dr \widehat{=} \begin{bmatrix} 2(2\mu + 2\lambda) \\ 2(3\mu + \lambda) \end{bmatrix}, \qquad 3\underline{F}_0'' \int_0^1 J(r) r^3 dr \widehat{=} \begin{bmatrix} 3(2\mu + 3\lambda) \\ 3(4\mu + \lambda) \end{bmatrix}$$

$$\Rightarrow \lambda = \mu = \underline{F}_0''/4 \int_0^1 J(r) r^2 dr \qquad \Rightarrow \lambda = \mu = \underline{F}_0''/5 \int_0^1 J(r) r^3 dr\,.$$

Table 2.4 centralizes the shear modulus and the fracture toughness of the bond-based softening model in two and three dimensions. Note, that the material

Dimension	Shear modulus	Fracture toughness
2	$\mu = \underline{F}_0''/4 \int_0^1 J(r) r^2 dr$	$G = 4/\pi \underline{F}_\infty \int_0^1 J(r) r^2 dr$
3	$\mu = \underline{F}_0''/5 \int_0^1 J(r) r^3 dr$	$G = 6/4 \underline{F}_\infty \int_0^1 J(r) r^3 dr$

Table 2.4.: Horizon independent material parameters for the softening model.

parameters of the softening model are obtained in a way, such that the parameters are independent on the horizon δ of the interaction zone. Accordingly, the length scale of the non local interaction is not a discretization parameter and instead describes a length scale associated with the process zone of the material.

Energy equivalence with the classical theory

In Section 2.3.2 the bond-based model with a generic non-local peridynamic potential (2.41) is introduced. For the energy equivalence for the fracture toughness

and the shear modulus (Table 2.4) a specific positive, smooth and concave function $\underline{F} : [0,T] \times \mathbb{R}^3 \times \mathbb{R}^3 \to \mathbb{R}$ is defined by

$$\underline{F}(t, x(t,X') - x(t,X), X' - X) := \beta \left(1 - e^{(-\alpha \|X'-X\| \underline{s}^2(t, x(t,X') - x(t,X), X'-X)}\right) . \tag{2.55}$$

In the softening model two material parameters α and β for modeling the material behavior exist. Figure 2.7a shows different plots of $\underline{F}$ for a constant β and different values of α. Where α influences the slope of the potential before it reaches the constant part, which is influenced by β. Figure 2.7b shows the elastic and then

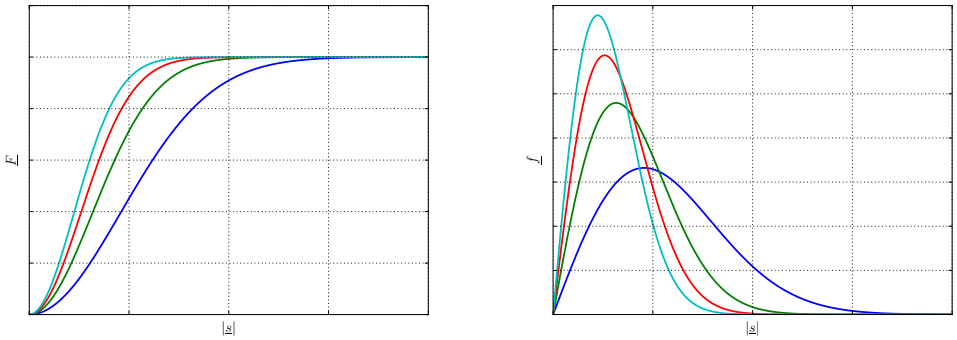

(a) $\underline{F}(t, x(t,X') - x(t,X), X' - X)$ **(b)** $\underline{f}(t, x(t,X') - x(t,X), X' - X)$

Figure 2.7.: Different plots of the specific positive, smooth and concave function $\underline{F}$ (2.55) and the derived force $\underline{f}$ (2.56) for a constant β and different values of α.

softening constitutive law for the bond force $\underline{f}$ (2.43) for a constant β and different values of α, which is derived by

$$\begin{aligned} \underline{f}(t, x(t,X') - x(t,X), X' - X) :&= \frac{1}{\delta} \frac{1}{\|X' - X\|} \frac{\partial}{\partial_{\underline{s}}} \underline{F}(t, x(t,X') - x(t,X), X' - X) \\ &= \frac{2}{\delta} \alpha\beta e^{(-\alpha \|X'-X\| \underline{s}^2(t, x(t,X') - x(t,X), X'-X))} \\ &\quad \cdot s(t, x(t,X') - x(t,X), X' - X) . \end{aligned} \tag{2.56}$$

Table 2.5 shows the material parameters in three dimensions with respect to specific the values for $\underline{F}_\infty = \beta$ and $F_0'' = \alpha\beta$ for the non local potential peridynamic potential (2.55). To relate the softening material parameters

Shear modulus	Fracture toughness
$\mu = {}^{\alpha\beta}/_{5} \int_0^1 J(r) r^3 dr$	$G = {}^{6\beta}/_{4} \int_0^1 J(r) r^3 dr$

Table 2.5.: Horizon independent shear modulus μ and fracture toughness G for the specific non local peridynamic potential (2.55).

α and β to the bulk modulus and the fracture toughness from classical theory, the same energy equivalence as for the PMB model is applied for the fracture toughness and the shear modulus with the influence function $J(r) = 1$

$$
\begin{aligned}
G &\stackrel{!}{=} G_{\text{PD}} \\
\frac{2}{3}\frac{K_{\text{Ic}}^2}{K} &= \frac{6\beta}{4} \underbrace{\int_0^1 J(r) r^3 dr}_{=[1/4 r^4]_0^1 = 1/4} \\
\frac{2}{3}\frac{K_{\text{Ic}}^2}{K} &= \frac{6}{16}\beta \\
\Rightarrow \beta &= \frac{16}{9}\frac{K_{\text{Ic}}^2}{K}
\end{aligned}
\qquad (2.57)
$$

$$
\begin{aligned}
\lambda &\stackrel{!}{=} \mu_{\text{PD}} = \lambda_{\text{PD}} \\
\frac{3}{5}K &= \frac{\alpha\beta}{5} \underbrace{\int_0^1 J(r) r^3 dr}_{=[1/4 r^4]_0^1 = 1/4} \\
\frac{3}{5}K &= \frac{1}{20}\frac{16}{9}\frac{K_{\text{Ic}}^2}{K}\alpha \\
\Rightarrow \alpha &= \frac{27}{4}\frac{K^2}{K_{\text{Ic}}^2}\,.
\end{aligned}
\qquad (2.58)
$$

This ends up with the material parameters α and β for the softening model with the specific potential (2.55) (see Table 2.6). Here, these material parameters not only depend on the bulk modulus and the critical stress intensity factor, but also are independent on the horizon of the process zone of the material. In comparison to the PMB or DPMB model (see Table 3.1) the softening model has the same material parameters for all horizons.

$\alpha_{K,K_{\text{Ic}}} = \frac{27}{4}\frac{K^2}{K_{\text{Ic}}^2}$	$\beta_{K,K_{\text{Ic}}} = \frac{16}{9}\frac{K_{\text{Ic}}^2}{K}$

Table 2.6.: Material parameters α and β for the softening model with the specific potential (2.55). Note, that these parameters depend solely on the bulk modulus and the critical stress intensity factor.

3.Discretization

To discretize the bond-based peridynamic equation of motion (2.25) different approaches have been proposed in literature: continuous and discontinuous Galerkin finite element methods [CG11], Gauss quadrature [WE05] and spatial discretization can be applied [EW07a; Par+08]. With respect to the computational costs the EMU nodal discretization (EMU ND), a discretization for the strong form of the PD equation of motion is feasible. For this discretization an efficient load distribution scheme [Kil08; LH12b] exist. Therefore, we developed a bond-based peridynamic code using the EMU ND on Graphics Processing Unit (GPU) implemented with Compute Unified Device Architecture (CUDA) [Die12]. Due to this benefit for an efficient parallel implementation on CPU and GPU all numerical results in Chapter 5 are obtained via a EMU ND.

3.1. EMU nodal discretization

For the EMU ND the assumption is made, that all material points X are placed at the nodes $\mathbf{X} := \{X_i \in \mathbb{R}^3 | i = 1, \dots, n\}$ of a regular grid (Figure 3.1a) in the reference configuration Ω_0. The discrete nodal spacing Δx between X_i and X_j is defined as $\Delta x = \|X_j - X_i\|$. Now, the discrete interaction zone $B_\delta(X_i)$ of X_i is given by $B_\delta(X_i) := \{X_j | \, ||X_j - X_i|| \leq \delta\}$. Note, that the interaction zone solely depends at placement of the nodes in the reference configuration Ω_0. The amount of neighbors inside the interaction zone $B_\delta(X_i)$ is donated as $|B_\delta(X_i)|$.

For all material points at the nodes $\mathbf{X} := \{X_i \in \mathbb{R}^3 | i = 1, \dots, n\}$ a surrounding volume $\mathbf{V} := \{ \mathbf{V}_i \in \mathbb{R} | i = 1, \dots, n\}$ is assumed. These volumes are non overlapping $\mathbf{V}_i \cap \mathbf{V}_j = \emptyset$ and recover the volume of the volume of the reference configuration $\sum_{i=1}^{n} \mathbf{V}_i = \mathbf{V}_{\Omega_0}$. Figure 3.1a shows the dual mesh for the nodes $\mathbf{X}$ with the surrounding volume $\mathbf{V_i}$ for the material point $\bullet$ located at X_i in two dimensions. Figure 3.1b shows the surrounding volume $\mathbf{V}_1$ for the material point $\bullet$ located at X_1 in three dimensions. According to the assembly of the material points on the regular grid the surrounding volume for all X_i is given by $\mathbf{V}_i = \Delta x^3$ in three dimensions and respective $\mathbf{V}_i = \Delta x^2$ in two dimensions.

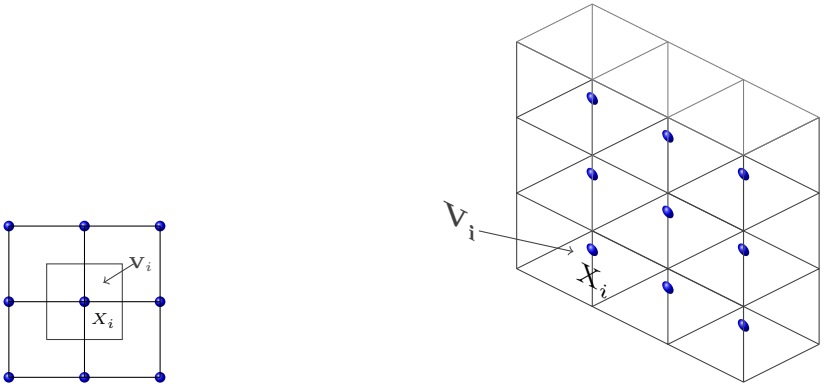

(a) The dual mesh in two dimensions with the surrounding volume $\mathbf{V}_i$ for the material point • located at the node X_i in the reference configuration Ω_0 in two dimensions.

(b) Material point • located at the node X_i in the reference configuration Ω_0 with the surrounding non overlapping volume $\mathbf{V}_i$ in three dimensions.

Figure 3.1.: Material points placed at the nodes of a regular grid (a) and the surrounding volumes $\mathbf{V}$ for the material points at X_{ND} (b).

Applying these assumptions to the peridynamic equation of motion (2.25) yields the discrete peridynamic equation of motion

$$\rho(X_i)a(t,X_i) = \sum_{X_j \in B_\delta(X_i)} f\left(t, x(t,X_j) - x(t,X_i), X_j - X_i\right) d\mathbf{V}_j + b(t,X_i)\,. \tag{3.1}$$

With $\rho(X_i)$ as the material density at X_i, $\mathbf{V}_j$ the surrounding volume of the node at X_j, and $b(t,X_i)$ as an external force. Next, two common issues of the EMU nodal discretization, the integration accuracy and the skin effect, are emphasized.

Figure 3.2a shows a common integration error for a one-point spatial discretization for integration nodes (green colored) close to the boundary of the interaction zone $B_\delta(X_i)$. In Equation 3.1 the volume of each node inside $B_\delta(X_i)$ has the same influence to the pair-wise force function f, independent on the position. Thus, volumes close to the boundary should be scaled, because not the whole volume

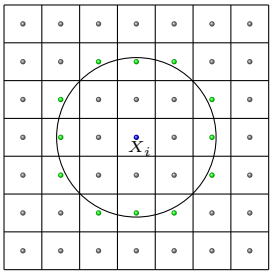

(a) The interaction zone $B_\delta(X_i)$ of integration node at position X_i. The green colored integration nodes are inside $B_\delta(X_i)$ and influence the pair-wise force function f with the full surrounding volume.

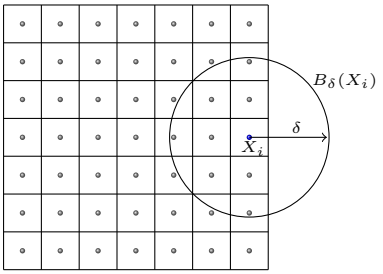

(b) The integration node at position X_i, close to the boundary, has fewer neighbors inside the integration zone $B_\delta(X_i)$ as an integration node in the middle. This results to the commonly named skin effect.

Figure 3.2.: Two common issues for the EMU nodal discretization: (a) integration error with volumes $\mathbf{V}$ close to the border of the integration zone and (b) the commonly named skin effect.

should influence the pair-wise force function f. Parks and et al. suggested as scaling function $\tau : \mathbb{R}^3 \times \mathbb{R}^3 \to \mathbb{R}$

$$\tau(X_j, X_i) = \begin{cases} -\frac{1}{2r_s}\|X_j - X_i\| + \left(\frac{\delta}{2r_s} + \frac{1}{2}\right), & \delta - r_s \leq \|X_j - X_i\| \leq \delta \\ 1, & \|X_j - X_i\| \leq \delta - r_s \\ 0, & \text{otherwise,} \end{cases} \tag{3.2}$$

for the scaling of the surrounding volume $\tilde{\mathbf{V}}_j(X_i) := \tau(X_j, X_i)\mathbf{V}_j$, with $r_s := {}^{\Delta x}/_2$ in [Par+08]. For the two dimensional peridynamics model improved one-point quadrature rules based on analytic solutions are presented in [Sel14; BD12].

Figure 3.2b emphasizes the commonly named skin effect, where material points close to the boundary have fewer neighbors in the interaction zone $B_\delta(X_i)$ then material points inside the body in the reference configuration Ω_0 [Hu+12; BH11].

3.1.1. Numerical verification of a bond-based peridynamic softening model

For the softening model (SM), introduced in Section 2.3.2, the discretization with the EMU ND can be verified via energy equivalence. The classical isotropic energy $W_{\mathrm{M}} : \mathbb{R}^{3\times3} \to \mathbb{R}$ for a small deformation with the deformation matrix $D_t : \mathbb{R}^3 \times \mathbb{R}^3$ is obtained by

$$W_{\mathrm{M}}(D_t) = 2\mu|D_t|^2 + \lambda(\mathrm{tr}D_t)^2\,. \tag{3.3}$$

This energy can be related to the energy per unit length to soften a bond $\underline{s} \to \infty$. Especially, the energy $\underline{W}_{\mathrm{D}} : [0,t] \times \mathbb{R}^3 \to \mathbb{R}$ with respect to the EMU nodal discretization (EMU ND) inside the interaction zone $B_\epsilon(X_i)$ is approximated by

$$\underline{W}_{\mathrm{D}}(t, X_i) := \frac{2}{\epsilon}\alpha\beta \sum_{X_j \in B_\epsilon(X_i)} \hat{s}(t, X_j, X_i)\,, \tag{3.4}$$

for a small uni-directional shear strain $\hat{s} : [0,T] \times \mathbb{R}^3 \times \mathbb{R}^3 \to \mathbb{R}$

$$\hat{s}(t, X_i, X_j) := \frac{(X_{j_1} - X_{i_1})^2}{\|X_j - X_i\|^2} t\,. \tag{3.5}$$

Note, that for small deformation, such that the force $\underline{f}$ (2.56) is in the linear regime in Figure 2.7b, the force can be seen as the slope $\alpha\beta$. For the comparison with the classical theory the uni-directional shear strain $\hat{s}$ (3.5) is related to the deformation matrix $D_t : \mathbb{R}^3 \times \mathbb{R}^3$, such that the shear strain $\hat{s}$ is the first entry of the matrix

$$D_t \begin{pmatrix} \hat{s}(t, X_i, X_j) & 0 & 0 \\ 0 & 0 & 0 \\ 0 & 0 & 0 \end{pmatrix} \tag{3.6}$$

and the classical isotropic energy $W_{\mathrm{M}} : [0,T] \times \mathbb{R}^3 \times \mathbb{R}^3 \to \mathbb{R}$ (3.3) is simplified to

$$W_{\mathrm{M}}(t, X_i, X_j) = 2\mu\hat{s}^2(t, X_i, X_j) + \lambda\hat{s}^2(t, X_i, X_j)\,, \tag{3.7}$$

and the energy $\underline{W}_{\mathrm{M}} : [0,T] \times \mathbb{R}^3 \to \mathbb{R}$ inside the interaction zone $B_\epsilon(X_i)$ is given by

$$\underline{W}_{\mathrm{M}}(t, X_i) = \sum_{X_j \in B_\epsilon(X_i)} 2\mu \hat{s}^2(t, X_i, X_j) + \lambda \hat{s}^2(t, X_i, X_j)\,. \tag{3.8}$$

And now the discretized energy $\underline{W}_{\mathrm{D}}$ can be compared to the classical energy $\underline{W}_{\mathrm{M}}$ for different amount of neighbors $|B_\epsilon(X_i)|$ inside the interaction zone $B_\epsilon(X)$. Only the first ten time steps are considered, because the assumption for the energy equivalence is only valid for small deformations, such that the pair-wise force $\underline{f}$ (2.56) stays in the linear regime.

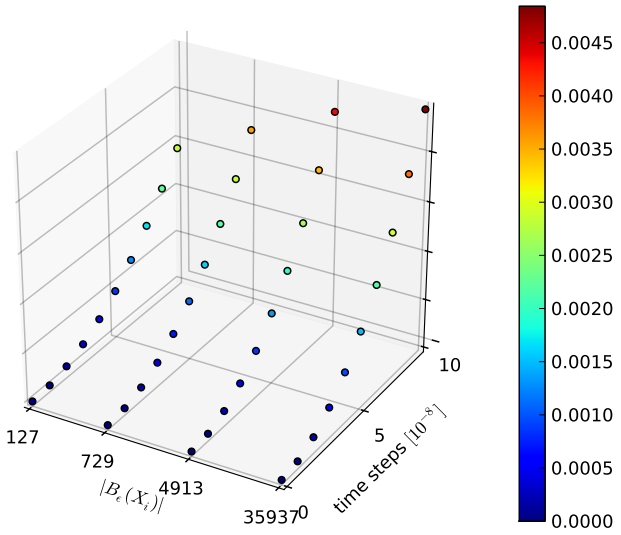

Figure 3.3.: The normalized error $|\underline{W}_{\mathrm{D}} - \underline{W}_{\mathrm{M}}|/|B_\epsilon(X_i)|$ between the discrete PD energy $\underline{W}_{\mathrm{D}}$ (3.4) and the model energy $\underline{W}_{\mathrm{M}}$ (3.8) for small deformations.

Figure 3.3 shows the normalized error $|\underline{W}_{\mathrm{D}} - \underline{W}_{\mathrm{M}}|/|B_\epsilon(X_i)|$ for the comparison of the discretized energy $\underline{W}_{\mathrm{D}}$ (3.4) and the model energy W_{M} (3.8). First, the error is for the first ten time steps sufficiently small in the range 10^{-2} for 127 neighbors up to $35\,937$ neighbors inside the interaction zone $|B_\epsilon(X_i)|$. Second, the error is in the same range for a small amount of neighbors $|B_\epsilon(X_i)| = 127$ and a significantly larger amount of neighbors $B_\epsilon(X_i) = 35937$. This, indicates that the material parameters α and β of the bond-based softening model are independent of the

horizon and the horizon can be seen as the length scale associated with the process zone. The disctretized bond-based peridynamic equation of motion (3.1) for a specific softening model (Section 2.3.2) with the EMU nodal discretization results with acceptable errors with respect to the classical theory. In Section 5.3 the bond-based softening model is validated against the Young's modulus E and the Poisson's ratio ν. There, the definition of these two material properties from classical theory is used to obtained them in the simulations.

3.2. How to choose the horizon δ ?

In [Du16a] an overview, which is briefly summarized here, on non-local vector calculus, non-local calculus of variations, and well-definedness of peridynamics (PD) solutions is given. There, following mathematical questions are addressed for gaining a better mathematical understand of peridynamics:

- Are peridynamics models well-posed, such that unique solutions exist?
- Are there relations between non-local peridynamics models, differential equation models in classical continuum mechanics, dynamics of interaction particles and molecular dynamics?
- Are there characteristics of solutions in PD models, such that regularity properties or singular behavior of solutions?

First, the first bullet point of well-definedness of PD solutions is addressed. Fore more details see [SL10; ELP13]. For linear bond-based PD the existence and uniqueness of solutions for a one-dimensional bar is shown in [EW07b]. More general pair-wise force functions are studied in [DZ11]. Non-linear initial value problems in one-dimension are studied in [EEM12] and one-dimensional scalar non-local conservation laws in [Du+12a]. In [EP13] non-linear bond-based PD with globally Lipschitz continuous pair-wise force functions are analyzed. The existence for non-local variational problems is given in [BM14] and for more general state-based peridynamics models see [MD15]. In [ZD10] two-dimensional bond-based models are addressed and multiple dimensions bond-based PD models are studied in [AP11].

With the framework non-local vector calculus [Du+12b; Du+13b; Du+13a] it can be shown that non-local equations are well-posed on bounded domains with

various non-local boundary conditions. Well-definedness of linear and non-linear PD models with more general assumptions can be done with non-local calculus of variations [MD13; MD14b; MD14a; MD15].

Second, consistency between non-local models and their local limits is emphasized. Therefore, numerical approximations of peridynamic models (e.g. asymptotically compatible schemes [TD14; ZD10]) are considered. For the consistency between nearest-neighbor peridynamic discretizations and discretized classical elasticity models see [SDP16]. The questions related to the choice of the horizon and the nodal spacing:

- Are there relations between the solution $u_{\delta,0}$ of the PD model and the solution $u_{0,0}$ of the limiting classical PDE model as the horizon δ increases to zero?
- How does the numerical scheme of the PD solution $u_{\delta,\Delta x}$ behaves when the horizon δ increases to zero? Does $u_{\delta,\Delta x}$ converge to $u_{0,\Delta x}$, which is the numerical approximation of $u_{0,0}$?
- How does the numerical approximations $u_{\delta,\Delta x}$ behaves when the horizon δ goes to zero and the nodal spacing Δx goes to zero? Does $u_{\delta,\Delta x}$ converge to $u_{0,0}$?

addressed in [Du16b] are briefly discussed here. Figure 3.4 shows the different cases $u_{\delta,\Delta x}$,$u_{0,\Delta x}$,$u_{\delta,0}$, and $u_{0,0}$ of non-local models with respect to the horizon δ and the nodal spacing Δx [DT15; Du16b].

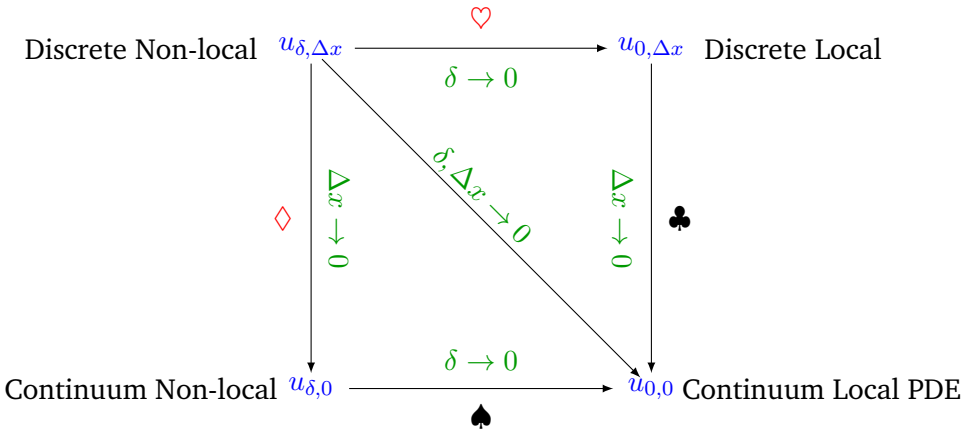

Figure 3.4.: Different cases $u_{\delta,\Delta x}$,$u_{0,\Delta x}$,$u_{\delta,0}$, and $u_{0,0}$ of non-local models with respect to the horizon δ and the nodal spacing Δx [DT15; Du16b].

Now, the focus is on the connection between the different cases, so-termed with ♡,♢,♠, and ♣, where one of the parameters δ and Δx is fixed and the other parameter goes to zero. The connection ♣ from discrete local to continuum local PDE is studied in the field of numerical PDEs and is well understood. The connection between non-local and local solutions is so-termed with ♠. Convergence of the discretization to the non-local model is conformed by the connection ♢.

The connection ♡ is the most intriguing one, because it is not clear whether the local limit of the numerical schemes for non-local problems would remain to be an effective scheme for local limit problems [Du16b]. With a possible positive answer, both connections ♢ and ♠ or ♡ and ♣ could be used for convergence of $u_{\delta,\Delta x}$ to $u_{0,0}$. In a mathematical point of view the connections in Figure 3.4 would be commutative.

Furthermore, the diagonal connection, where the horizon and the nodal spacing go proportionally to zero is an possible numerical scheme. Here, for piece wise constant finite element the correct local limit solution can be obtained as long as the nodal spacing decays faster than the horizon of the interaction zone [DT15]. In [TD13] is demonstrated that the EMU ND converges to the local limit $u_{0,0}$ (Figure 3.4) if the nodal spacing $\Delta x \to 0$ decays faster than the horizon $\delta \to 0$. For more details see [TD14].

One empirical choice of δ of $B_\delta(X_i)$ for a specific material is to adjust it, such that the model reproduce the same dispersion curves as those measured for the material [Sil11]. Hence, the obtained horizon δ may works for this one specific material, but may not for a different material. In Section 5.2 a study for the critical traction in Mode *I* crack opening for different proportions of δ and Δx is done for a wide range of material from polymethyl methacrylate up to titanium alloy. Since there is no theoretical indication how to choose the proportions of the horizon and the nodal spacing.

3.3. Discrete Prototype Microelastic Brittle Material Model

Here, the Prototype Microelastic Brittle (PMB) model is adjusted to the EMU nodal discretization (EMU ND), because the PMB model assumes that all material points have the same amount of neighbors inside the interaction zone and the same volume

of the interaction zone. Thus, all nodes have the same stiffness constant (2.35), which depends on the bulk modulus and the horizon, and the same critical stretch for bond failure (2.40), which depends on the bulk modulus, the critical stress intensity factor, and the horizon. For non-homogeneous materials, modeling material defects or handle the skin effect (Figure 3.2b), a non-uniform spatial partitioning is preferable. For more details read [GHM14; Sil+07]. Next, a brief description how the position depended stiffness constant $\overline{c}(X_i, X_j)$ and critical stretch for bond failure $\overline{s}_c(X_i, X_j)$ are obtained is given.

In the PMB model the stiffness constant $c_{K,\delta}$ (2.35) is derived from the analytic solution of the integral in (2.34) for the peridynamics strain energy density W_{PD} (2.33). Using the EMU ND as discretization, the integral can approximated via the summation over all neighbors inside the interaction zone $B_\delta(X_i)$. Hence, the discrete PD energy density $\overline{W}_{\text{PD}} : [0,T] \times \mathbb{R}^3 \to \mathbb{R}$ yields

$$\overline{W}_{\text{PD}}(t, X_i) = \frac{1}{2} \sum_{B_\delta(X_i)} \overline{\omega}(t, x(t, X_j) - x(t, X_i), X_j - X_i)\mathbf{V}_j \,, \tag{3.9}$$

where $\overline{\omega} : [0,T] \times \mathbb{R} \times \mathbb{R} \to \mathbb{R}$ is a valid micro potential for a large homogeneous deformation

$$\begin{aligned}\overline{w}(t, x(t, X_j) - x(t, X_i), X_j - X_i) = \\ \frac{1}{2}\mathbf{w}(X_j, X_i)\overline{c}(X_i)s^2(t, x(t, X_j) - x(t, X_i), X_j - X_i)\,.\end{aligned} \tag{3.10}$$

For the energy equivalence with the classical strain energy density $\overline{W}_2(\mathbf{s}) = {}^{(9K\mathbf{s}^2)}/_4$ in two dimensions, the assumptions, that for the weights in the interaction zone $\sum_{X_j \in B_\delta(X_i)} \mathbf{w}(X_i, X_j) \equiv 1$ holds and for the over all stretch in the interaction zone $\mathbf{s} \equiv \sum_{X_j \in B_\delta(X_i)} s(t, x(t, X_j) - x(t, X_i), X_j - X_i)$ holds, are made. With these assumptions the discrete PD strain energy density $\overline{W}_{\text{PD}}$ can be rewritten as

$$\begin{aligned}\overline{W}_{\text{PD}}(t, X_i) &= \frac{1}{2} \sum_{B_\delta(X_i)} \overline{w}(t, x(t, X_j) - x(t, X_i), X_j - X_i)\mathbf{V}_j \\ &= \frac{1}{2} \sum_{B_\delta(X_i)} \frac{1}{2}\mathbf{w}(X_j, X_i)\overline{c}(X_i)s^2(t, x(t, X_j) - x(t, X_i), X_j - X_i)\mathbf{V}_j \\ &= \frac{1}{4}\mathbf{s}^2 \sum_{B_\delta(X_i)} \overline{c}(X_i)\mathbf{V}_j \,.\end{aligned} \tag{3.11}$$

Now, the energy equivalence with the classical strain energy density $\overline{W}$ is done, because the energy stored in the bonds is equivalent to it

$$\begin{aligned} \overline{W}_{PD} &\stackrel{!}{=} \overline{W} \\ \frac{1}{4}\mathbf{s}^2 \sum_{B_\delta(X_i)} \overline{c}(X_i)\mathbf{V}_j &= \frac{9K\mathbf{s}^2}{4} \\ \overline{c}(X_i) &= \frac{9K}{\sum\limits_{B_\delta(X_i)} \mathbf{V}_j}\,. \end{aligned} \tag{3.12}$$

Note, that here the differing amount of neighbors inside $B_\delta(X_i)$ take in account and each node has a different stiffness constant instead as the full volume of the interaction zone as in (2.35). Thus, the conservation of linear momentum (2.27) does not hold and therefore the average $\overline{c}(X_i, X_j) := {}^{(\overline{c}(X_i)+\overline{c}(X_j))}/_2$ is introduced.

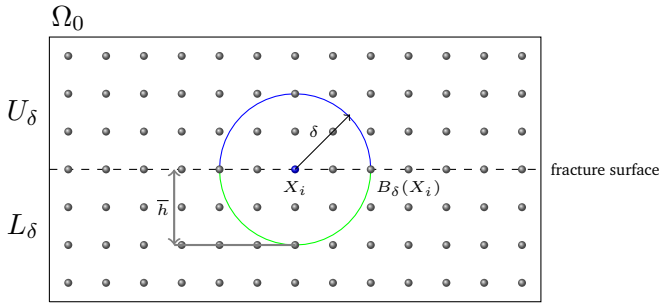

Figure 3.5.: To obtain the PD energy release rate $\overline{G}_{\text{PD}}$ in two dimensions, which relates to the energy release rate G from classical theory. This expresses the energy, which is dissipated during the fracture, for creating the newly fracture surface. Here, the PD energy density is determined by integrated over the interaction zone $B_\delta(X_i)$ by varying the height $\overline{h}$ of the fracture surface.

To obtain the critical stretch (for bond failure) $\overline{s}_c(X_i, X_j)$ look at the two dimensional plane, see Figure 3.5, and assume the energy release rate $\overline{G}_{\text{PD}}$ is obtained by the integration of the energy density $\overline{\omega}$ overall fracture surfaces with the height $\overline{h}$. The

volume $\overline{\mathbf{V}} : \mathbb{R} \times \mathbb{R} \to \mathbb{R}$ is the thickness $\bar{t}$ of the plate multiplied by the area of the circular segment

$$\overline{\mathbf{V}}(\delta, \overline{h}) = \bar{t}\delta^2 \arccos\left(\frac{\delta - \overline{h}}{\delta}\right) - \left(\delta - \overline{h}\right)\sqrt{2\delta\overline{h} - \overline{h}}\,. \tag{3.13}$$

Now, the PD energy release rate $\overline{G}_{\text{PD}} : [0, T] \times \mathbb{R}^3 \to \mathbb{R}$ for breaking all bond between U_δ and L_δ and let the fracture surface grow is given by

$$\begin{aligned}\overline{G}_{\text{PD}}(t, X_i) &= 2\overline{w}(t, x(t, X_j) - x(t, X_i), X_j - X_i) \int_0^\delta \overline{\mathbf{V}}(\delta, \overline{h}) dh \\ &= \frac{2}{3}\mathbf{s}^2\bar{t}\overline{c}(X_i, X_j)\delta^3\,. \end{aligned} \tag{3.14}$$

With the same energy equivalence as for the PMB model the critical stretch $\overline{s}_c(X_i, X_j)$ is obtained as

$$\begin{aligned}\overline{G}_{\text{PD}} &\stackrel{!}{=} \overline{G} \\ \frac{2}{3}s^2\bar{t}\overline{c}(X_i, X_j)\delta^3 &= \frac{8}{9}\frac{K_{\text{Ic}}^2}{K} \\ \mathbf{s} &= \sqrt{\frac{8K_{\text{Ic}}^2}{6\bar{t}\overline{c}(X_i, X_j)\delta^3}}\,. \end{aligned} \tag{3.15}$$

From the energy equivalence the critical stretch $\overline{s}_c(X_i, X_j)$

$$\overline{s}_c(X_i, X_j)_{K, K_{\text{Ic}}, \delta, \bar{t}} = \sqrt{\frac{8K_{\text{Ic}}^2}{6\bar{t}\overline{c}(X_i, X_j)\delta^3}} \tag{3.16}$$

depends on K, K_{Ic}, δ, and the thickness $\bar{t}$.

Note, that this model address a surface correction, but does not emphasize the numerical integration error of the EMU nodal discretization. Table 3.1 shows the comparison of the stiffness constant c and the critical stretch for bound failure s_c for bond-based PMB model and the bond-based DPMB model. In Section 5.1 the DPMB is used to simulate wave propagation and the obtained front wave speed is compared with experimental data. The comparison with the critical traction for Mode *I* crack opening with the Linear Elastic Fracture Mechanics is done in Section 5.2.

	PMB	DPMB
Stiffness constant	$c_{K,\delta} = \frac{18K}{\pi\delta^4}$	$\overline{c}(X_i)_{K,\delta} = \frac{9K}{\sum_{B_\delta(X_i)} \mathbf{V}_j}$
Critical stretch	$s_{c_{K,K_{\text{Ic}}^2,\delta}} = \frac{5}{12}\sqrt{\frac{K_{\text{Ic}}}{K^2\delta}}$	$\overline{s}_c(X_i, X_j)_{K,K_{\text{Ic}},\delta,\bar{t}} = \sqrt{\frac{8K_{\text{Ic}}^2}{6\bar{t}\overline{c}(X_i, X_j)\delta^3}}$

Table 3.1.: Comparison of the stiffness constant c and the critical stretch for bond failure s_c for the PMB model and DPMB model.

4.Implementation and Post-processing

Particle methods or nodal methods, like smoothed particle hydrodynamics (SPH) [GM77], molecular dynamics (MD) and peridynamics (PD), are very common nowadays. They are typically applied in material science to simulate crack and fractures. For discretization the search for neighboring nodes inside a finite interaction zone has some benefits for parallel implementations. Finding neighbors is a large part of the overall computation time and due to the often weak convergence properties of these methods, very large node clouds $\mathbf{C}$ need to be employed in high fidelity simulations. If the interaction of forces does not solely depend on the reference configuration Ω_0, additional searches for neighbors for the computation of short-range forces or contact forces need to be applied. In subsection 4.1 a generic sorting-based approach for finding the k–nearest neighbors or neighbors inside a sphere (a circle in 2D) is presented. The resulting library, the Fast neighbor search on GPU (FNSG), contains following additional features: computation of contact forces and modeling initial cracks by defining a two dimensional plane, where all straight lines between nodes, crossing this plane are left out as neighbors.

A different aspect is the coupling [Lub+12] of often computational expensive non-local methods with the FEM [LH12a; KM10; Lit10; Ote+12; AGM12] or the partition of unity method (PUM) [SW14; MS14]. Here the aim is to apply the computational expensive non-local method in the area of interest, where cracks emerge or crack paths bifurcate and the other (computational cheaper) methods outside the area of interest. Subsection 4.2 emphasizes a approach to integrate Compute Unified Device Architecture (CUDA) into the asynchronous execution graph of High Performance ParallelX framework (HPX). Here the non-local method is implemented on the GPU with CUDA, because of the advantage of load balancing [BB87; LH12b]. Within the HPX compute language (HPXCL) framework the implementation can be fully asynchronous coupled with the implementation on the CPU, where the other method is simulated.

The verification and the analysis of simulation results against experimental data is essential for validating simulations. The Section 5.1 the PMB material and the DPMB material model is compared to the Edge-On impact experiment. Here, the extraction of the wave front of the node-based data was quite challenging. In Section 4.3.2 a technique based on standard volume rendering for the visualization of stress waves after impact damage is presented. A different scenario is the extraction of fragments

after an impact. Here, the distribution of the fragments with respect to their mass or velocity at the center of mass are from interest. There a comparison with the impact experiments described in [Vog+03; SH05] could be considered as a future comparison. An extension for the connected component algorithm [Die+ed] is employed in Section 4.3.1 to extract fragments from the node-based PD data.

4.1. Fast neighbor search on GPU

An efficient and general sorting-based approach for the neighbor search on a Graphics Processing Unit (GPU) [PM14], which overcomes the computational complexity $\mathcal{O}(n^2)$ of the naïve neighbor search, is presented. In the naïve the distance $\|X_i - X_j\|$ of each node X_i to all other nodes X_j is computed. One of the most renowned single-core libraries is ANN [MA10]. However, to deal with very large node clouds, necessary for accurate simulations results today, the node neighborhoods need to be computed in parallel. Here, also a number of libraries exist for shared-memory [Ary+94; NN97; TH81] and distributed-memory [Mic09; Pli95] parallel computers. For general-purpose computing on graphics processing units (GPGPU) following implementations [DKD13; Lei+12] are available.

The algorithm rests upon the approach presented in [Mic09]. According to [Mic09] the algorithm is designed for better efficiency on multi-core machines due to low memory usage and good cache efficiency. For GPGPU low memory usage and good cache efficiency are important indicators of the performance on the GPU. These benefits of the algorithm and its complexity $\mathcal{O}(\lceil n/p \rceil m \log(m))$, where n donates the number of nodes, p the number of threads and m the number of neighbors, offers a good initial situation for an implementation on the GPU.

Figure 4.1 shows sketches of the node clouds considered as references for the implementation of this library. Initial node configuration in the reference configuration Ω_0 are often uniformly distributed for methods like PD, MD [GKZ07] and, smoothed particle hydrodynamics (SPH). Thus, a regular node arrangement and a uniformly distributed, but irregularly spaced node cloud, is considered. These initial node clouds are redistributed at later time steps in the simulation by the applied method. This may encounter large variations in the node density. As a benchmark these reference cases are considered for the evaluation of this algorithm.

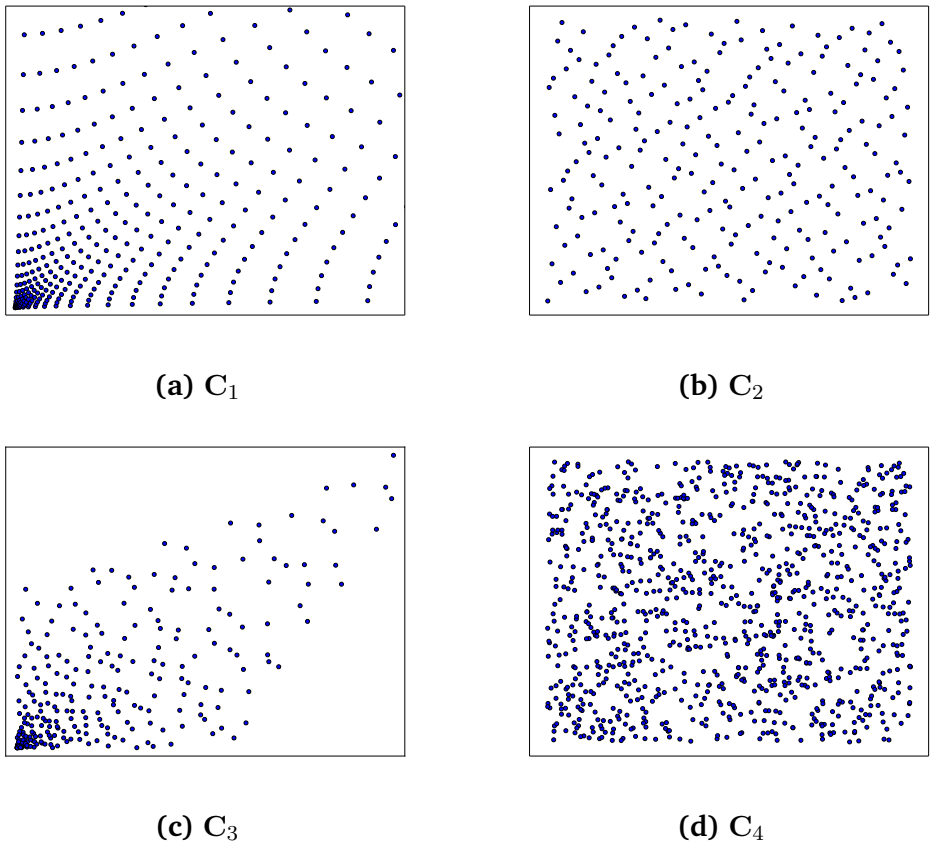

(a) $\mathbf{C}_1$ **(b)** $\mathbf{C}_2$

(c) $\mathbf{C}_3$ **(d)** $\mathbf{C}_4$

Figure 4.1.: Sketch of reference node clouds: (a) graded node cloud of a regular grid $\mathbf{C}_1$, (b) nodes of the Halton sequence $\mathbf{C}_2$, (c) graded Halton sequence $\mathbf{C}_3$ and, (d) uniformly distributed random nodes $\mathbf{C}_4$. The node clouds $\mathbf{C}_1$ and $\mathbf{C}_3$ were graded with $g(X_i) = ||X_i||^2 X_i$.

4.1.1. Implementation

Let us shortly review the fundamental algorithm [Mic09], which will serve as the basis for our massive parallel implementation using the CUDA. The algorithm bases on the idea to sort the nodes with respect to a space-filling curve (SFC). This is a very successful and widely used approach for sorting multidimensional data with respect to topological information [WS93; Bad13; SSL13; BBK01; MWK01; AS97; M A03]. Such a sorting strategy is essentially realized via the following four steps (see also Algorithm 4.1).

1. Generating keys: The multidimensional node cloud $\mathbf{C}$ is transformed with $T : \mathbb{R}^d \to \mathbb{R}$, which is the inverse of a SFC. Thus, a one dimensional key $k_i = T(X_i)$ is assigned to every node $X_i \in X_{\text{ND}}$.
2. Sorting keys: These one-dimensional keys k_i can easily be sorted and induce a respective ordering of the nodes $X_i \in X_{\text{ND}}$.
3. Range scan: Moreover it is easy to identify "neighbor keys" in one dimension to obtain a good initial guess $\tilde{N}(N_i)$ for the geometric neighbors in multidimensions of a particular node X_i.
4. Geometrical validation: Finally, we need to check if all geometrical neighbors $X_j \in X_{\text{ND}}$ of node $X_i \in X_{\text{ND}}$ are already found.

In the following this approach is discussed with respect to the implementation on a GPU. In a SFC-method, a multidimensional node $X_i \in \mathbb{R}^d$ is transformed to a (large) integer value $T(X_i) = k_i \in \mathbb{N}$, which can then be easily sorted. Thus, the transformation $T : \mathbb{R}^d \to \mathbb{N}$ is essentially influencing the computational costs and the quality of the resulting ordering of the data. There exists plenty different space filling curves, e.g Hilbert curve, the Peano curve, Lebesque curve, also referred as Morton Order, which can potentially be employed. One early application of the Morton Order is efficient range searching of multidimensional data in dynamically balanced trees [TH81]. The Morton Order as a transformation $T : \mathbb{R}^d \to \mathbb{N}$ is computationally cheap, but provides some sub-optimal locality. To clarify this issue let us consider the generation and comparison of keys for the Morton Order in the following.

$$X_1 = \begin{pmatrix} 0 \\ 3 \end{pmatrix}_{b=10} = \begin{pmatrix} 000 \\ 0111 \end{pmatrix}_{b=2} \xrightarrow{T(X_1):\mathbb{R}^2\to\mathbb{N}} (000101)_{b=2} \tag{4.1}$$

Equation (4.1) shows the transformation of the node $X_1 := (0, 3)^T$ to the key $k_1 =: T(X_1)$. First the coordinates of the node in base 10 are converted to base 2 and then mapped to the scalar key $(x_0y_0x_1y_1x_2y_2)_{b=2}$ in base 2 by bit-interleaving. Equation (4.2) shows the comparison of two nodes $X_1 = (0, 3)^T$ and $X_2 = (1, 2)^T$ using the Morton Order compare operator $\leq_M$.

$$T(X_1) = T\begin{pmatrix} 0 \\ 3 \end{pmatrix} = (000101)_{b=2} \leq (000110)_{b=2} = T\begin{pmatrix} 1 \\ 2 \end{pmatrix} = T(X_2) \tag{4.2}$$

Algorithm 4.1: Origin algorithm described in [Mic09]. The steps highlighted in blue are discussed in this subsection, because these need to be adapted for the implementation on the GPU.

Data: Morton order compare operator $\leq_M$ and node cloud $\mathbf{C}$
Result: m-nearest neighbors $\forall X_i \in \mathbf{C}$
$\leftarrow$ ParallelSort($\mathbf{C}, \leq_M$);
for $X_i \in C$ **do**
  $A_i \leftarrow nn^m(X_i, \{X_{i-m}, \ldots, X_{i+m}\})$;
  if $X_i^{\lceil rad(A_i) \rceil} < X_{i+m}$ **then**
    $u \leftarrow i$
  else
    $I \leftarrow 1$; **while** $X_i^{\lceil rad(A_i) \rceil} < X_{i+2^i}$ **do** $++I$;
    $u \leftarrow \min(i + 2^I, n)$;
  end
  if $X_i^{-\lceil rad(A_i) \rceil} > X_{i-m}$ **then**
    $l \leftarrow i$;
  else
    $I \leftarrow 1$; **while** $X_i^{-\lceil rad(A_i) \rceil} > X_{i-2^i}$ **do** $++I$;
    $l \leftarrow \min(i - 2^I, n)$;
  end
  if $l \neq u$ **then**
    CSearch(X_i, l, u);
  end
end

The computational effort of the comparison $T(X_1) \leq T(X_2)$ is small, since it involves only 2 operations: the exclusive-or operation and the most significant bit (MSB) operation deliver the result. Thus, the largest cost of the computational work associated with the Morton Order compare operator

$$X_1 \leq_M X_2 \Leftrightarrow T(X_1) \leq T(X_2) \tag{4.3}$$

is associated with the respective computation of the respective keys $T(X_1)$ and $T(X_2)$.

Applying the Morton order compare operator to the nodes of a uniform 4×4 grid yields to the ordering depicted in Figure 4.2. From this plot we find that we assign "adjacent" keys to the nodes $X_3 = (3, 1)^T$ and $X_4 = (0, 2)^T$. Thus, these nodes are

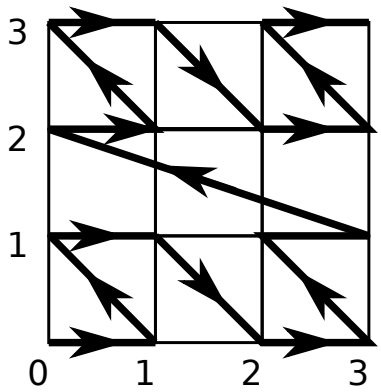

Figure 4.2.: The resulting space-filling curve with the Morton Order compare operator $\leq_M$ on a uniform grid with 4×4 nodes. Because of its shape, the curve is also called Z–Curve.

"neighbors" with respect to the Morton order, but not with respect to their euclidean distance. Other space-filling curves, e.g. the Hilbert curve, may provide a better data locality but the computational costs associated with the respective key generation or compare operator may be much larger.

We obtain an initial estimate of the m-nearest neighbors of a node x_i by selecting $m/2$ nodes x_j with the largest keys $k_j = T(X_j) \leq k_i = T(X_i)$ and $m/2$ nodes with the smallest keys $k_j \geq k_i = T(X_i)$ and collect these keys in the set $\hat{N}(k_i)$. This initial guess $\tilde{N}(x_i) = \{X_j | T(X_j) = k_j, k_j \in \hat{N}(k_i)\}$ then needs to be validated, i.e. we need to check if $\hat{N}(k_i)$ in fact contains the nodes X_j which are closest to X_i.

To this end, the Morton order divides a d-dimensional unit cell recursively in 2^d sub cells. In each sub cell there exist two keys $q = T(X)$ and $p = T(X')$, so that all nodes X_l with $q \leq T(X_l) < p$ are included in this sub cell. To validate the initial guess $\tilde{N}(X_i)$, we have to check if the smallest key q and the largest key p are included in $\hat{N}(k_i)$. Otherwise, the range of the set $\hat{N}(k_i)$ needs to be extended. Algorithm 4.2 describes the extension of the set using some geometrical information about the sub cells. Note that we use $\upsilon = 4$ as suggested in [Mic09] and have not yet optimized this parameter for the GPU. The described transformation T is so far suitable for node clouds with integer values as coordinates. With the extensions, described in [Mic09; Cha06], the Morton Order $\leq_M$ compare operator handles floating node values and multidimensional input data with $d > 3$.

Thus, in summary the operations to generate the keys and handle recursiveness in Algorithm 4.2 on the GPU need to be provided. To provide the exclusive-or operation and the most significant bit (MSB) operation, which are not available in the standard library on a GPU, a new data type for the IEEE 754 representation of float and double, to access the exponent and the mantissa of the respective double or floating values of the nodes, needs to be defined.

Another issue for the implementation on a GPU are the recursive calls of Algorithm 4.2, because the programming model on the GPU does not support "real" recursiveness in kernel functions. The kernel function is launched on the device with a specified grid of blocks. Then, a device function is called, recursively, within a kernel function. Thus, some recursive calls need to be implemented with the help of device functions and the grid of blocks need to be adjusted, because of the single instruction multiple threads (SIMT) architecture, depending on the employed GPU.

Parallel sorting

The increasing popularity of GPGPU provides many standard sorting algorithms for GPU [SHG09; SA08]. The library Thrust [Wen11], a powerful library of parallel algorithms and data structures, was extended with CUDA support and is now integrated in the CUDA SDK. The Thrust library contains the data structure *vector*, to store the multidimensional input data, in our case the node locations X_j, and an optimized parallel merge sort algorithm, which utilizes a user defined *StrictWeakOrdering comp* which we realize with the help of $\leq_M$, see Equation (4.3).

4.1.2. Results

The algorithm provided in the Fast neighbor search on GPU (FNSG) library is compared to the STANN [CK10] library in version 0.74, a single-threaded CPU implementation of the origin algorithm. Table 4.1 lists the compiler and hardware used for this benchmark. Figure 4.3a shows the comparison for the random point cloud C_4 in two dimensions and three dimensions for both libraries for finding the 100-nearest neighbors in a unit square or respective a unit cube. Figure 4.3b shows the results for the graded node cloud of a regular grid $\mathbf{C}_1$. For more details about the comparison of these two libraries see [PM14].

Algorithm 4.2: Function *CSearch(...)* [Mic09] extends the range of the set $\{X_{i-cm}, \ldots, X_{i+cm}\}$ with using some geometrical information about the generated sub cubes.

Data: Node X_i, lower range l and upper range u
Result: Extended range for neighbors with additional geometrical information

```
CSearch(X_i, l, u) ;
if (h − l) < υ then
    A_i ← nn^m(X_i, A_i ∪ {X_{i−m}, ..., X_{i+m}}) ;
    return
end
b ← (u + l)/2 ;
A_i ← nn^m(X_i, A_i ∪ p_b) ;
if dist(p_i,box(X_l,X_h)) ≥ rad(A_i) then
    return
end
if X_i < X_b then
    CSearch(X_i, l, b − 1);
    if X_b < X_i^⌈r(A_i)⌉ then
        CSearch(X_i, b + 1, u);
    end
else
    CSearch(X_i, b + 1, u);
    if X_i^−⌈r(A_i)⌉ < X_b then
        CSearch(X_i, l, b − 1);
    end
end
```

The approach presented in [Mic09] delivers the m-nearest neighbors of a node X_i. This algorithm was extended to deliver all neighbors inside an interaction zone $B_\delta(X_i) := \{X_j | \, \|X_j - X_i| \leq \delta\}$ for all nodes X_i in the node cloud $\mathbf{C}$. The reference node clouds $\mathbf{C}_1, \ldots, \mathbf{C}_4$ in Figure 4.1 were generated on the unit square $[0,1] \times [0,1]$ and a unit cube $[0,1] \times [0,1] \times [0,1]$. The overall computational time for the extended algorithm to find all neighbors inside the interaction zone for $\delta = 0.1$ is shown in Figure 4.4.

Figure 4.4a shows the result for the Halton sequence $\mathbf{C}_2$ and the uniformly distributed random nodes $\mathbf{C}_4$ for the unit cube. Here, the asymptotic behavior for

	CPU	GPU
Compiler	gcc 5.3	nvcc 5.5
Hardware	Intel M-5Y10c @ 0.80GHz	Nvidia Tesla K20c
OS/Driver	Fedora 23 (4.3.4)	Nvidia-SMI 346.46

Table 4.1.: System information and compiler version for the benchmark of the libraries.

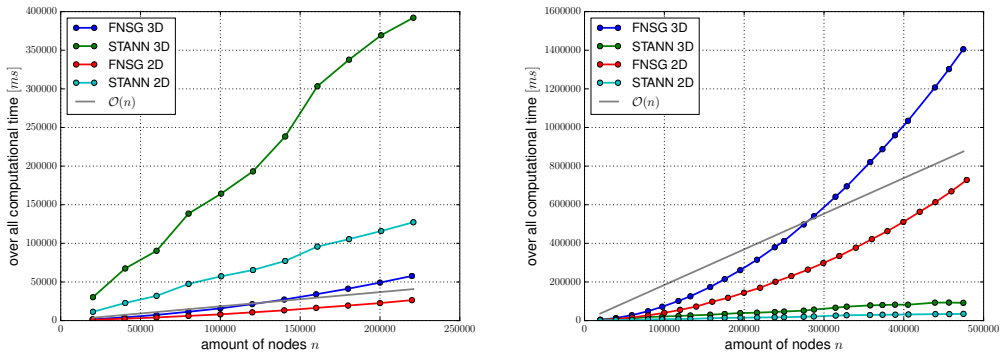

(a) Uniformly distributed random nodes **(b)** Graded nodes of a regular grid

Figure 4.3.: Comparison of the FNSG and STANN library for uniformly distributed random nodes $\mathbf{C}_4$ and graded nodes of a regular grid $\mathbf{C}_1$ in two dimensions $[0,1] \times [0,1]$ and three dimensions $[0,1] \times [0,1] \times [0,1]$.

both node clouds looks the same. Figure 4.4c shows the same asymptotic behavior for the node clouds on the unit square, but here the sub-optimal locality of the Morton order takes in account and the overall computational time increases. For the graded node clouds $\mathbf{C}_1$ and $\mathbf{C}_3$ on the unit square the computational effort for both node clouds differs marginal. For the three dimensional case of the graded node clouds the sub-optimal locality of the Morton order is seen peaks in the curves (Figure 4.4b). To overcome this issue of the sub-optimal locality the transformation of the node cloud could be replaced with a different SFC, e.g. the Hilbert curve.

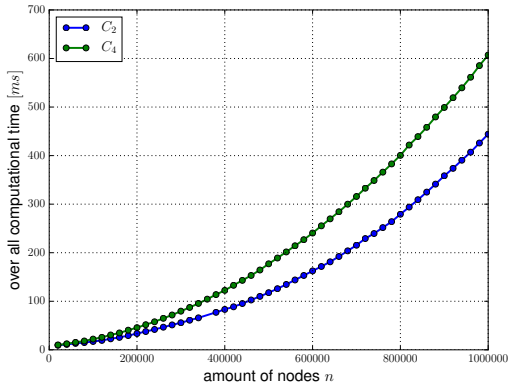

(a) Node clouds: $\mathbf{C}_2$ and $\mathbf{C}_4$ for $\mathbb{R}^3$

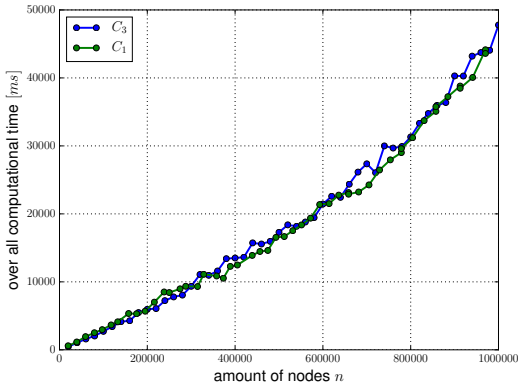

(b) Node clouds: $\mathbf{C}_1$ and $\mathbf{C}_3$ for $\mathbb{R}^3$

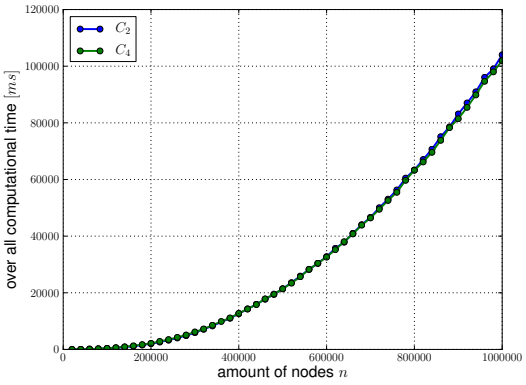

(c) Node clouds: $\mathbf{C}_2$ and $\mathbf{C}_4$ for $\mathbb{R}^2$

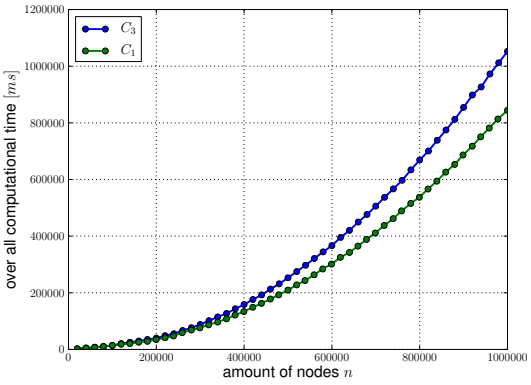

(d) Node clouds: $\mathbf{C}_1$ and $\mathbf{C}_3$ for $\mathbb{R}^2$

Figure 4.4.: Overall computational time on a Nvidia Tesla K20c for the reference node clouds:(a) graded node cloud of a regular grid $\mathbf{C}_1$, (b) nodes of the Halton sequence $\mathbf{C}_2$, (c) graded Halton sequence $\mathbf{C}_3$, and (d) uniformly distributed random nodes $\mathbf{C}_4$.

4.2. Integration of CUDA to the High Performance ParallelX framework

For today's high performance systems experience shows that the utilization of different acceleration cards in conjunction with a high utilization of all other parts of the system is quite difficult. For the future direction to exascale computing, the high utilization of all available resources, including local and remote acceleration

cards on a cluster while using all available CPU resources is necessary [Adv12]. On many super computers in the Top 500 a large part of the compute power in terms of FLOPS is provided by various acceleration cards and co-processor boards. The integration of these cards requires special effort from side of the programmer for managing the heterogeneous code base and explicitly managing the data transfer from and to the acceleration card and the synchronization of the execution of kernels. To utilize the full capability of the cluster a) the main cores need to be kept busy while kernels are executed on the GPU and b) the latencies and overheads of the data transfer from and to the device need to be hidden behind other useful work. Currently available solutions make it very hard to gain scalability, programmability and performance portability on heterogeneous super computers.

With the HPX compute language (HPXCL), a programming environment which overcomes the problems addressed above by transparently enabling asynchronous data transfers and kernel execution within CUDA while task are executed concurrently on the main cores, is provided. The concept of the programming environment is, that all GPU operations are represented as asynchronous task like the parallel tasks on the CPU. Thus, these tasks are integrated in the parallel execution graph of the High Performance ParallelX framework (HPX) [Kai+15b]. In Section 4.2.1 more details for the integration of the CUDA SDK in the parallel execution graph are emphasized. The integration into HPXCL is compared for some examples with the native CUDA implementation in Section 4.2.2.

4.2.1. Implementation

In this section the important ingredients of the HPX framework, specific for the integration of CUDA, are briefly introduced. The goal of HPX is to provide a unified programming model which transparently utilizes the full capability of the cluster to achieve unprecedented levels of scalability. To achieve this goal, the design of the API for the integration of CUDA is implemented to fit to the design of HPXCL-OpenCL.

Futurization

The futurization is an important part of the HPX concept for synchronization. The API provides the asynchronous return type `hpx::future<T>`. Note, that the return

type, a so-called future, is template-based and the specific return value of the called function is hidden in the future. Thus, the called function immediately returns, even if the result of the return value is not computed. The specific return value of the called function is accessible with the `.get()` operator of the future. For the synchronization of the immediately returned futures, the standard-conform API `hpx::future<T>::then` and `hpx::future<T>::wait_all` for composition and `hpx::dataflow` to build implicit parallel executions graphs [Kai+15a], are provided.

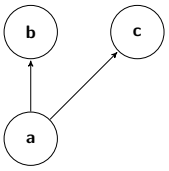

Figure 4.5.: Example dependency graph.

```
1 //Vector with all dependencies of a
2 std::vector<hpx::future<void>> dependencies;
3 dependcy.push_back(compute(b));
4 dependcy.push_back(compute(c));
5 hpx::wait_all(dependencies);
6 compute(a,b,c);
```

Listing 4.1: Modeling the dependency graph in Figure 4.5 with composition in HPX.

Listing 4.1 shows the usage of the futurization to resolve the simple dependency graph (Figure 4.5) with composition. For the integration of CUDA all functions, like the data transfer or the launching of a kernel, return a `hpx::future`. Thus, the data dependency of a kernel is modeled with the same concept and the resulting data of the kernel launch can be a dependency of a task on the host. Note, that all CUDA specific functions return the same type of future and it is possible to combine them with all other futures on the host side.

Design of the CUDA API

Figure 4.6 shows the classes derived from the programming concept of CUDA for the client-side objects, which are addressable via AGAS. Each local or remote GPU in the whole cluster is represented on the client-side as a `Device`. All available devices in the cluster are detected by HPXCL and the programmer can query them by specifying a CUDA minimum compute capability. The result is a vector with all available devices represented in AGAS. The device id is the identifier of each device on its locality. With this feature, all available CUDA devices are available for the utilization of the full cluster capability. Listing A.1 shows the functionality of HPXCL to discover all local and remote GPUs available in the cluster. Each device

is synchronized internally with CUDA streams and the synchronization between devices and hosts is implied using the futurization concept.

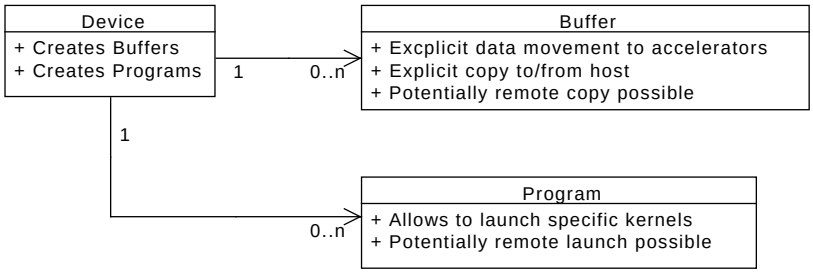

Figure 4.6.: Classes of the HPXCL-CUDA component which are globally addressable from all localities via AGAS on the host.

The physical memory of each device is organized with the class `Buffer`. The memory of the device is not globally addressable with AGAS. Therefore, a kind of wrapping is implemented. With the generation of an instance of this class, the requested memory is allocated on the device. Note, that a buffer is derived by a device and the combination of the locality and the device id are a unique identifier of the device. Depending on the memory, which is transferred to the device, resides on the same locality or on a different locality, an additional copy of the host memory with the serialization functionality of HPX is made. All transfers of the memory from or to the device are asynchronous and are synchronized with streams. The read or write operation of a buffer object returns a `hpx::future` which can be used for the synchronization with kernel launches and other tasks on the host.

The second object derived from a physical device is the class `Program`. Here, a difference from the compilation process of native CUDA code is applied. Writing pure CUDA code implies that the kernel and device functions are compiled with the Nvidia C/C++ compiler (nvcc). HPXCL-CUDA uses the Nvidia Runtime Compiler (nvrtc) to dynamically build the kernels on run time. The first benefit is that kernels can be optimized at compile time depending on the grid size and block size, e.g by unrolling loops.

Figure 4.7 shows the execution of a CUDA kernel with simplified calls of the methods to show the concept of concurrent execution and integration of the futurization concept of HPX. In this application, a kernel with size and data as parameters is applied and the result is computed in-place in the data parameter. In the first step two `Buffer`, to store size of the data and data itself are generated, and a `Program`

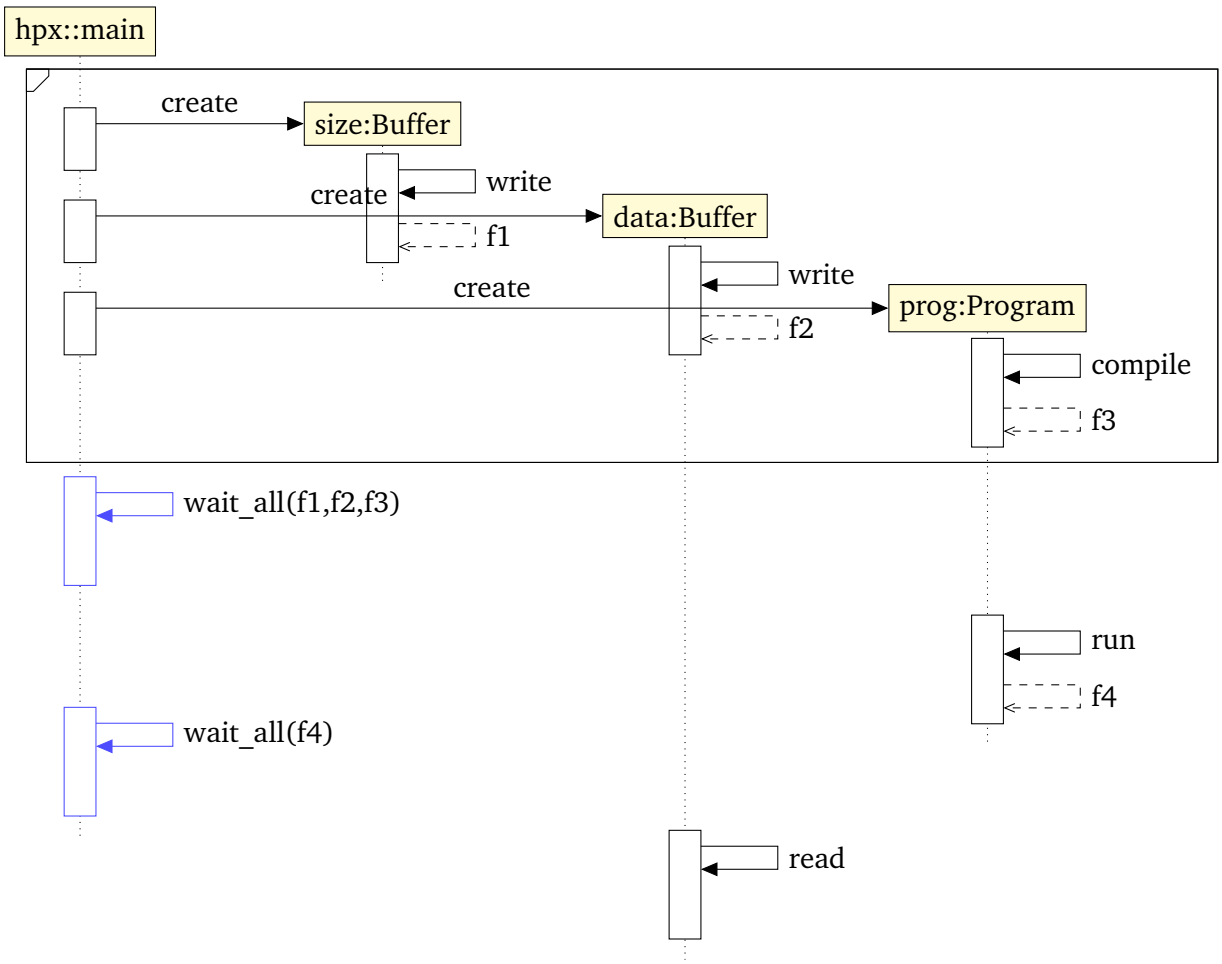

Figure 4.7.: Sequence diagram for the execution of a kernel and the synchronization with composition of HPX.

for the kernel. Note, that both writing data to the device memory and compiling the kernel at run time with the NVRTC library return a `hpx::future`. All of these operations are independent of each other and are executed concurrently on different HPX internal threads. For the execution of the kernel these operations need to be done and the first barrier for these three futures is defined with the `hpx::future<T >::wait_all` composition feature of HPX. Next, the kernel is executed and returns a future as well. Here, the future of the launch of the kernel can be combined with any other asynchronous tasks on the host. Thus, the execution of the host code and the device code is overlapped and the full capability of the system is addressed.

During the launch of the kernel, the next barrier for its future needs to be defined. After that, the data from the buffer can be copied back to the host and processed.

With the integration of data transfer and launching of the kernel into HPX with the HPXCL framework, the coordination of the control flow of accelerator cards with control flow on the host architecture, the advantage of the data flow and continuation style programming techniques is realized. Thus, synchronization of the data transfer with the launch of the kernel is hidden from the programmer.

4.2.2. Results

To measure the performance of the abstraction layer built on top of CUDA, two benchmarks were conducted. Both benchmarks were run on the Titan super computer, a CRAY XK7 with $18\,688$ nodes. For more details see Table 4.2. As a first

CPU	16 Core AMD Opteron 6274 Interlagos
RAM	32GB
GPU	Nvidia Tesla K20X
SDK	CUDA 7.0

Table 4.2.: Specification of the Titan super computer at the ORNL.

benchmark, a simple 3-Point stencil $s(X_i) := 0.5X_{i-1} + X_i + 0.5X_{i+1}$ is applied on the one-dimensional node cloud $\mathbf{C} := \{X_1, \ldots, X_n\}$. Algorithm 4.3 is implemented in pure CUDA and with the CUDA back end of HPXCL. Both implementations are performing asynchronous data transfers and are synchronized with the kernel launches. Thus, the performance implications of the abstractions are addressed. To avoid measuring the initialization, the benchmarks were run 1000 iterations and the mean value was used to compare both implementations with increasing elements in the node cloud $\mathbf{C}$. Figure 4.8a shows the mean execution time for the first benchmark for 1000 iterations on one compute node of the CRAY XK7. For the benchmark the implementation within the abstraction layer of HPXCL outperform the native CUDA implementation. For increasing elements n of the node cloud the difference of the execution time exceeds. Note, that both implementations use asynchronous data transfers, the HPXCL-CUDA abstraction layer additionally uses the futurization concept of HPX. This concept exposes a light-weight mechanism for the synchronization of results which results in improved performance for this benchmark. This optimization could be applied as well to the native CUDA implementation and the resulting

Algorithm 4.3: 3-Point Stencil Benchmark

Init X with random values;
CopyToDevice(X);
Apply stencil s on X;
CopyToHost(R);
Check result R;

code would look very similar to what is implemented in the abstraction layer of HPXCL. The second benchmark (Algorithm 4.4) emphasizes the asynchronous data

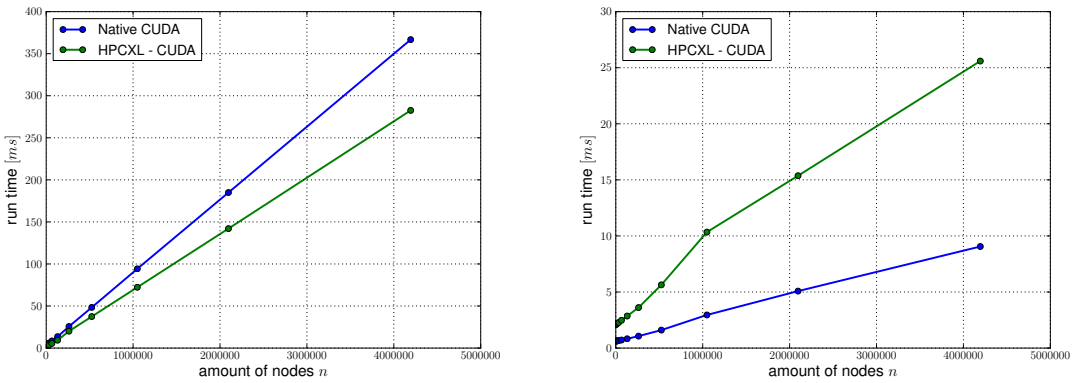

(a) Execution time of Algorithm 4.3 with a increasing size n of elements.

(b) Execution time of Algorithm 4.4 with a increasing size n of elements.

Figure 4.8.: Execution time for the Algorithm 4.3 and Algorithm 4.4 with a increasing size n of elements for pure CUDA and HPXCL.

transfer and the efficiency of overlapping between communication and computation. Therefore, a kernel $k(X_i) := \sqrt{\sin^2(X_i) + \cos^2(X_i)}$ is applied to the node cloud $\mathbf{C}$. For the efficiency of computation and data transfer the node cloud is divided in partitions and the copying of partitions and the execution of kernel, depending on the partition, is done asynchronously. This concept[1] is ported to HPXCL-CUDA by synchronizing the data transfer with the launching of the depending kernel based of HPX's `hpx::future` objects to build the parallel execution graph. The execution graph is built within the abstraction layer of HPXCL and the user is not required to handle the CUDA streams as in the native implementation. This abstraction improves the

[1] `https://devblogs.nvidia.com/parallelforall/how-overlap-data-transfers-cuda-cc/`

Algorithm 4.4: Multiple Partitions Benchmark

Init X with random values ;
for $i = 0$ *;* $i <$ *partition ;* $++i$ **do**
  CopyToHost(X_i);
end
for $i = 0$ *;* $i <$ *partition ;* $++i$ **do**
  Apply kernel k to partition X_i;
end
for $i = 0$ *;* $i <$ *partition ;* $++i$ **do**
  CopyToDevice(R_i);
end

programmability and the integration of asynchronous tasks in the work flow on the CPU. Figure 4.8b shows the execution time for the multiple partitions benchmark and run time overhead for the HPXCL-CUDA implementation is clearly visible. The implementation of HPXCL-CUDA relies on callbacks that are attached to CUDA streams for synchronizing with the futurization concept of HPX. For the benefit that the synchronization of local and remote GPUs is provided, a server-side synchronization of the `hpx::future` objects has to be implemented for gaining programmability in heterogeneous computing environments. The server-side synchronization of the futurization needs to be optimized to reduce the overhead of the abstraction layer.

On the one hand, with the abstraction, CUDA is tightly integrated into the HPX general purpose parallel run time system. Thus, local and remote GPU devices are seamlessly integrated into a fully heterogeneous application in a unified fashion. The combination of GPGPU with CPUs is more convenient for the programmer, because the synchronization of dependencies is hidden in the API of HPX and only the CUDA kernels need to be provided.

On the other hand, the sustainable development of scientific HPC codes is addressed. The API of the CUDA SDK is hidden by the abstraction layer of HPXCL and future concepts of the programming kernels are the only changes a programmer has to make at the code. Changes in the API are provided by updating the library.

Two possible future directions of the HPXCL library with respect to peridynamics are outlined in the following. First, the native CUDA implementation delivers performance issues for simulations with velocity conditions or boundary conditions. Where, the branch divergence issue of Compute Unified Device Architecture is

observed. Here PeriHPX, the generic implementation of the bond-based peridynamic using the EMU nodal discretization could be combined with the FNSG library (Section 4.1). By this, the neighbor search is outsourced to the GPU and is concurrent to the update of the forces or the positions on the CPU. Another benefit for the quasi-static formulation of bond-based peridynamics [Bre14] are the efficient matrix-vector operations for solving large matrix systems on GPUs.

Second, the coupling of the often computational expensive non-local methods with FEM or PUM could be done seamless with HPX and HPXCL. Here, in the area where cracks emerge or crack path bifurcates, the more accurate but also computational more expensive non-local method is executed on the GPU. The computational cheaper method outside the area of interest is executed on the CPU with HPX. Thus, a seamless asynchronous integration of both methods and the utilization of the full cluster capabilities of modern heterogeneous architectures is achieved.

4.3. Extraction of fragments and waves after impact damage

Analyzing simulation results and their verification against experimental data is essential for the development and interpretation of simulation models. In Section 5.1 the Prototype Microelastic Brittle model and the Discrete Prototype Microelastic Material where validated against the Edge-On impact experiment. Here, the extraction of the wave front out of the node-based data after the impact of the projectile was quite challenging. Therefore, two approaches for a quantitative comparison with a more “global” view are presented for the validation against experimental data.

The first analysis technique is an extended connected component algorithm for the extraction of fragment size and the corresponding histograms. The distribution of the fragment size with respect to the mass or velocity at the center of mass can be obtained by real-world experiments [Vog+03; SH05]. The second technique focuses on the visualization of stress after an impact. The node-based data is re-sampled and rendered with a standard volume technique to highlight the interference pattern after the reflection of the wave at the boundary. For a quantitative study with a simple geometry the EOI experiment [WSR89] and for a complex geometry the Stanford bunny (Subsection 4.3.2) can be applied. These new visualization approaches give new insights for the quantitative comparison of fragmentation.

Thus, understanding of wave propagation becomes more intuitive. For more details about the visualization techniques see [Die+ed]. Both of these techniques are available as Paraview Plugins.

4.3.1. Fragments and histograms

The identification of fragments after an impact, like a stone impacting the front window of a car, is important for the validation of node-based methods. Here the size of the fragments is an important estimation of the medical harm to the occupants. The relevant quantities, such as the size, mass or velocity of each fragment obtained by experiments is still difficult to compare with node-based simulations. A distribution for the number of fragments with respect to the mass is provided by the experiment in [SH05]. Here, a tungsten-alloy projectile perforates a steel armor plate with a velocity of $1020\,\mathrm{m\,s^{-1}}$. This data of the experiment is used as a benchmark for the smoothed particle hydrodynamics (SPH) model in [ZJH11] and for a Lagrangian approach in [R+07]. The fragmentation of a cylindrical steel tube with a gas gun impact with the impact velocity of $1920\,\mathrm{m\,s^{-1}}$, is another experiment covered in literature [Vog+03]. This experimental data was used as a benchmark for SPH [Owe05]. All of these benchmarks show that fragmentation obtained by the simulations is qualitatively reasonable, but the quantitative modeling of the material needs some improvement.

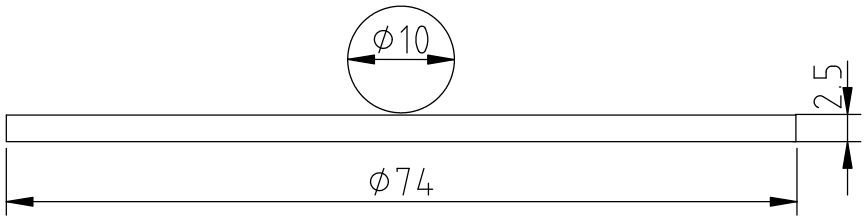

Figure 4.9.: Blueprint of the thin plate and the spherical projectile.

Figure 4.9 shows the simulation setup which was used to demonstrate the extraction of fragments. The plate is modeled with a material density ϱ of $2200\,\mathrm{kg\,m^{-3}}$, a bulk modulus K of $14.9\,\mathrm{GPa}$, and a shear modulus G of $8.9\,\mathrm{GPa}$. The spherical projectile is modeled as steel with a material density ϱ of $7700\,\mathrm{kg\,m^{-3}}$, a bulk modulus K of $160\,\mathrm{GPa}$, and a shear modulus G of $78.3\,\mathrm{GPa}$. It hits the target with a velocity of $200\,\mathrm{m\,s^{-1}}$. For the simulation with Peridigm [Par+12], the elastic material model combined with the critical stretch damage model was used. With a critical stretch

$s_c = 0.0025$, and for the interaction of the sphere and the plate a contact model with a spring constant of 1×10^{12}.

The first row in Figure 4.10 shows a common visualization of node-based simulations. Here the spheres are placed at the center of the actual position $x(t, X_i)$ of nodes over the time t. These spheres are colorized with the scalar damage $d(t, X_i)$ (2.38). Blue indicates that there is no damage and red indicates that all bonds inside the interaction zone $B_\delta(X_i)$ are broken. The damage develops radially from the center of the plate and starts to bifurcate twice before hitting the boundary of the plate. There are plenty of "free" particles in the center of the plate, which have no neighbors inside the interaction zone anymore. These particles foreclose the identification of the shape of the fragments and the crack paths. The Algorithm 1 (Connected Components) [Die+ed] is applied for extracting the fragments and provides an alternative visualization to highlight the crack branches in more detail. In the second column of Figure 4.10, the extracted fragments are colored by their label. This exposes the shape of the fragments noticeably and the crack pattern can be clearly observed (Figure 4.10j). Additionally, attributes like the mass or the velocity at the center of mass of the fragments are of interest for the comparison with experimental data.

The histograms of the fragment's size obtained by the algorithm are shown in Figure 4.11. The algorithm needs to be extended to estimate the mass of the fragment via the material density $\varrho(X_i)$ of the nodes and the volume $\mathbf{V}_i$. With this additional attribute, the histograms could be compared with the experimental data in [SH05; Vog+03]. Furthermore, the crack patterns look slightly different depending on the initial positions X of the nodes [HS14]. Here, the histograms could be compared with respect to the initial placement of the particles for the sensitivity of the mass or velocity at the center of the mass.

For the benchmark against the experiments,like mentioned above, the computational effort of the algorithm needs to be reduced for two reasons. First, the geometry of the projectile and the specimen in the experiments are more complex and the amount of nodes increases. Second, due to slow convergence of node-based methods the run time is no longer negligible.

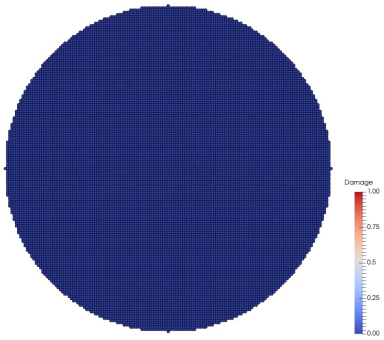

(a) $t = 0$ s

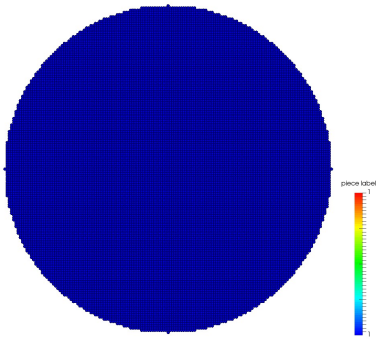

(b) $t = 0$ s

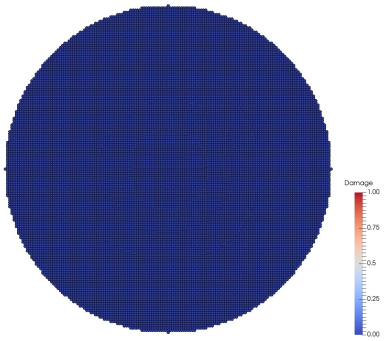

(c) $t = 6.38 \times 10^{-7}$ s

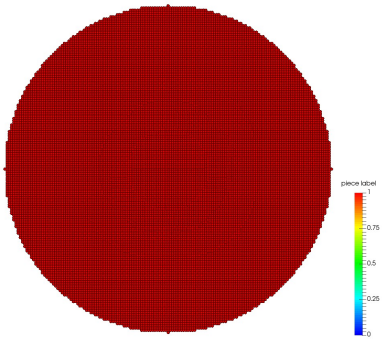

(d) $t = 6.38 \times 10^{-7}$ s

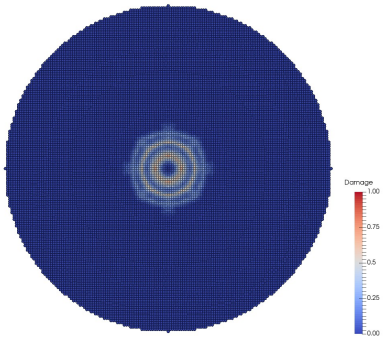

(e) $t = 1.27 \times 10^{-7}$ s

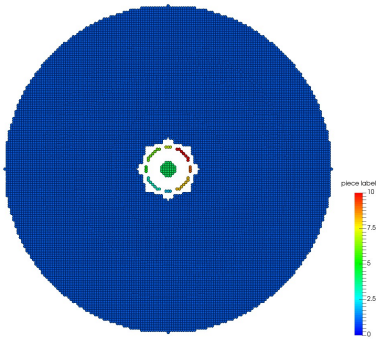

(f) $t = 1.27 \times 10^{-7}$ s

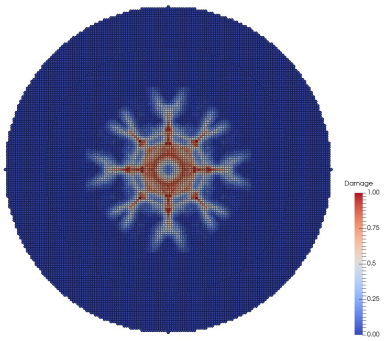

(g) $t = 1.91 \times 10^{-7}$ s

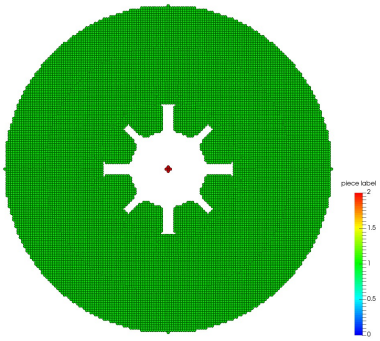

(h) $t = 1.91 \times 10^{-7}$ s

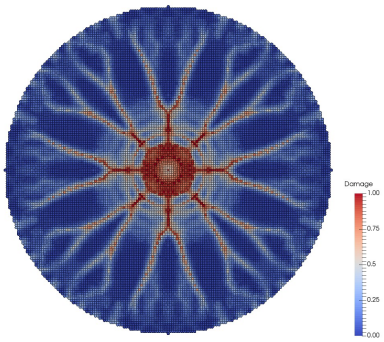

(i) $t = 2.55 \times 10^{-7}$ s

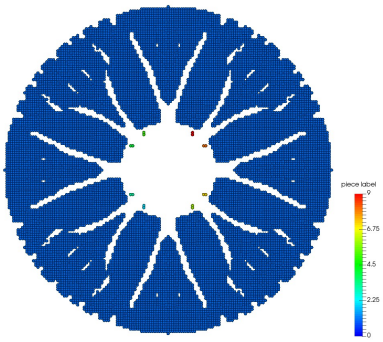

(j) $t = 2.55 \times 10^{-7}$ s

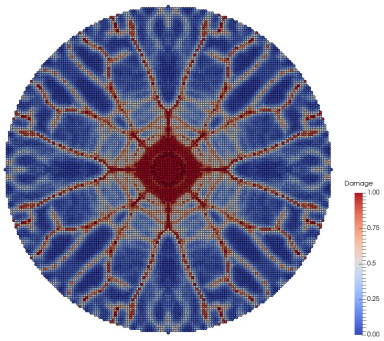

(k) $t = 3.18 \times 10^{-7}$ s

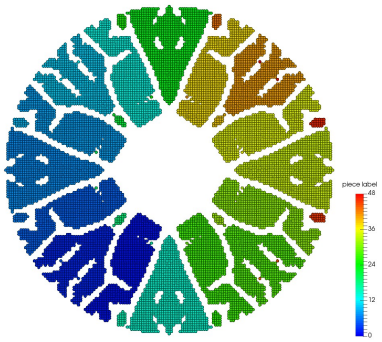

(l) $t = 3.18 \times 10^{-7}$ s

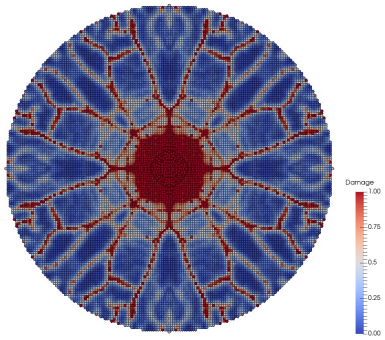

(m) $t = 3.82 \times 10^{-7}$ s

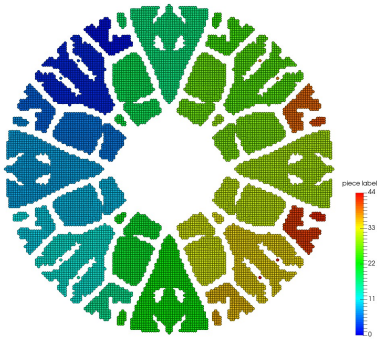

(n) $t = 3.82 \times 10^{-7}$ s

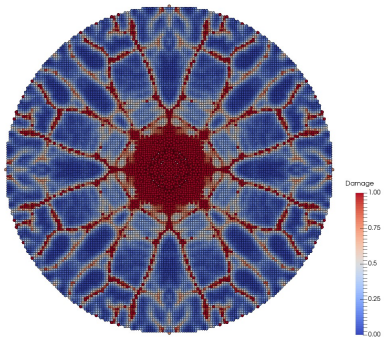

(o) $t = 4.45 \times 10^{-7}$ s

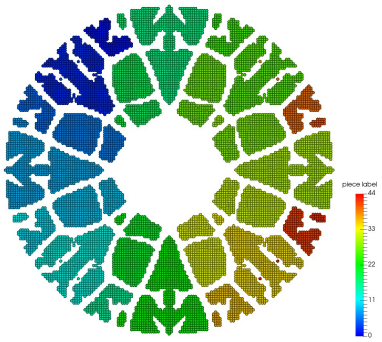

(p) $t = 4.45 \times 10^{-7}$ s

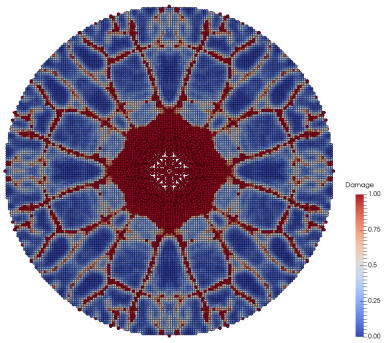

(q) $t = 8.27 \times 10^{-7}$ s

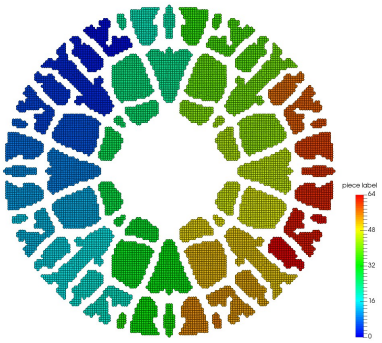

(r) $t = 8.27 \times 10^{-7}$ s

Figure 4.10.: Impact of a spherical projectile on a thin plate with a velocity of $200\,\mathrm{m\,s^{-1}}$. The nine figures on the left-hand side (above and below) show the visualization of the particles as spheres colorized with their damage $d(t, X)$ (2.38). The right-hand side shows the particles colorized according to the extracted fragments.

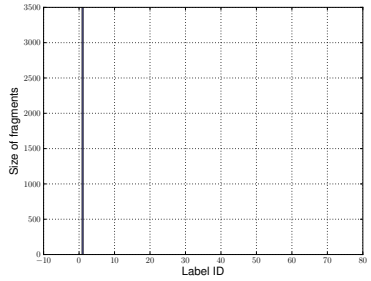

(a) $t = 6.38 \times 10^{-7}$ s

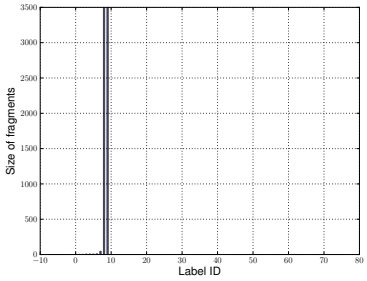

(b) $t = 1.27 \times 10^{-7}$ s

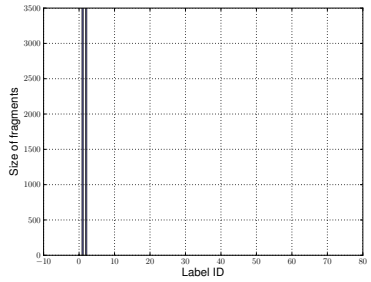

(c) $t = 1.91 \times 10^{-7}$ s

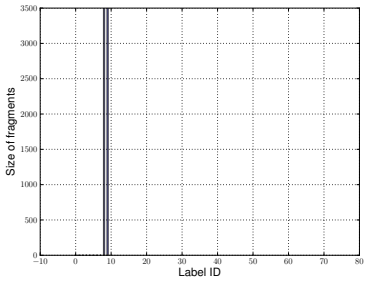

(d) $t = 2.55 \times 10^{-7}$ s

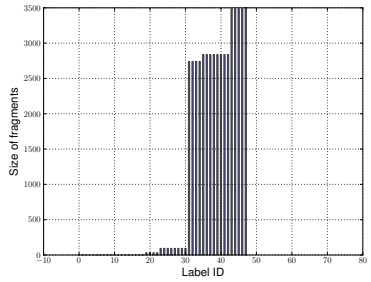

(e) $t = 3.18 \times 10^{-7}$ s

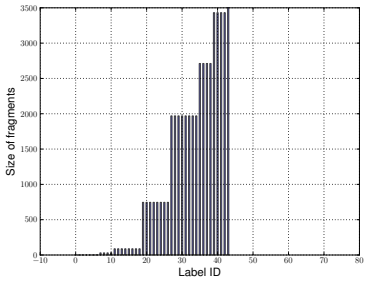

(f) $t = 3.82 \times 10^{-7}$ s

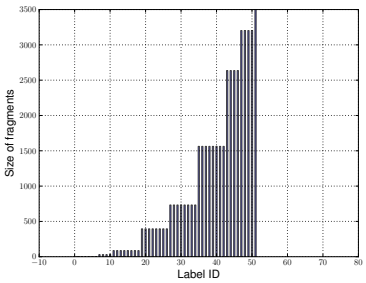

(g) $t = 4.45 \times 10^{-7}$ s

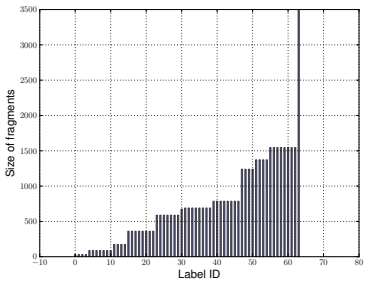

(h) $t = 8.27 \times 10^{-7}$ s

Figure 4.11.: Distribution of the fragments with respect to the amount of particles per fragment.

4.3.2. Wave propagation and impact damage

Understanding the wave propagation after impact damage is important to analyze how the damage front propagates through the specimen and reflects at the boundary of the geometry. In Subsection 5.1, the wave and damage front was simulated for the Edge-On impact (EOI) experiment. One challenge of the comparison of the speed of these fronts was the extraction of the fronts via the velocity $v(t, X_i)$ of node sets at time t. With this visualization technique, the local properties of each node are resampled and the resulting scalar field is visualized with a standard volume rendering technique. Thus, the propagation and the inference of the wave is visualized in a more "global" view. Figure 4.12a shows the Stanford bunny, a data set of the Stanford 3D scanning repository[2], scanned from a ceramic figurine of a rabbit. For the visualization of the propagation of the wave through the material in

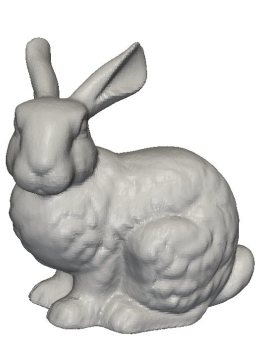

(a) The reconstructed surfaces of the Stanford bunny.

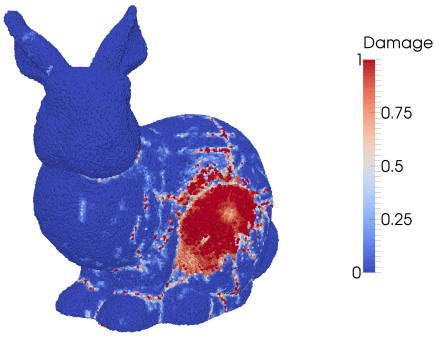

(b) Visualization of the impact damage per particle of the Stanford bunny.

Figure 4.12.: Figure (a) shows the extracted surfaces of the Stanford bunny as a complex geometry for the simulation and analysis, and Figure (b) shows the impact damage where the spheres at the actual positions $x(t, X_i)$ are colorized by the damage $d(t, X_i)$.

this complex geometry, (Figure 4.12b) the scalar value $d(t, X_i)$ is not sufficient. The reconstructed surfaces of the Stanford bunny are scattered with $1\,787\,245$ nodes and the material is modeled with a material density ϱ of $3369\,\mathrm{kg\,m^{-3}}$, a bulk modulus K of $210 \times 10^9\,\mathrm{Pa}$ and a critical stress intensity factor K_{Ic} of $2 \times 10^6\,\mathrm{Pa}\sqrt{\mathrm{m}}$.

[2] http://graphics.stanford.edu/data/3Dscanrep/

Figure 4.13 shows the development of the wave after the impact through the bunny visualized as a volume instead of nodes. With the visualization of the spectral norm of the virial stress (5.7) a more “global” view of the propagation, interference and reflection of the wave after the impact is provided. Figures 4.13b–4.13g show the development of the wave after the impact through the bunny. Figure 4.13h visualize the reflection of the wave at the back of the bunny at time $t = 20\times10^{-8}$ (colored in red). After the reflection, the interference of the wave is shown in Figures 4.13i–4.13x. The artifacts at the lugs and the occiput of the bunny are clearly evident in Figure 4.13l and Figure 4.13u.

(a) $t = 0$ s **(b)** $t = 1{\times}10^{-8}$ s **(c)** $t = 5{\times}10^{-8}$ s

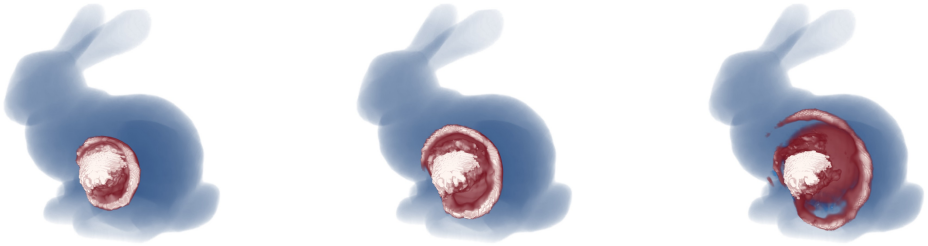

(d) $t = 7{\times}10^{-8}$ s **(e)** $t = 9{\times}10^{-8}$ s **(f)** $t = 12{\times}10^{-8}$ s

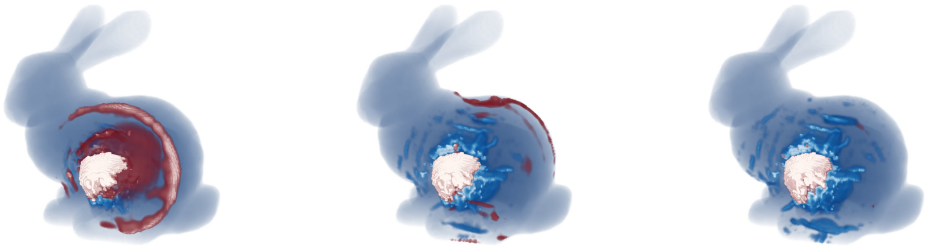

(g) $t = 14{\times}10^{-8}$ s **(h)** $t = 20{\times}10^{-8}$ s **(i)** $t = 25{\times}10^{-8}$ s

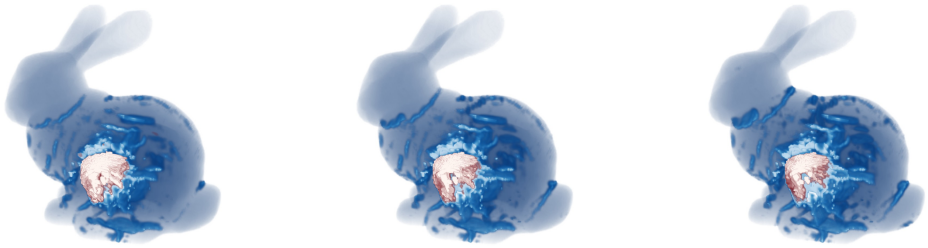

(j) $t = 30{\times}10^{-8}$ s **(k)** $t = 35{\times}10^{-8}$ s **(l)** $t = 40{\times}10^{-8}$ s

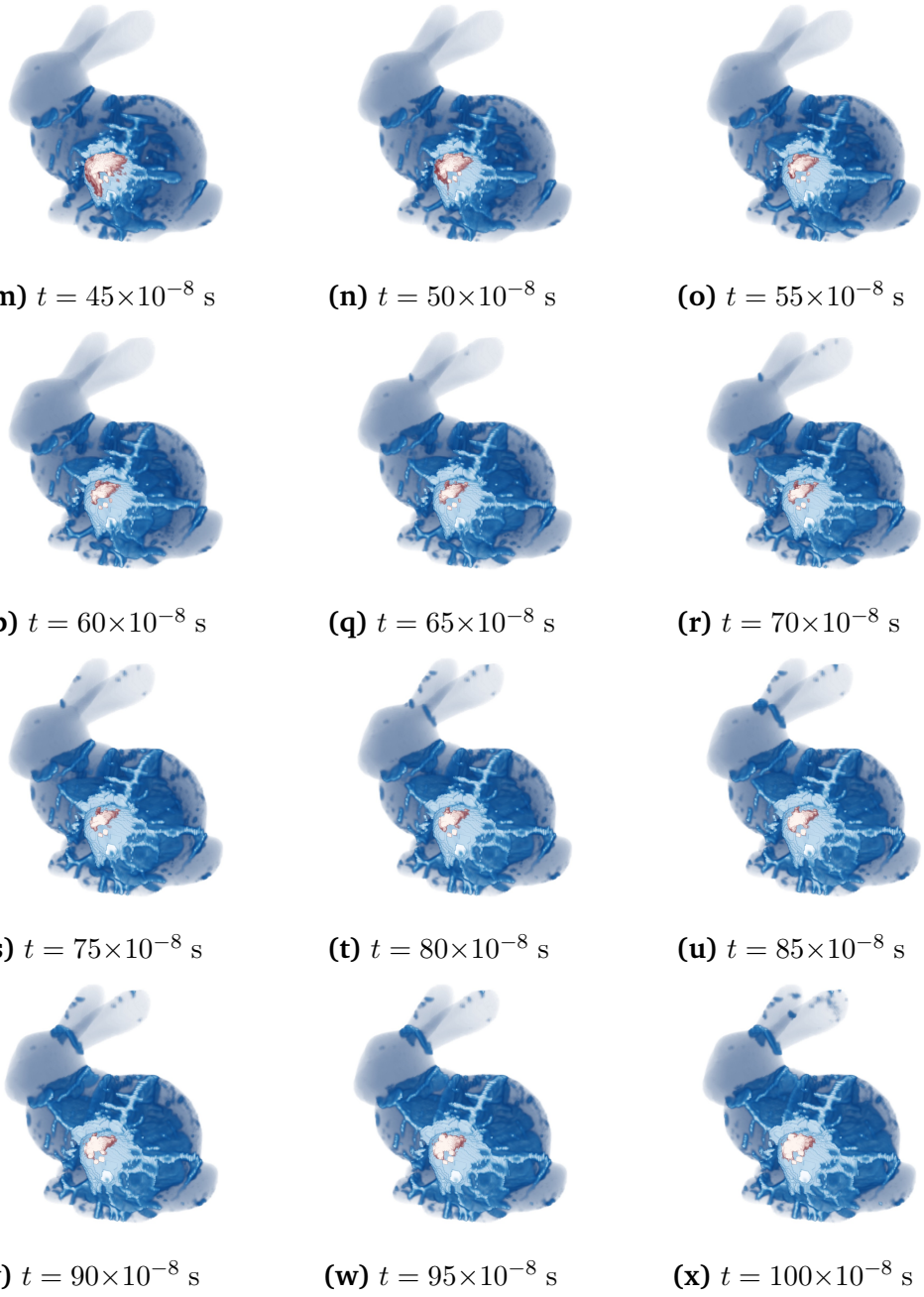

(m) $t = 45{\times}10^{-8}$ s **(n)** $t = 50{\times}10^{-8}$ s **(o)** $t = 55{\times}10^{-8}$ s

(p) $t = 60{\times}10^{-8}$ s **(q)** $t = 65{\times}10^{-8}$ s **(r)** $t = 70{\times}10^{-8}$ s

(s) $t = 75{\times}10^{-8}$ s **(t)** $t = 80{\times}10^{-8}$ s **(u)** $t = 85{\times}10^{-8}$ s

(v) $t = 90{\times}10^{-8}$ s **(w)** $t = 95{\times}10^{-8}$ s **(x)** $t = 100{\times}10^{-8}$ s

Figure 4.13.: Visualization of the stress in the Stanford bunny (1 787 245 nodes) with a spherical projectile with an impact velocity of $100\,\mathrm{m\,s^{-1}}$ and a time step size of 10^{-8} s.

5.Numerical results

In this chapter three experiments for the initiation and growth of cracks are considered. In Section 5.1 the Edge-On impact experiment is used for the propagation of waves after impact damage. Here, the obtained velocity at the wave front in the simulation is compared with the one measured in the experiment. The bond-based peridynamic PMB material model and bond-based peridynamic DPMB model are employed as constitutive laws for modeling Aluminiumoxynitrid (ALON). The critical traction for mode *I* crack opening is studied for the bond-based peridynamic DPMB material model for a wide range of materials in Section 5.2. Here, the obtained value in the simulation is compared to the prescribed value for the critical traction by Linear Elastic Fracture Mechanics (LEFM). The calibration for connecting the parameters of a specific bond-based peridynamic softening model material model to the shear modulus and fracture toughness of LEFM via theoretical relations was done in Section 2.3.2. In Section 5.3 this calibrated model is applied to verify the linearity of the displacement field and the Poisson effect for small deformations. In the simulation the Poisson ratio and the Young modulus are computed equivalent to physical experiments. Next to the consistency of the material properties to the material properties of polymethyl methacrylate (PMMA), the same time-dependent behavior of the Poisson ratio and the Young modulus is compared to the measured behavior of a real physical tensile test.

5.1. Comparison with Edge-On impact experiment

Nowadays, ceramics are of great relevance for industrial sector, they are a essential ingredient of batteries in electric/hybrid cars or modern airplanes. One import feature of this kind of battery type is the safety of its ceramic core during a crash. Here, the precise approximation of the evolution of the damage after an impact and the wave propagation is highly important to ensure the safe operation of the device. The Edge-On impact (EOI) [WSR89; Sch39; Str04], developed in the 1980s for the visualization of wave propagation and impact damage, is a classical benchmark for impact damage in brittle materials.

The EOI is used for different macroscopic ceramic material models as a verification against experimental data. One example is the Kayenta material model [BFS09], a generalized plasticity model for ceramic materials. Employing it on a traditional mesh-based discretization on a Lagrangian hexahedral mesh delivers an average of $83\ \%$ of damage velocity of the experimental results. Furthermore, the damage and the resulting cracks align in a preferential horizontal and vertical fashion [Lea+13]. Thus, a common issue of mesh-alignment is observed. With traditional particle-based methods, e.g. smoothed particle hydrodynamics (SPH), however, damage and cracks are smeared out [RHT10; Ben92].

EOI is used as a benchmark for the bond-based PMB model (Section 2.3.1) and the bond-based DPMB model (Section 3.3). Note, that the DPMB model is the PMB model extended with a surface correction. The advantages of the bond-based peridynamic and the applied discretization are:

- The EMU nodal discretization (EMU ND) can be classified as a total-Lagrangian collocation method with nodal integration (Section 3). Similar, to SPH, no mesh is involved and the alignment of cracks and fractures is not restricted to it.
- The force function f of peridynamics allows for non-smooth kernel functions and the EMU ND provides the modeling of local damage.

Resulting, it is promising that the bond-based peridynamic and the EMU ND overcome the above mentioned deficiencies of the other macroscopic ceramic models.

5.1.1. Model problem

For the comparison with experimental data the Edge-On impact (EOI) experiment, developed by the Ernst-Mach-Institute for the visualization of dynamic fractures in brittle materials using a high-speed camera technique [Str04], is applied. Here the experiment with a glass plate was done in the late 1930s [Sch39]. In the 1980s it was reused to visualize impact damage and wave propagation in ceramic materials [WSR89]. This experiment was applied in [BFS09; Lea+13] for the Kayenta model and in [RHT10] for SPH with a Lagrangian hydro-code approach as a benchmark. Thus, the same experiment is used for the bond-based peridynamic as a benchmark for wave propagation and impact damage.

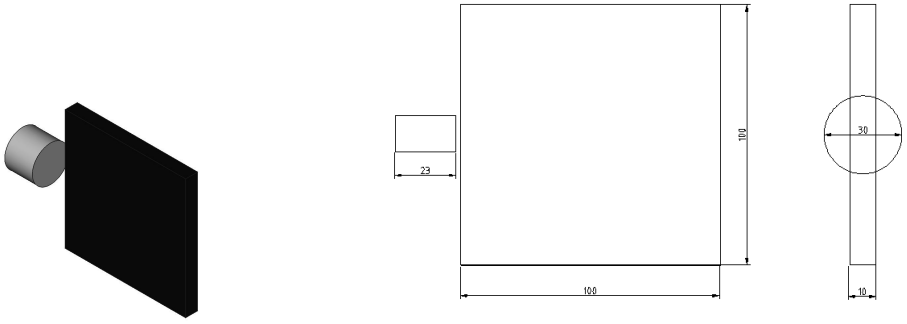

(a) Experimental assembly of the plate and the cylindrical projectile.

(b) Blueprint of the plate and the cylindrical projectile.

Figure 5.1.: Figure (a) shows the assembly of the experiment with the steel projectile of and the Aluminiumoxynitrid (ALON) specimen. The measurements of the experimental assembly is shown in Figure (b) for a projectile with a diameter of $30\,\mathrm{mm}$ and a length of $23\,\mathrm{mm}$ and a specimen ($100\,\mathrm{mm}\times\ 100\,\mathrm{mm}\times\ 31\,\mathrm{mm}$). The contact force $b(t, X_i)$ between the projectile and the plate was 3.8×10^5 N.

Figure 5.1 shortly summarizes the simulation setup. More details for the visualization of the wave propagation are described in [Sch39; Str04]. The experiments described in [Str+05; Str+06] are used to compare the obtained wave fronts of the simulations with the experimental data shown in Table 5.1.

Wave	Velocity $[\mathrm{m\,s^{-1}}]$
Wave front	9367
Coherent damage/fracture front	8381

Table 5.1.: Experimental measured wave velocities for Aluminiumoxynitrid (ALON) at the nominal impact velocity of $380\,\mathrm{m\,s^{-1}}$ at time $8.6\,\mu\mathrm{s}$ [Str+05; Str+06]. Common material properties for ALON are for the bulk modulus $K\ = 210\,\mathrm{GPa}$ and for the critical stress intensity factor $K_{\mathrm{Ic}}\ =\ 2\,\mathrm{MPa}\sqrt{\mathrm{m}}$.

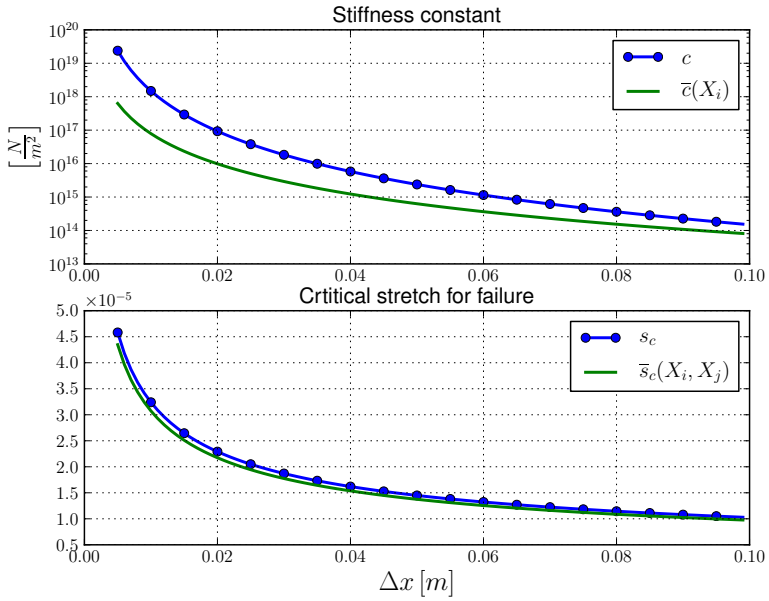

Figure 5.2.: Comparison of the stiffness constant and the critical stretch for bond failure for PMB and DPMB (Table 3.1). The material parameter for ALON are for the bulk modulus $K = 210\,\mathrm{GPa}$ and for the critical stress intensity factor $K_{\mathrm{Ic}} = 2\,\mathrm{MPa}\sqrt{\mathrm{m}}$. The nodal spacing Δx is in the range of $[5 \times 10^{-3}, 1 \times 10^{-1}]\,\mathrm{m}$.

5.1.2. Results

The obtained speed at the extracted wave front in the simulations is compared to wave speeds (see Table 5.1) observed in experiments [Str+05; Str+06]. In this numerical study the bond-based PMB material model and the bond-based DPMB material are employed. Note, that the DPMB material model (Section 3.3) is the PMB material model with a surface correction for the skin effect (Figure 3.2b). Figure 5.2 shows the stiffness constants and the critical stretches for bond failure for both materials (Table 3.1). The material points are assembled on the nodes of a regular grid and the surrounding volume of X_i is chosen as $\mathbf{V}_i = \Delta x^3$. The material parameter for ALON are for the bulk modulus $K = 210\,\mathrm{GPa}$ and for the critical stress intensity factor $K_{\mathrm{Ic}} = 2\,\mathrm{MPa}\sqrt{\mathrm{m}}$. The nodal spacing Δx is in the range of $[5 \times 10^{-3}, 1 \times 10^{-1}]\,\mathrm{m}$. The stiffness constants c and $\overline{c}(X_i)$ differ by two orders of the magnitude. The critical stretch for bond failure s_c and $\overline{s}_c(X_i, X_j)$ differ marginally.

Figures 5.3a-5.3b show the results for two different limit cases in Figure 3.4 for the obtained wave speed in the simulations. Each figure shows the speed at the wave front and the speed at coherent damage front for a nominal velocity of $380\ \mathrm{m\,s^{-1}}$ at time $8.7\ \mu\mathrm{s}$. Figure 5.3a shows the resulting wave speed for the continuum local case $u_{\delta,0}$. Note, that this case here is simplified and the decreasing of the nodal spacing Δx is coupled to the decreasing of the horizon $\delta = 3\Delta x$. A more complex study for the ratio $\delta/\Delta x$ is done in Section 5.2 for the Mode *I* crack opening. In Figure 5.3a the propagation of the wave speed starts with decreasing nodal spacing Δx. The obtained wave speed is for one nodal spacing in the range of the speed at the wave front and the coherent damage front of the experiments. For the next nodal spacing, the obtained speed in the simulation overshoots the experimental values. For the DPMB model, no front wave could be obtained for the fitted parameter $\delta = 3\Delta x$ [SA05; Sil11].

Note, that a single GPU-based implementation of the bond-based peridynamic [Die12] is used on a Nvidia Tesla M2090 with 6 GB. Therefore, the simulations are restricted to the memory limitations of the GPU, especially for the DPMB model, where each material point has its own stiffness constant $\overline{c}(X_i)$.

Figure 5.3b shows the discrete local case $u_{0,\Delta x}$, where the nodal spacing $\Delta x = \text{const}$ and the horizon $\delta \to 0$ decreases to zero. The range of the horizon δ is chosen as $[2\Delta x, 2\sqrt{(2)}\Delta x, 3\Delta x, 4\Delta x]$. For $\delta = \Delta x$ the interaction zone was too small and the crack and fracture where aligned to the structure of the initial grid. Thus, the same limitations as in the mesh-based approach can be seen. For the PMB model, the best result is obtained by adjusting the horizon so that the peridynamic result produces the same dispersion curve as the measured one for the respective material. Additionally, in [BH12] it was suggested that a smaller horizon δ delivers better results, since the wave dispersion due to the size of the non-locality is reduced as the horizon decreases.

For the DPMB a study for a good ratio for the horizon and the nodal spacing δ/dx is done in Section 5.2 for the Mode *I* crack opening. Here, the obtained critical traction (5.7) in the simulation is compared with the prediction of the Linear Elastic Fracture Mechanics.

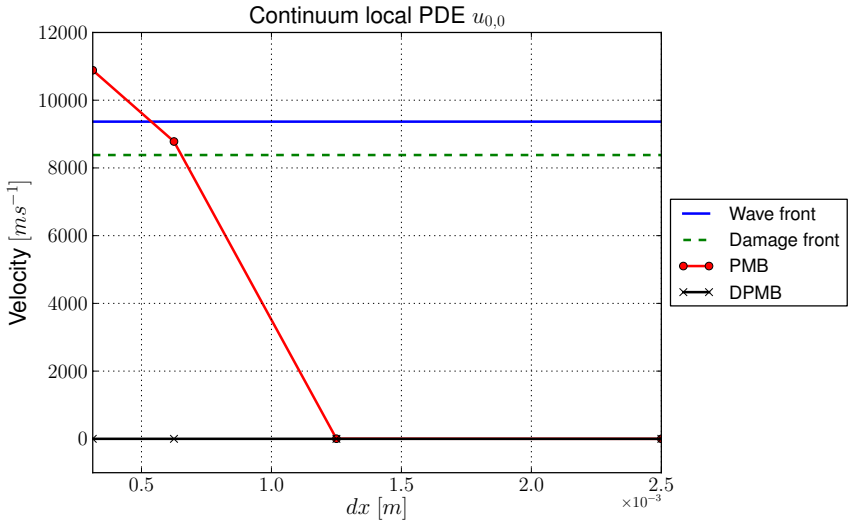

(a) Continuum local $u_{\delta,0}$ case, where $\Delta x \to 0$ and $\delta = 3\Delta x$ decrease to zero.

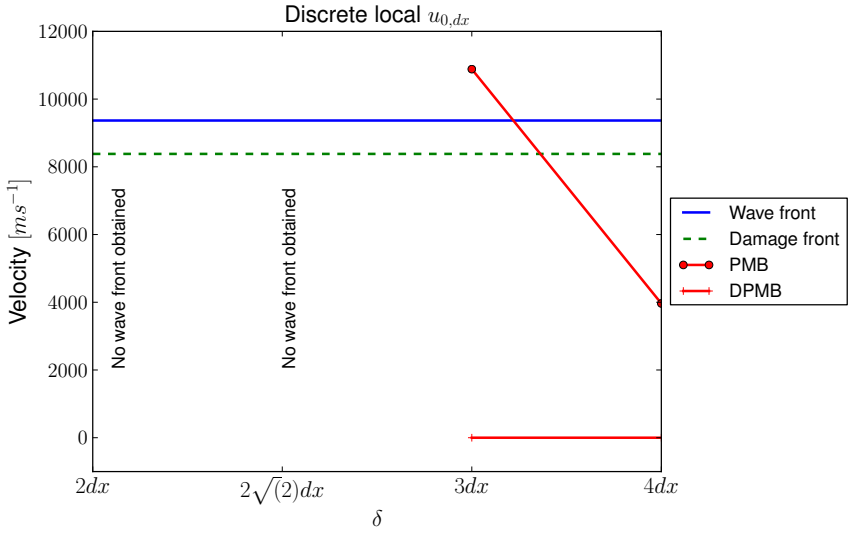

(b) Discrete local $u_{0,\Delta x}$ case, where Δx was fixed and δ goes to zero.

Figure 5.3.: The obtained wave speed for two different limit cases of Figure 3.4 for the Edge-On impact experiment.

5.1.3. Summary

The deficiencies of the other macroscopic ceramic materials are not seen in the simulation results of the bond-based PMB material model and the EMU ND discretization. In [BFS09] an alignment of the damage and cracks was observed in a horizontal and vertical fashion. In the simulations this alignment was not observed for the bond-based PMB material model. Depending on the choice for the horizon δ, due to the non-smooth kernel functions, the cracks and fractures develop locally. They do not smear out, like other particle methods, repetitive SPH [RHT10].

The obtained speed at the extracted wave front is compared with the coherent damage front and wave front in [Str+05; Str+06] as a reference. For the PMB material model the suggested horizon $\delta = 3\Delta x$ [SA05] results in applicable results for the wave propagation. The extracted speed at the wave front is in the range of the coherent damage front and the wave front (Table 5.1). Here, the horizon is adjusted for this model, such that it reproduces the same dispersion curve as those measured for a specific material [Sil11]. For the discrete limit $u_{0,\Delta x}$ in Figure 3.4 a smaller horizon δ gets better results, since wave dispersion due to the size of the non-locality is reduced as the horizon decreases [BH12].

For the DPMB material model, the extraction of the wave front in the node-based data was quite challenging. The extraction using velocity and the damage (2.38) as quantities, worked well for the PMB model, but not for the DPMB model. Here, more sophisticated techniques for the extraction of the wave front should be applied. One possible approach is the visualization technique described in Section 4.3.2. The results in [GHM14] considered an idealized material with a bulk modulus $K = 1\ \mathrm{Pa}$ and a material density $\varrho = 1\ \mathrm{kg\,m^{-3}}$. Here, the wave propagation was initiated by an initial displacement with a Gaussian distribution. In addition, the comparison with experimental data includes errors in the experimental setup and the measurements.

For both material models the choice of the horizon δ or respectively the ratio $\delta/\Delta x$ affects the result of the simulations. In Section 5.2 the comparison of the critical traction obtained by the Linear Elastic Fracture Mechanics for the DPMB model is done. The focus here is on the sensitivity of the parameters (e.g. horizon δ, nodal spacing Δx) to the quantity of interest, the critical traction shortly before the crack starts to grow.

5.2. Critical traction for Mode *I* crack opening

The EOI experiment was studied in Section 5.1 for the comparison with experimental data. Here, one can see that the resulting wave speed for the PMB material model is feasible for the continuum local $u_{\delta,0}$ case. For this material model the horizon parameter δ is fitted. Tian and Du [TD13] claimed that the horizon δ should shrink slower than the nodal spacing Δx for convergence to the continuum local PDE $u_{0,0}$ case.

In this Section the DPMB material model is studied for the critical traction in Mode *I* crack opening. The critical traction $\vec{\sigma}_a$ (5.7) obtained in the simulations is compared to the critical traction $\vec{\sigma}_c$ (5.6) prescribed by Linear Elastic Fracture Mechanics (LEFM). Before the comparison of critical traction, the constitutive law is validated against the Young's modulus from classical theory for a homogeneous deformation in Section 5.2.3. Different ratios of $\delta/\Delta x$ are employed to compare the critical traction. Here, the goal is to emphasize what a good choice of the ratio $\delta/\Delta x$ could be.

Therefore, a wide range of materials from polymethyl methacrylate (PMMA) up to titanium alloy (Table 5.2) was studied. Note, that the predicted critical traction by LEFM is for quasi-static loading. Thus, the time step size is very small and goes up to 3×10^6 time steps in the largest setting. For addressing this wide range of material runs, a surrogate model is applied to reduce the computational expensive PD simulations.

5.2.1. Surrogate model

As a surrogate model, the concept of sparse grids was used, which is briefly introduced here. For more details on the theory see [BG04; Pfl12] and for more details regarding efficient implementation see [Pfl10]. The studied system can be driven by a model $\mathcal{M} = (\mathbf{z}, h)$ that depends on a finite number of parameters, after the normalization to the unit cube, $\mathbf{z} = (z_1, z_2, \ldots, z_d) \in [0,1]^d$. These parameters are mapped to a real-valued quantity of interest with a unknown multivariate response function $h(\mathbf{z}) \in \mathbb{R}$. For this application, the model $\mathcal{M}$ can be thought of as a bond-based peridynamics simulation with $\mathbf{z}$ as the parameter (Δx, δ, etc.) with respect to a quantity of interest (e.g. maximum strain) using a simulation that describes h.

Suppose a search for a surrogate model $g(\mathbf{z})$ of the multivariate function $h(\mathbf{z}) \in \mathbb{R}$ on the unit hypercube $[0,1]^d$. The surrogate model g is restricted to to the space of piece wise d-linear functions $\mathcal{V}_\ell$ with ℓ being the maximum discretization level in each dimension. An index set, with the multi-indices $\vec{l} = \{l_1, \ldots, l_d\}$ and $\vec{i} = \{i_1, \ldots, i_d\}$ can be defined as

$$\mathcal{I}_{\vec{l}} := \{(\vec{l}, \vec{i}) : 1 \leq i_k < 2^{l_k}, i_k \text{ odd}, k = 1, \ldots, d\}\,, \tag{5.1}$$

with the size $N := |\mathcal{I}_{\vec{l}}|$. The grid points are nested, i.e., the grid points at level l_k are equal to the even-indexed grid points at level $l_k + 1$, $1 \leq k \leq d$. The general one-dimensional reference hat function $\varphi(z) := \max(1 - |z|, 0)$ is used to obtain the one-dimensional hierarchical hat functions $\varphi_{l,i}(z)$. These are centered at the grid points by scaling and translation according to level l and index i as $\varphi_{l,i}(z) := \varphi(2^l z - i)$. Higher-dimensional basis functions can be obtained via a tensor-product approach,

$$\varphi_{\vec{l},\vec{i}}(\mathbf{z}) := \prod_{k=1}^{d} \varphi_{l_k,i_k}(z_k)\,. \tag{5.2}$$

The level-index vectors $\vec{l}, \vec{i}$ define a unique set of hierarchical increment spaces $\mathcal{W}_{\vec{l}} := \text{span}(\{\varphi_{\vec{l},\vec{i}} : (\vec{l}, \vec{i}) \in \mathcal{I}_{\vec{l}}\})$. The space $\mathcal{V}_\ell$ of piece wise d-linear functions on a full grid, with equidistant grid spacing in each dimension, is obtained by a direct sum of all increment spaces up to level ℓ in each dimension,

$$\mathcal{V}_\ell = \bigoplus_{|\vec{l}|_\infty \leq \ell} \mathcal{W}_{\vec{l}}, \tag{5.3}$$

where $|\vec{l}|_\infty = \max_{1 \leq k \leq d} l_k$.

The hierarchical basis allows to consider just those increment spaces that contribute most to our approximation are chosen. For sufficiently smooth functions h, it is possible to choose the optimal set of sub spaces a priori [BG04]. In this context, sufficiently smooth means that h is a function of the mixed Sobolev space H^2_{mix}, where the mixed weak derivatives up to order 2 are bounded. The sparse grid space is obtained by selecting

$$\mathcal{V}_\ell^{(1)} := \bigoplus_{|\vec{l}|_1 \leq \ell + d - 1} \mathcal{W}_{\vec{l}} \tag{5.4}$$

and is optimal for such functions in an L_2 sense [BG04], where $|\vec{l}|_1 = \sum_{k=1}^{d} l_k$. This end up for $g_{\mathcal{I}_{\vec{l}}}$ as a linear combination of $\varphi_{\vec{l},\vec{i}}$,

$$g_{\mathcal{I}_{\vec{l}}}(\mathbf{z}) = \sum_{(\vec{l},\vec{i})\in|\vec{l}|_1\leq\ell+d-1} \alpha_{\vec{l},\vec{i}}\varphi_{\vec{l},\vec{i}}(\mathbf{z}) \in \mathcal{V}_\ell^{(1)}\,, \tag{5.5}$$

with $\alpha_{\vec{l},\vec{i}}$ as the hierarchical coefficients.

The number of grid points is reduced significantly from $\mathcal{O}((2^\ell)^d)$ for a full grid to $\mathcal{O}(2^\ell \ell^{d-1})$. This is one of the main properties of the sparse grid approach. Therefore, sparse grids overcome the curse of dimensionality to some extent. The interpolation accuracy is of order $\mathcal{O}((2^{-\ell})^2 \ell^{d-1})$, which is just slightly worse than the accuracy of a full grid $\mathcal{O}((2^{-\ell})^2)$.

5.2.2. Model Problem

The model problem considered here is Mode *I* fracture or crack opening under tensile stress. For the geometry shown in Figure 5.4 with a initial crack of length a the Linear Elastic Fracture Mechanics (LEFM) theory predicts the critical traction as

$$\vec{\sigma}_c(K_{\mathrm{Ic}}, L, a) := K_{\mathrm{Ic}} \frac{1}{\sqrt{\pi a}} \left(1.12 - 0.23\frac{a}{L} + 10.6\frac{a^2}{L^2} - 21.7\frac{a^3}{L^3} + 30.4\frac{a^4}{L^4}\right)^{-1}. \tag{5.6}$$

The critical traction depends on the critical stress intensity factor K_{Ic} as the only material parameter from classical elasticity [CY98] and L and a are given by the geometry. The traction $\vec{\sigma}$ is defined as the force per area $\mathrm{N\,m^{-2}}$ and $\vec{\sigma}_c$ is the critical traction, which occurs shortly before the initial crack starts to propagate. The specimen for this study is a 2D specimen with a height and width of $(1\mathrm{m} \times 2\mathrm{m})$ and an initial crack length $a = 124\mathrm{mm}$. The initial crack is the line with the points $(0, 0.5)\mathrm{m}$ and $(0.125, 0.5)\mathrm{m}$. All bonds crossing this plane are set as initially broken. At the top (Top) and the bottom (Bottom) of the rectangular prism a thin layer of the height $1 \times 10^{-3}\mathrm{m}$ is defined as the boundary, see Figure 5.4. The initial velocity of these boundaries is set to the scaled bulk sound speed $c_o(K, \varrho) := 10^{-5}\sqrt{K/\varrho}$, which depends on the bulk modulus K and the material density ϱ. For an adaptive choice of the time step size, the Courant–Friedrichs–Lewy (CFL) condition $dt_{\mathrm{CFL}} := \Delta x/2c_0$

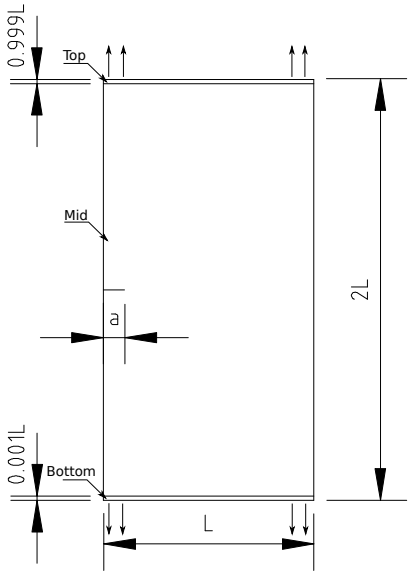

Figure 5.4.: Blueprint of the simulation setup. The parameter L of the geometry is $1\ \mathrm{m}$ and $a := {}^{L}/_{8}$. The initial velocity is applied at the geometric region Top and Bottom. The traction applied to these two regions is measured at the region Mid of the specimen.

is applied. For the discrete peridynamic model, the virial stress $\vec{\sigma}_a : [0,T] \times \mathbb{R}^3 \to \mathbb{R}$, an atomistic measure of mechanical stress [TPM09], is given by

$$\vec{\sigma}_a(t,X_i) := \\ -\frac{1}{2\|\mathbf{V}_i\|} \sum_{X_j \in B_\delta(X_i)} \Big((x(t,X_i) + x(t,X_j)) \overline{f}(t, x(t,X_j) - x(t,X_i), X_j - X_i) \Big) . \tag{5.7}$$

For measuring the traction applied to the specimen, the atomistic stress (5.7) is averaged over the geometric region Mid (Figure 5.4). Here, all nodes in the reference configuration Ω_0 contribute to A_{Mid}. The critical traction given as the maximum value of the yy-component of this stress tensor (coinciding with the loading direction) is observed during the simulation by

$$\vec{\sigma}^n_{a_c} := \max_{t \le T} \left\{ \frac{1}{\|A_{\text{Mid}}\|} \sum_{X_i \in A_{\text{Mid}}} \vec{\sigma}_a(t,X_i)_{yy} \right\} . \tag{5.8}$$

Parameter	Min	Max	Unit	Description
K	3.1×10^9	116×10^9	Pa	Bulk modulus
K_{Ic}	1×10^6	66×10^6	$\mathrm{Pa}\sqrt{\mathrm{m}}$	Critical stress intensity factor
ϱ	1180	2630	$\mathrm{kg\,m^{-1}}$	Material density
$n = 1/\Delta x$	10	250	–	Number of nodes
$\vec{\sigma}_c$	1.3×10^7	8.6×10^8	Pa	LEFM critical traction (5.6)
e	1.1×10^{-4}	2.8×10^{-1}	–	LEFM strain
$\overline{s}_c$	3.3×10^{-4}	1.6×10^{-3}	–	Critical stretch (3.15)

Table 5.2.: Range of the parameters that define the parametric input space for the simulation.

Note, that for the computation of the critical traction, the same spatial algorithm of LAMMPS is applied and its accuracy is discussed in [Sel14]. Table 5.2 shows the range of the parameters that define the parametric input space used in the simulations. The largest simulation, involving 125000 nodes, was completed within 24 hours on two cluster nodes with 16 CPU each. The simulations were computed with an extended version of LAMMPS [Pli95] with the improved prototype micro brittle material model. Thus, this model $\mathcal{M}_{\text{Peridynamics}} = (\mathbf{z}, h)$ with $\mathbf{z} := (K, K_{\mathrm{Ic}}, \rho, n)$ and $h := \vec{\sigma}^n_{a_c}$ is studied.

5.2.3. Verification of the constitutive law

The Young's modulus for a homogeneous deformation was obtained for the verification of the constitutive law. According to the classical theory the elastic modulus of a material is given by $\mathrm{E}_{\text{clas}} = \left[1/(1+\nu^2)\right]_{\nu=1/3} = 9/10$. For obtaining the Young's modulus for the DPMB material model the geometry (Figure 5.4) without the initial crack is applied. For the simulation, an extended version of LAMMPS and its spatial integration scheme is used. Figure 3.2a emphasizes a common issue of this integration scheme: the volume of the nodes close to the cut-off radius δ is partly outside and inside of the integration domain. The spatial integration within LAMMPS uses the full volume of these nodes and does not apply any partial volume correction. For the ratio between the horizon δ and the nodal spacing Δx, different values of either 3, 4 or 5 are suggested [HB10; HB11; HHB12; Sil11; SA05]. These suggested ratios

are applied to obtain the Young's modulus for the DPMB model with a fixed nodal spacing and the spatial integration algorithm of LAMMPS.

$\delta/\Delta x$	$\mathrm{E}_{\mathrm{LAMMPS}}$	$\mathrm{E}_{\mathrm{PA\text{-}HHB}}$	$\lvert\mathrm{E}_{\mathrm{clas}} - \mathrm{E}_{\mathrm{LAMMPS}}\rvert$	$\lvert\mathrm{E}_{\mathrm{clas}} - \mathrm{E}_{\mathrm{PA\text{-}HHB}}\rvert$
2.0	0.959	0.903	0.059	0.003
2.5	0.852	0.869	0.048	0.031
3.0	0.84	0.833	0.056	0.067
3.5	0.86	0.863	0.034	0.037
4.0	0.84	0.825	0.06	0.075

Table 5.3.: Young's modulus obtained by the slope of the stress-strain curve for a homogeneous deformation with different ratios for $\delta/\Delta x$ for a fixed nodal spacing Δx and compared to the analytic Young's modulus $\mathrm{E}_{\mathrm{clas}} = 0.9$ from elasticity theory.

Table 5.3 shows the Young's modulus $\mathrm{E}_{\mathrm{LAMMPS}}$ obtained by simulations for different ratios of $\delta/\Delta x$ in the second column and the error with respect to the classical theory $\mathrm{E}_{\mathrm{Class}}$ in the fourth column. For the spatial integration of LAMMPS without any volume correction the error with respect to the classical theory is ≈ 0.05. Next, the focus is on more accurate quadrature rules [Sel14], e.g. the PA-HHB partial volume correction [HHB10]. In the third column is the Young's modulus obtained with the PA-HHB volume correction. With this volume correction, the error is small for a ratio of 2 and between 0.03 and 0.07 for larger values. The improved quadrature rule does not directly relate significantly to the accuracy of the Young's modulus for a homogeneous deformation. A reason for the similar accuracies of the quadrature rule in Table 5.3 is the surface effect, which affects the computation of the Young's modulus using the stress-strain curve approach. An alternative approach where the Young's modulus is computed by displacements is presented in [Sar+16].

In addition, the relative error of the critical traction with respect to the LEFM theory was studied for different ratios of $\delta/\Delta x$. It can be considered as a robustness study in order to access the sensitivity of the model error with respect to these two discretization parameters. This study considers PMMA and titanium alloy, the two corner cases of the range of materials that should be addressed here. These materials define the lower and upper limit for the bulk modulus K and the critical stress intensity factor K_{Ic}, which define two important parameters. The two-dimensional parameter space that consists of the nodal spacing $\Delta x \in [1/250, 1/10]$ and the horizon $\delta \in [1, 5]$ in units of Δx. The domain is sampled uniformly with respect to δ and

logarithmically with respect to Δx. These simulations were run for both materials, such that the longest computation time for one simulation was 7 days on a 32 core machine. For each material 250 simulations were done. The results of the robustness study is presented in Figure 5.5. On the left-hand side of the figure the

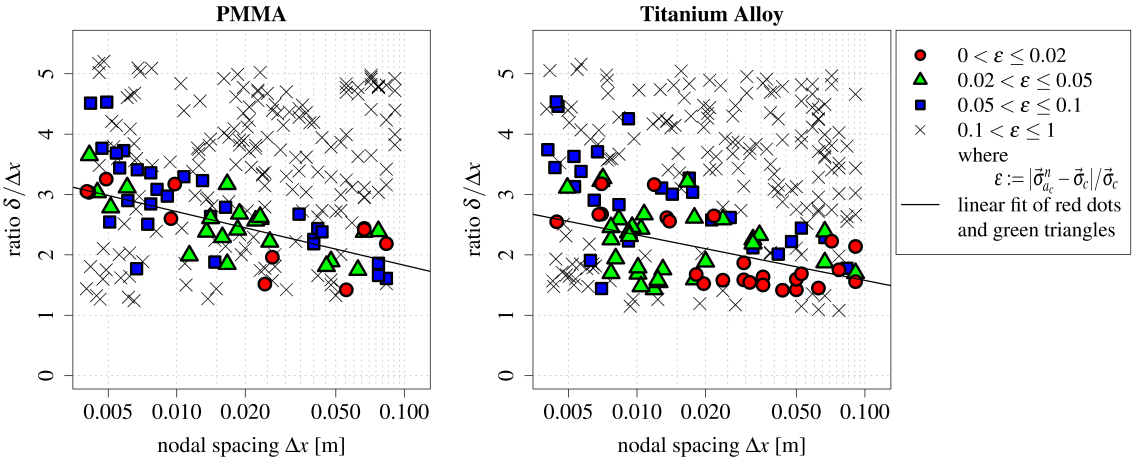

Figure 5.5.: Figures show an extended robustness study for the nodal spacing Δx and the ratio $\delta/\Delta x$. The left plot shows the simulation results for PMMA, the right plot for titanium alloy. The different markers are related to the relative error ϵ of the simulation results obtained for the critical traction for the corresponding parameter combination with respect to the reference solution obtained via LEFM theory.

result for PMMA is addressed. The markers in the plot represent the selected labels. These are categorized in four categories: the red dots represent simulations with a relative error ϵ of the critical traction $\vec{\sigma}^n_{a_c}$ with respect to the analytical solution $\vec{\sigma}_c$ smaller than $2\ \%$, the green triangles represent simulations with an error between $2\ \%$ and $5\ \%$, the blue squares between $5\ \%$ and $10\ \%$, and finally, the crosses are the remaining ones. If an error of $5\ \%$ is acceptable, then the plots suggest that there is an acceptable δ for each Δx to achieve $\epsilon < 5\ \%$. Moreover, the plot for PMMA implies non-continuous behavior. As an example, the error exhibits large gradients at $\Delta x \approx 0.0025$ between the two red dots at a ratio of approximately 1.5 and 2. This makes it difficult to find a regular pattern to obtain a simple optimal functional relation between Δx and δ.

A tendency of the ratio can be identified by a linear fit of the acceptable results (red dots and green triangles). Here, the ratio $\delta/\Delta x$ increases with shrinking Δx, which means to see convergence, δ should shrink slower than Δx. This result is

supported by [TD13]. Additionally, the ratio of 3 is a good choice for practical purposes for small Δx, as suggested by [SA05]. A possible reason for this behavior is that the ratio for the PMB model was adjusted such that the measured dispersion curve of the material is reproduced, see [Sil11]. Increasing δ does not improve the result since the error increases and does not seem to get smaller at least within the simulated parameter range. Similar behavior is observed for titanium alloy and even slightly smaller ratios of $\delta/\Delta x$ lead to acceptable results for small nodal spacing Δx. The following conclusion can be drawn: choosing a proper horizon is not trivial and requires an expensive optimization for each nodal spacing and material, which is not feasible for a large range of materials. A ratio of $\delta/\Delta x = 3$ seems to be a reasonably good choice for both PMMA and for titanium alloy and small Δx.

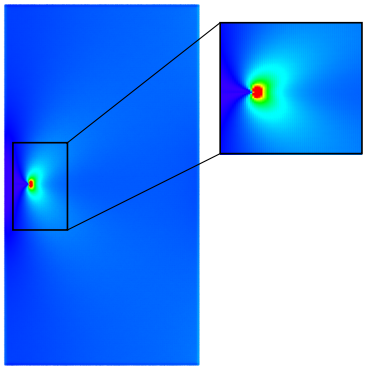

(a) Visualization of the stress per node shortly before the crack propagation occurs.

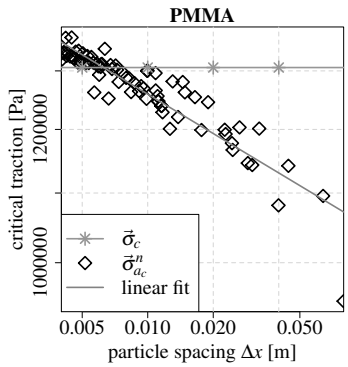

(b) Scatter plot (log-log scale) of the failure stress for randomly chosen nodal spacings Δx for the material parameters of PMMA ($K = 3.1 \times 10^9$, $K_{\text{Ic}} = 1 \times 10^6$, $\rho = 1160$).

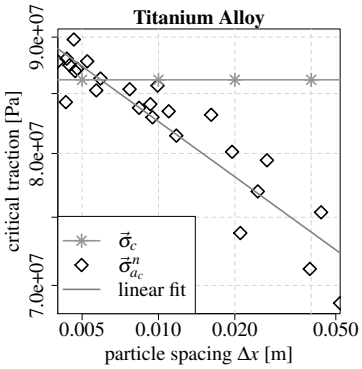

(c) Scatter plot (log-log scale) of the failure stress for randomly chosen nodal spacings Δx for the material parameters of titanium alloy ($K = 116 \times 10^9$, $K_{\text{Ic}} = 66 \times 10^6$, $\rho = 2630$).

Figure 5.6.: Figure (a) shows the stress per node shortly before the crack propagation occurs for the simulation parameters $\varrho = 1180\,\mathrm{kg\,m^{-1}}$, $n = 250$, $K_{\text{Ic}} = 2.7 \times 10^6$ Pa, and $K = 6.3 \times 10^{10}$ Pa. Figures (b) and (c) show scatter plots for PMMA and titanium alloy for fixed δ, ρ, K_{Ic} and K. One can see that the analytic result was not achieved with shrinking nodal spacing and keeping the horizon δ fixed. Nevertheless, for small Δx the results are robust since they lie within a small interval around the analytic value.

Before a wide range of materials is studied in Section 5.2.4 the focus on the robustness with respect to the nodal spacing $\Delta x \to 0$ for PMMA and titanium alloy is addressed. Therefore, the parameter space is cut at $\delta/\Delta x = 3$ and the resulting parameter space is sampled again logarithmically. In Figure 5.6b and Figure 5.6c, the starred line is the predicted traction from the LEFM theory (5.6) and should be obtained in the simulation in the limit for $\Delta x \to 0$. The gray diamonds in the plots are the values of the simulations runs for different values of Δx. The obtained values in Figure 5.6b overshoot the predicted value for very small $\Delta x \approx 0.005$. The relative error for $\Delta x < 0.01$ lies within a range of $\epsilon \leq 5\%$. Figure 5.6c shows the same behavior for titanium alloy and it also differs up to $5\ \%$ from the predicted value for $\Delta x < 0.01$. Therefore, the peridynamic model does not entirely reflect the continuum model, but these results quantify the expected error intervals.

5.2.4. Results

This section shows the simulation results for the wide range of materials, which are specified by the parameter ranges (Table 5.2). The DPMB material model is robust within these parameter ranges and reproduce the critical traction from elasticity theory up to small error. To validate the model problem (Section 5.2.2), the stress per node, shortly before the crack propagation occurs is visualized. Figure 5.6a shows, for example, the simulation for parameters $\varrho = 1180\,\mathrm{kg\,m^{-1}}$, $n = 250$, $K_{\mathrm{Ic}} = 2.7 \times 10^6\ \mathrm{Pa}$ and $K = 6.3 \times 10^10\ \mathrm{Pa}$. For all permutations of the minimal and maximal values of the parametric input space (Table 5.2), the symmetry was checked and the maximal value of the traction shortly before the crack propagation occurs was tracked.

Figure 5.7a shows a scatter plot with 4×4 tiles for the 4-dimensional sparse grid surrogate $g_{\mathcal{I}_{\bar{l}}}$. The tiles are referred to line and column indices, with $(0, 0)$ as the lower-left corner, $(0, 3)$ the top-left corner, and so on. The scatter plot contains two kinds of lower-dimensional representations of the 4-dimensional function. In the lower triangle, projections on two dimensions each are shown; the corresponding parameters can be found on the axis of the scatter plot. The two-dimensional projections for all subplots (i, j) were obtained by integrating over all dimensions but i and j. For example, $(0, 0)$ is the projection onto the K-n plane, $\int_{K_{\mathrm{Ic}},\rho} g_{\mathcal{I}_{\bar{l}}}(K, K_{\mathrm{Ic}}, \rho, n)$. The upper triangle contains the histograms of the function values for the corresponding projections. Thus, $(2, 3)$ is the histogram of $(0, 1)$. For Fig. 5.7a and Fig. 5.7b the

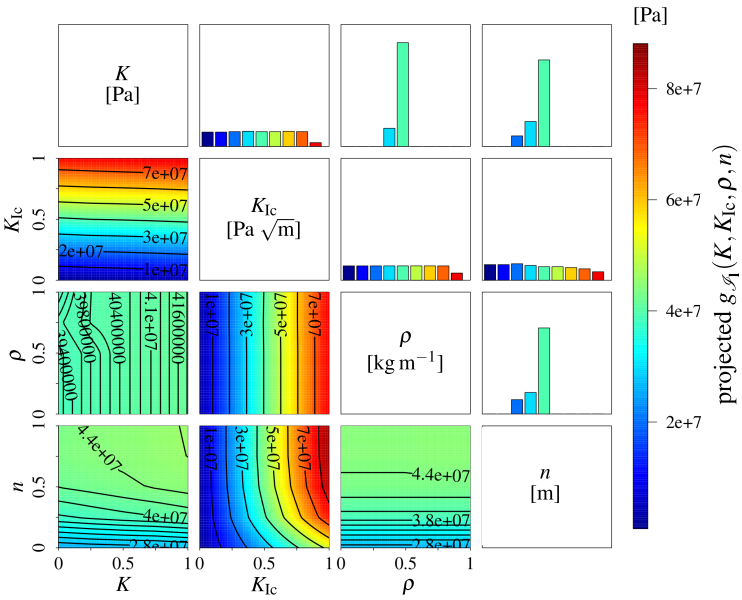

(a) Scatter plot matrix for the sparse grid surrogate $g_{\mathcal{I}_{\vec{l}}}$. Each tile in the lower triangle of the plot contains a projection of $g_{\mathcal{I}_{\vec{l}}}$ on two out of the four dimensions. The upper triangle additionally shows histograms of the corresponding function values drawn in the lower triangle.

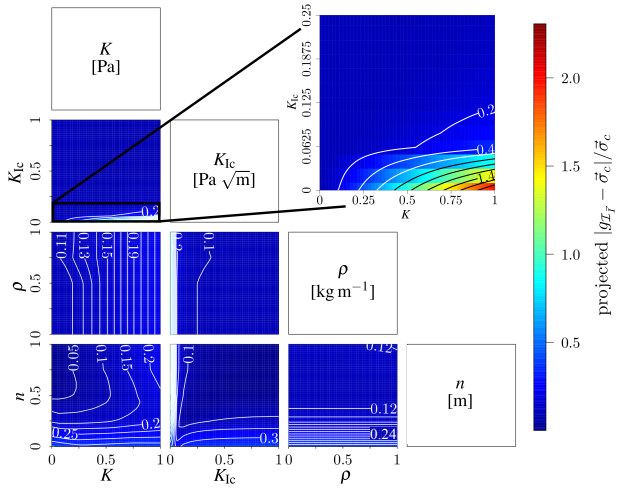

(b) Scatter plot matrix of the relative error for the sparse grid surrogate $g_{\mathcal{I}_{\vec{l}}}$ with respect to the reference function $\vec{\sigma}_c$. The enlarged plot shows that the error is largest for small values of K_{Ic}.

Figure 5.7.: Scatter plot matrix for the sparse grid surrogate $g_{\mathcal{I}_{\vec{l}}}$ and the relative error for the sparse grid surrogate $g_{\mathcal{I}_{\vec{l}}}$ with respect to the reference function $\vec{\sigma}_c$.

sparse grid function is equidistantly sampled in each dimension and the sample can be seen as an approximation for the integrals.

The influence of the material density ϱ can be seen at the subplots $(0,1)$, $(1,1)$, and $(0,2)$. These are projections on the planes K-ρ, K_{Ic}-ρ and ρ-n. For parallel contour lines to the direction of ϱ are these values independent of ϱ. In the subplots $(1,1)$ and $(0,2)$, the contour lines are parallel to this direction, but not everywhere with respect to K in subplot $(0,1)$. To study this phenomenon further, K is fixed at 3.1×10^9 and the remaining 3D-space is searched for dependencies of $\vec{\sigma}_{a_c}^{n}$. For $n > 154$ and $13 \times 10^6 < K_{\text{IC}} < 51 \times 10^6$, a dependency on the material density ϱ exists. A major investigation is needed to study this behavior of the artificial materials, where no knowledge about their material properties exists.

The subplots $(0,0)$ and $(1,0)$ show the projections of the bulk modulus K and the critical stress intensity factor K_{Ic} for $n = {}^1/_{\Delta x}$. Taking vertical cuts of these subplots and following the corresponding contour lines shows the critical traction increases for small n and reaches a steady state for larger n. The same behavior can be seen for PMMA (Figure 5.6b) and titanium alloy (Figure 5.6c) on linear scales. This indicates that the observations for the lower-case and upper-case hold for the whole domain of the parameter range in Table 5.2.

Furthermore, the projections in Figure 5.7a nicely reflect properties of the LEFM theory in Equation (5.6): The projections depend linearly on K_{Ic} with respect to all other parameters, see the subplots $(0,2)$, $(1,1)$ and $(1,0)$. The corresponding histograms in $(1,3)$, $(3,2)$ and $(2,2)$ show exactly this behavior.

Figure 5.7b visualizes the relative error with respect to the prescribed critical strain $\vec{\sigma}_c$ of the LEFM theory. The projections in the lower triangle have been created as before, but now for the relative error $|g_{\mathcal{I}_{\vec{i}}} - \vec{\sigma}_c|/\vec{\sigma}_c$. For most material configurations, the projected (integrated over two dimensions) relative error is smaller than 0.5. Only for simulation parameters with values $K \geq 42.5 \times 10^9$ and $K_{\text{Ic}} \leq 6.99 \times 10^6$ does the relative error increase to 2. For a example, the projection $(0,2)$ is zoomed in and presented at the upper right corner of Fig. 5.7b. As a result materials with high densities, low values for the bulk modulus K and low values for the critical stress intensity factor K_{Ic} should be avoided in the parameter range. For the remaining parameters in the range, the DPMB material model with the EMU ND discretization delivers acceptable results.

5.2.5. Summary

The critical traction for Mode *I* crack opening was estimated with the DPMB bond-based PD model, which is a special case of the state-based LPS material model. The employment of sparse grids enables a study of an astonishingly large range of materials. The validity of this approach is compared with the values predicted by Linear Elastic Fracture Mechanics for quasi-static loading [CY98].

For the majority of materials, the limit $\vec{\sigma}^n_{a_c}$ exists and differs by $\approx 5\%$ from the prescribed value of the LEFM theory. For most materials, the critical traction obtained in the simulation $\vec{\sigma}^n_{a_c}(K_{\text{Ic}}) = \mathtt{C}K_{\text{Ic}}$ depends only on K_{Ic} for a constant $\mathtt{C}$. Additionally, it is independent of the material density which further confirms the soundness of this approach. In general the DPMB bond-based model is feasible for this task.

In the following reasons for the examined overshooting by 5% are given. First, model errors have to be addressed. The DPMB material model models linear elasticity with only one proportionality constant $\bar{c}$ instead of two constants as in classical elasticity theory [SA05].

Second, the applied EMU ND discretization introduces a discretization error. This error is influenced by the skin-effect and the spatial integration without any volume correction. Different surface correction methods are available [KM10; LH12a; MS07]. For the validation of the constitutive law, the Young's modulus for a homogeneous deformation with EMU ND discretization was obtained. The result is compared with the classical theory without a volume correction and the PA-HHB correction [HHB10]. The accuracy of the improved spatial integration and LAMMPS spatial integration is similar.

Third, the choice of the horizon δ heavily influences the results. The nodal spacing Δx has to shrink faster than the horizon δ to obtain convergence. In literature different ratios of $\delta/\Delta x$ are suggested for isotropic and anisotropic materials [HB10; HB11; HHB12]. For the PMB model a ratio of 3 seems to be sufficient [Sil11; SA05]. For the lower range PMMA and the upper case titan alloy, a good Δx can be found for each δ and vice versa if a small error is acceptable. Nevertheless, there is no regular pattern from which a simple functional relation between δ and Δx could be derived. Thus, the choice of a suitable horizon δ for a given nodal spacing Δx is challenging.

For an error of 5% the bond-based DPMB material model with the EMU ND discretization without any volume correction is very robust for the ratio of $\delta/\Delta x = 3$.

5.3. Verification of a bond-based softening model for small deformations

A specific bond-based peridynamic softening model was calibrated using theoretical relations to connect the model material parameter to the shear modulus and the fracture toughness from Linear Elastic Fracture Mechanics (LEFM), see Section 2.3.2. This calibrated softening model is discretized with the EMU nodal discretization (EMU ND) and numerical experiments identical to physical experiments for the identification of material properties are done. First, the linearity of the displacement field and the Poisson effect for small strains is studied in Section 5.3.2. Second, the time-dependent Poisson ratio with respect to linear loading is compared with the results from a tensile test in Section 5.3.3. For the consistency of Poisson ratio and the Young modulus the obtained values in the simulation should lie in the range of material properties of polymethyl methacrylate (PMMA). Furthermore, the time-dependent material behavior of a tensile test should be seen in the simulation for the Poisson ratio, see Figure 5.8 to reflect the material behavior of the real physical experiment.

5.3.1. Model Problem

In engineering a common way to obtain material parameters is a tensile test. Here, the specimen of the observed material is placed at a electromechanical testing machine, which applies a quasi-static load to the boundary of the specimen. In addition, the experiment is observed with a stereo-microscope. Digital image correlation (DIC) is used to extract properties like the displacement (See Figure A.1). These properties are used to compute the time-dependent Poisson ratio $\tilde{\nu}(t)$ and the Young modulus $\tilde{E}(t)$. Figure 5.8 displays the Poisson ratio, obtained by the experiment until the specimen was broken. At the beginning the ratio is negative, shortly goes up to ≈ 0.7, shrinks to $\approx 0,4$ and diverges around this value until the specimen breaks at $120\,\mathrm{s}$. After 40 seconds the ratio is in the common range for the Poisson ratio for PMMA (Table 5.4).

Material property	
Density ϱ	$1.11 \times 10^3 - 1.18 \times 10^3$ kg m^{-3}
Young modulus E	$1.6 - 3.3$ GPa
Bulk modulus K	$3.6 - 3.68$ GPa
Poisson Ratio ν	$0.389 - 0.413$
Fracture Toughness G	$1.81 - 2.18$ MPa$/\sqrt{\text{m}}$

Table 5.4.: Common material parameters for impact modified polymethyl methacrylate (PMMA) with a composition *(CH-C(CH3)COOCH3)n*

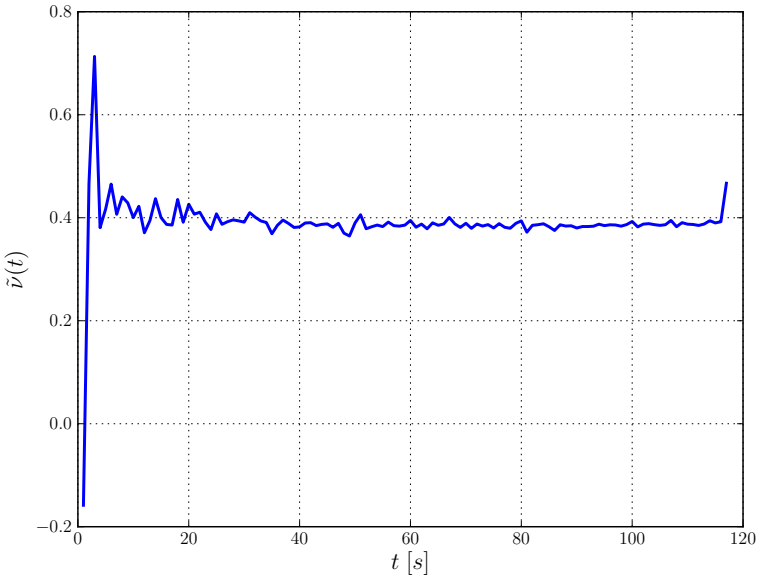

Figure 5.8.: Time-dependent Poisson ratio for PMMA obtained by a experiment and extracted via DIC.

The following questions are addressed to validate the energy equivalence applied in Section 2.3.2 to obtain the bond-based softening model peridynamic material parameters:

1. Is the time-dependent behavior of the Poisson ratio like in Figure 5.8 reproduced in the simulation?
2. Are the ranges of the Poisson ratio and the Young modulus as in Table 5.4 deduced in the simulation?

Simulation setup

For all simulations in this section a cubical domain $\Omega_0 = 0.21\,\mathrm{m} \times 0.21\,\mathrm{m} \times 0.21\,\mathrm{m}$ centered at $(1\,\mathrm{m}, 1\,\mathrm{m}, 1\,\mathrm{m})^T$, compare Figure 5.9, is considered. A external force at the left and right boundary (green-colored nodes), i.e. $b(t, X_i)_1 = \pm 40000\,\mathrm{N}$ is applied. For the estimation of the material properties in Section 5.3.3 the central node (blue-colored node) located at $X_i = (1\,\mathrm{m}, 1\,\mathrm{m}, 1\,\mathrm{m})^T$ and its interaction zone $B_\delta(X_i)$ is considered for the numerical results for small deformations. In Section 5.3.2 the linearity of the displacement field for the nodes inside the interaction zone is analyzed. Here, the linearity of the displacement field is checked in order to reproduce the elastic constants associated with PMMA. Second, the reproduction of the Poisson ratio and the Young modulus in Section 5.3.3 is considered. To obtain

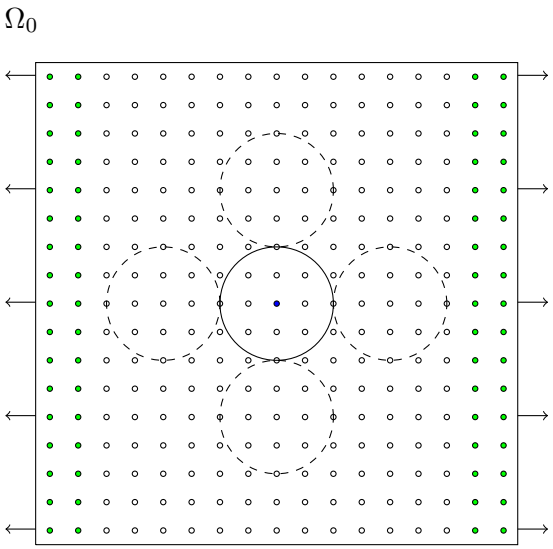

Figure 5.9.: Cross section in x-y-direction of the cube with the measurements $0.21\,\mathrm{m} \times 0.21\,\mathrm{m} \times 0.21\,\mathrm{m}$ centered at $(1\,\mathrm{m}, 1\,\mathrm{m}, 1\,\mathrm{m})^T$. The green colored nodes indicates where the external force $b(t, X_i)$ is applied.

the nodal spacing Δx of the nodes, the so-called m-convergence [BH11] is applied, such that the interaction zone $B_\delta(X_i)$ contains $2m + 1$ nodes in $[X_i - \delta, X_i + \delta]$ in each direction. To avoid effects from surface correction or reflection of waves in the numerical results, additional interaction zone (dashed ones) are located next to the interaction zone of interest as buffer zones. Two additional layers of nodes at the top and bottom in the y-direction are added with respect to symmetry. For the numerical experiments addressed in the next Section we choose $m = 4$, $\delta = 0.03\,\mathrm{m}$, and a time

step size $t = 1 \times 10^{-8}\,\mathrm{s}$. Note that here that there is a balance between the amount of particles inside the neighborhood $B_\delta(X_i)$ and interpretation of the displacement field. In addition, the focus here is on the validation of the applied discretization to the bond-based softening PD model. The convergence of this model is not addressed at this point. An overview related to this topic is provided in Section 3.2.

5.3.2. Linearity of the displacement

For this experiment the displacement of all nodes inside the interaction zone is considered. Therefore, some nodes inside the interaction zone are validated for linear displacement between the time steps for small strains. Due to symmetry, which was validated in the simulations, some nodes inside the interaction zone are not plotted here. In Figure 5.10 the selected nodes with these markers and colorization considered in this study are shown. The nodes were selected with respect to

$$\begin{aligned}
\bullet &\Leftrightarrow \{X_j \,|\, X_j \in B_\delta(X_i) \,\wedge\, X_{j_1} = 1 \,\wedge\, X_{j_2} = 1\} \\
\triangle &\Leftrightarrow \{X_j \,|\, X_j \in B_\delta(X_i) \,\wedge\, X_{j_1} < 1 \,\wedge\, X_{j_2} > 1\} \\
\triangleright &\Leftrightarrow \{X_j \,|\, X_j \in B_\delta(X_i) \,\wedge\, X_{j_1} > 1 \,\wedge\, X_{j_2} < 1\}\,.
\end{aligned} \tag{5.9}$$

All nodes $\bullet$ lie in the center of the interaction with respect to the x-y-plane. The other two types of marker are chosen with respect to the octants of a three-dimensional coordinate system. The eight octants inside the interaction zone are labeled using a sign convention. The nodes $\triangle$ are in octant $(-\,+\,+)$, the so-called top-back-right octant II and the nodes $\triangleright$ are in the octant $(+\,-\,+)$, the so-called top-front-left octant IV. From now on roman numbers of the octants are used for simplicity.

Following questions are addressed to validate the linearity of the considered specific softening model:

1. Is the displacement linear for the small bond stretches $\underline{s}$? The bond-based softening model and the energy equivalence with the classical theory (Section 2.3.2) is done under the assumption that the pair-wise bond force (2.56) is in the linear regime before the bond starts to "soften" (Figure 2.7b). Therefore, the displacement has to be linear.
2. Is there no displacement at the node at X_i and very small displacement at nodes close to it? This point is in the middle of the cube and the force

conditions at the first two layers of nodes and last two layers of nodes in x-direction are symmetric. Thus, because of the equilibrium in the middle of the cube no displacement should exist at node X_i.

3. Is the so-called Poisson effect, that when a material is compressed in one direction the two other directions expand perpendicular to the direction of compression (or vice versa), seen?

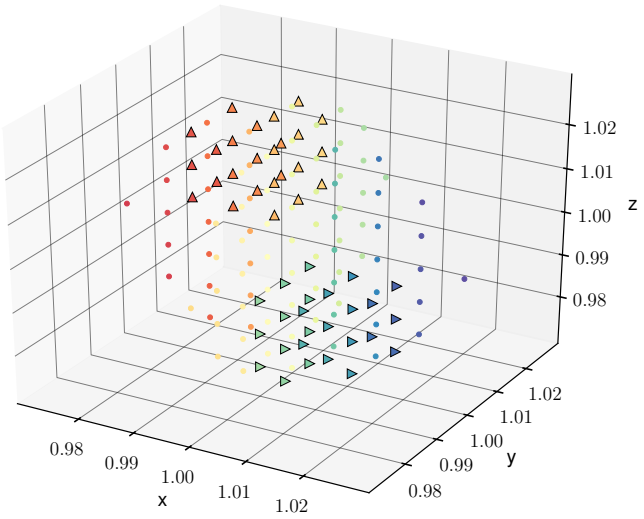

Figure 5.10.: Nodes inside the interaction zone $B_\delta(X_i)$, such that the nodes $\bullet$ are in the middle of the interaction $\{X_j \mid X_j \in B_\delta(X_i) \wedge X_{j_1} = 1 \wedge X_{j_2} = 1\}$, the nodes $\triangle$ are in the octant II $(-\ +\ +)$, and the nodes $\triangleright$ in the octant IV $(+\ -\ +)$.

First, the linearity of the displacement field of the selected nodes (5.9) is shown in Figure 5.11-5.13 for each direction (x, y, z) of the coordinate system. In all Figures there is no displacement in x-direction up to 0.3 and for the other directions up to 0.4. Figure 5.11 shows the displacement in x-direction for the nodes inside the interaction zone. Note, that in this direction at the green-colored nodes in Figure 5.9 the external force is applied. The displacement for nodes $\triangle$ in octant II is negative which agrees with the direction of the external force $b(t, X_i)_1 = -40000\,\mathrm{N}$. Respective for the nodes $\triangleright$ the displacement is positive which agrees with the direction of the external force $b(t, X_i)_1 = +40000\,\mathrm{N}$ too. For the nodes $\bullet$ close to X_i is the displacement is zero. For nodes very close to the boundary of the interaction zone the displacement is in the lower range respective to the nodes in

the corresponding octant. This behavior completely fits to the applied force and the material behavior of the pair-wise force (2.56) of this specific model. Furthermore, the plot of strain versus force in Figure 2.7b shows that the strain relates linear and the displacement in the simulation remains linear for small strains.
Figure 5.12 shows the displacement in y-direction of the nodes inside the interaction zone. In octant II the displacement is negative and the nodes move towards the center X_i and thus the length of the cube shrinks along the direction transverse to the applied force. The displacement of the nodes in octant IV is positive and they move to the center, too. Thus, the length of the cube shrinks along directions transverse to the force. Here, the displacement at the center X_i and nodes close to it is zero. The similarity to the linearity of the strain versus pair-wise force f and the linearity of the displacement field is seen as well.
Figure 5.13 shows the displacement in z-direction of the nodes inside the interaction zone. Due to symmetry the displacement in z-direction of the nodes inside the interaction zone in both octants is similar to the displacement of the nodes in y-direction. Thus, the length in z-direction shrinks, too. The displacement in this direction is also linear.
Furthermore, question *(1.)* can be answered positive, because the displacement is linear in all directions for small strains. Thus, the assumption that the force stays in the linear regime can be made and the assumptions which where made in Section 2.3.2 hold. Therefore, the definitions of the Poisson ratio and the Young modulus for a linear elastic material are applicable.

Second, the focus is on the displacement of the node $X_i = (1\,\mathrm{m}, 1\,\mathrm{m}, 1\,\mathrm{m})^T$ and nodes very close to it. This node is at the center $0.21\,\mathrm{m} \times 0.21\,\mathrm{m} \times 0.21\,\mathrm{m}$ of the cube and the applied external force is symmetric. As a consequence there is no displacement at this point, because the pair-wise force f is symmetric and the pair-wise forces between the nodes X_i in the left of the neighborhood $\{X_j \,|\, X_j \in B_\delta(X_i) \wedge X_{j_1} < 1\}$ and the right of the neighborhood $\{X_j \,|\, X_j \in B_\delta(X_i) \wedge X_{j_2} > 1\}$ add up to zero (conservation of linear momentum). In Figures 5.11-5.13 there is zero displacement at the node X_i and our simulation conserves the linear momentum.

Third, the so-called Poisson effect is studied. The Poisson effect describes the effect that a material expanded in one direction, tends to be shrink in the respective other two directions. The applied force at the green-colored layers in Figure 5.9 expands the cube in x-direction. The negative displacement in contant II and the positive displacement in octant IV indicates that the cube is expanded in this direction. Based on the definition of the Poisson effect the material should shrink in the others directions. The displacement in octant II and octant IV in y-direction

and z-direction indicates this effect. Respective to the Poisson effect these directions decrease. Figures 5.11-5.13 show this behavior clearly. The according Poisson ratio will be studied in Section 5.3.3.

In addressing questions *(1.-3.)* it was shown that the displacement for small deformations in the simulations was linear. Thus, the displacement stays in the linear regime and the validation with the linear elastic theory in the next section is valid. In addition, the considered bond-based softening model satisfies the conservation of linear momentum, and reproduces the Poisson effect. These objectives indicate that this specific version of the bond-based SM model preserves the properties of the continuum model.

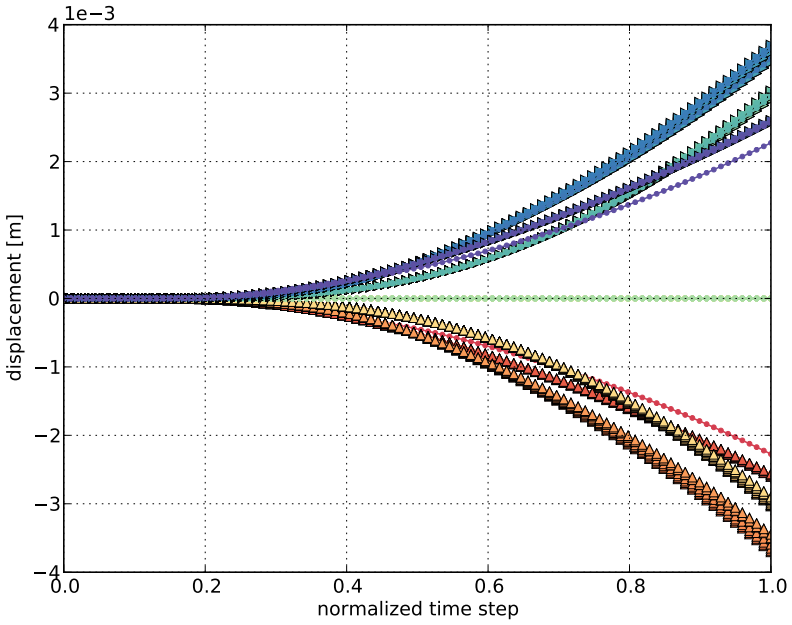

Figure 5.11.: Displacement in x-direction of the nodes inside the neighborhood $B_\delta(X_i)$.

5.3.3. Validation against experimental data

The Young modulus and the Poisson ratio are two characteristic properties of a linear elastic material. For the validation with experimental data the definitions of classical theory [Roy08] of these two material properties are used, see Equation (5.10) and Equation (5.11). For the calculation of α and β, the two specific bond-based

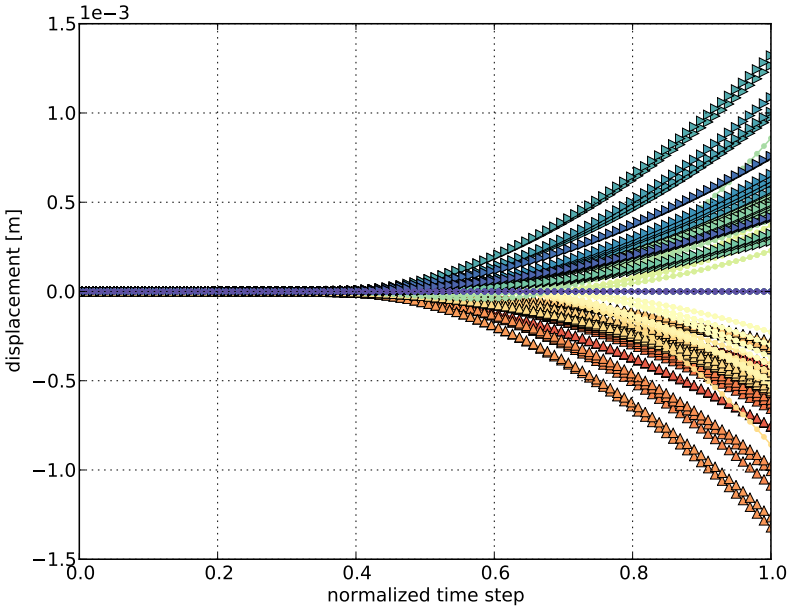

Figure 5.12.: Displacement in y-direction of the nodes inside the neighborhood $B_\delta(X_i)$.

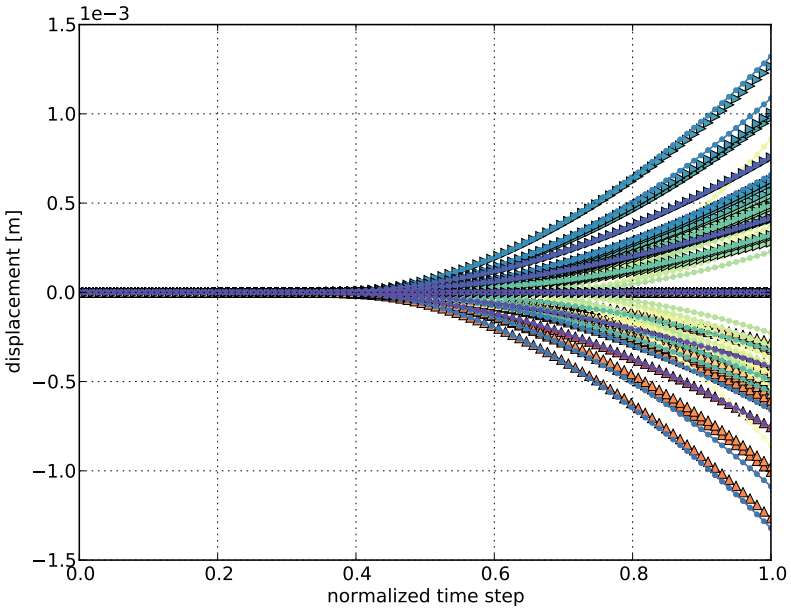

Figure 5.13.: Displacement in z-direction of the nodes inside the neighborhood $B_\delta(X_i)$.

peridynamic material parameters in Section 2.3.2 the material properties of impact modified PMMA in Table 5.4 are used. Now, the discretized softening model is used for the estimation of the Poisson ratio and the Young modulus inside the interaction zone $B_\delta(X_i)$ (see Figure 5.14) via their definition from classical theory. Due to the energy equivalence of the discretized softening model shown in Section 3.1.1 the simulations should reproduce the material parameters, which were used to calculate the softening material parameters α and β. Next, the deduction of the Poisson ratio and the Young modulus is shown.

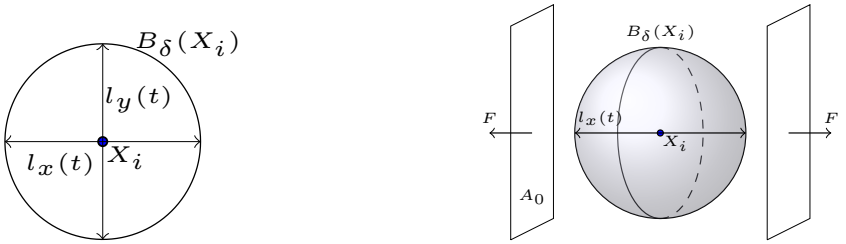

(a) Equation (5.10) shows the time dependent definition of the Poisson ratio $\nu_y : [1, T] \to \mathbb{R}$ inside the neighborhood $B_\delta(X_i)$ with respect to the length change $l_x(t)$ and $l_y(t)$ over time t.

(b) Equation (5.11) shows the time dependent definition of the Young modulus $E : [1, T] \to \mathbb{R}$ inside the neighborhood $B_\delta(X_i)$ with respect to the length change $l_x(t)$ and the force F in x-direction obtained in the cross section A_0.

Figure 5.14.: Sketches for obtaining the time dependent Poisson ratio $\nu_y(t)$ and time dependent Young modulus $E(t)$ inside the interaction $B_\delta(X_i)$. Equation (5.10) shows the time dependent Poisson ratio $\nu_y : [1, T] \to \mathbb{R}$ and Equation (5.11) $E : [1, T] \to \mathbb{R}$ the time dependent Young modulus.

Deduction of the Poisson ratio

The Poisson effect is observed in Section 5.3.2 in the displacement field of the nodes inside the interaction zone. The measurement of this effect is the Poisson ratio and expresses the fraction of the expansion of the material divided by the compression for small length changes. In [Sar+16; HM16] the Poisson ratio was obtained for the whole geometry. Our approach is novel in the way that we measure the Poisson ratio and the Young modulus directly inside in the interaction zone. Figure 5.14a

sketches the interaction zone $B_\delta(X_i)$ of the node X_i centered at the mid of the cube. Where $l_x(t)$, $l_y(t)$, and $l_z(t)$ denote the length at time t in the respective direction. Obviously the length in all directions at time $t = 0$ is 2δ. Equation (5.10) shows the approximation of the Poisson ratio $\nu_y : [1, T] \to \mathbb{R}$ for small length changes by its definition from classical theory

$$\begin{aligned} \nu_y(t) &\approx -\frac{(l_y(t) - l_y(0))l_x(0)}{(l_x(t) - l_x(0))l_y(0)}, \\ \nu_z(t) &\approx -\frac{(l_z(t) - l_z(0))l_x(0)}{(l_x(t) - l_x(0))l_z(0)}. \end{aligned} \tag{5.10}$$

Note that a bond-based softening material model with a pair-wise force $\underline{f}$ is used. Through the simplification, that the force between two nodes X_i and X_j is independent of all other nodes inside the interaction zone, the Poisson ratio is restricted to $1/4$ for a isotropic linear material. This restriction holds for MD simulations with pair-wise potential too [Sil16a]. A extension for bond-based peridynamic material models for arbitrary Poisson ratios is presented in [HM16]. This bond-based model has no extensions and is therefore restricted to a Poisson ratio $\nu = 1/4$. Thus, we used this ratio for the calculation of α and β. However, the same Poisson ratio used in these calculations for the model parameters of this specific bond-based material model should be reproduced in the simulation for the definition of the Poisson ratio from classical theory. Figure 5.15 shows the obtained Poisson ratio $\nu_y(t)$ inside the interaction zone $B_\delta(X_i)$. The red line is the Poisson ratio $\nu = 1/4$, which was used for the estimation of the softening model parameters via energy equivalence from classical theory. The obtained ratio in the simulation starts to increase and after 4 time steps the value is $\approx 1/4$, but then goes continuous linear to 0.8. At this ratio the PMMA material is already broken and thus these values are not plausible and the softening of the bonds should already be started. In addition, the behavior differs from the experiment in Figure 5.14a. Here, the ratio grows linearly at the beginning, but after some time it is nearly constant at 0.4, which lies in the range of expected values for the Poisson ratios of PMMA. Thus, it was not able to capture the time-dependent material behavior shown in Figure 5.8 for this specific bond model. In Addition, the range of the Poisson ratio differs too.

For the increasing Poisson ratio $\nu(t)$ seen in the computational experiment in Figure 5.8 one reason is the shape of the bond force versus strain curve. Recall the

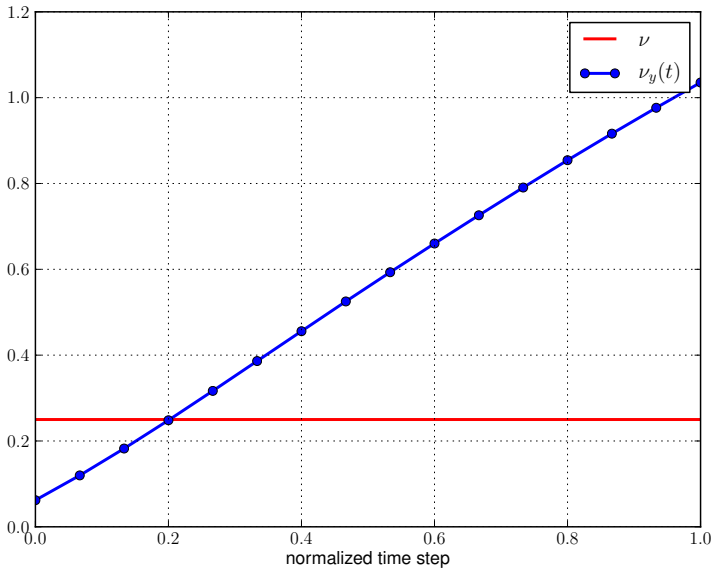

Figure 5.15.: The time depended obtained Poisson ratio $\nu_y(t)$ in y-direction inside the neighborhood $B_\delta(X_i)$. The red line is the Poisson ratio $\nu = 1/4$, which was used in Section 2.3.2 for the calculation of the material parameters of the bond-based softening model via energy equivalence. The obtained values $\nu_z(t)$ are identical, because of symmetry of the Poisson ratio for an elastic isotropic material and therefore not plotted here.

inflection point of the bond force $\underline{f}$ (2.43) in Figure 2.6b, which is the equivalent to the critical strain

$$\underline{s}_c = \frac{r}{\sqrt{\|X' - X\|}}\,.$$

After exceeding this value the force should start to soften. In this case the chosen potential (2.55) is too strong and therefore the force stays in the linear regime well past where the PMMA material begins to soften and fail. This is the primary factor behind the differences' ratio for the bond-based PD in the simulation and the ratio of PMMA in the experiment. In Section 5.3.3 improvements to overcome this issues are discussed.

Deduction of the Young modulus

The Young modulus describes the ratio of the stress to the strain in the material. The definition of the Young modulus according to classical theory adapted for obtaining it inside in the interaction zone is sketched in Figure 5.14b. The ratio F/A_0 is the external force $b(t, X_i)_1$ divided by are of the green-colored nodes in the y-z-plane. The strain $(l_x(t) - x_x(0))/l_x(0)$ is the length change in x-direction proportional to the initial length $l_x(0)$. The initial length $l_x(0)$ is defined by the simulation setup as 2δ. Next, the time-dependent Young modulus $E : [1, T] \to \mathbb{R}$ with respect to the classical theory yields

$$E(t) \approx \frac{F l_x(0)}{A_0 \left(l_x(t) - l_x(0)\right)}. \tag{5.11}$$

The obtained Young modulus $E(t)$ is plotted in blue in Figure 5.16. The two red lines are the minimal value E_{min} and the maximal value E_{max} of the Young modulus fro PMMA given in Table 5.4. After few time steps the Young Modulus is for one time step in the common range for PMMA. Next, the value goes down to zero which does not correspond to its physical behavior. Thus, this specific peridynamic potential can not capture the expected physical behavior of PMMA. As before the exponential bond force is to strong and the Young modulus goes down to zero which is physically not plausible. In addition, the definition of the Young modulus obtained by the experiment is dynamical, but depends on global stress and strain. Here, a quasi-static measurement should be considered to capture these global attributes.

Improvements to overcome these issues

The simulations captured the expected material properties from Table 5.4, but did not account for the strength of PMMA in Figure 5.8. Here, the softening of the bonds starts too “late”. One reason is the inaccuracy of the two parameter exponential function (2.55) used for representing the force in this model. The parameter α and β are related to the strength $\underline{s}_c$ and the fracture toughness $\underline{G}_{\text{PD}}$ and are not independent. For this case the linear elastic coefficient and fracture toughness determine the strength of the softening model. In addition, the force $b(t, X_i)$ applied in the simulations was 10 times the one used in the experiment to see appreciable displacement. This yields a second argument for decoupling these parameters.

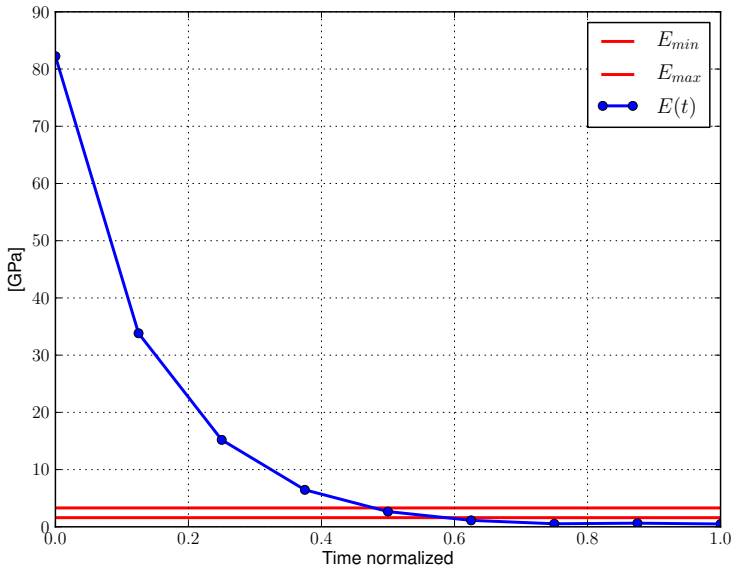

Figure 5.16.: The time depended obtained Young modulus $E(t)$ inside the neighborhood $B_\delta(X_i)$.

The decoupling is possible with the generic softening peridynamic model, because the requirements of the positive, smooth and concave potential function $\underline{F}$ do allow the independent specification of strength and fracture toughness. These properties are determined by $\underline{F}'(0)$ and by $\lim_{r\to\infty} \underline{F}(r)$. The strength is given by the inflection point determined by $r = \sqrt{\overline{z}}$ where $\overline{z}$ is the root of $\underline{F}'(z) + 2z\underline{F}''(z)$. Decoupled approaches, where the elasticity, strength and fracture toughness are independent of each other should be considered.

5.3.4. Summary

The calibration of the model parameters of a specific bond-based peridynamic softening model in Section 2.3.2 were verified for small displacements inside the interaction zone. In the simulations the linearity of the displacement field was verified and the Poisson effect was observed. Thus, the force stays in the linear regime of the corresponding force function for small strain, see Figure 2.6a. The simulations for obtaining the Poisson ratio was conducted identical to a physical experiment. Here, the strength of the bond-based peridynamic softening model did

not correspond to the strength of PMMA in the experiment. The expected Poisson ratio of $1/4$ for bond-based PD material models was observed in the simulation, but the bond force starts to soften too "late" and at Poisson ratios ≥ 0.8 PMMA is already broken. The obtained Young modulus lies in the expected range for PMMA for one time step, but goes down to zero which is not physically correct. Here, the simple two parameter exponential function can not capture the physical behavior of the material.

Therefore, more sophisticated realizations of the bond force model should be applied to capture the same behavior for the Poisson ratio as in the experiment. For Poisson ratios other than $1/4$ state-based PD should be considered for capturing the Poisson ratio of PMMA, which is 0.4. As future work the same energy equivalence and comparison for the state-based peridynamic softening model is to be considered. Here, we started to work on the energy equivalence for three parameter potential with independent material properties. In addition, the Young modulus should be obtained via the global stress-strain with a quasi-static approach.

6.Concluding remarks

In this thesis, the modeling and simulation of cracks and fractures with peridynamics in brittle material was studied. The focus was on the simple bond-based peridynamics theory, which was discretized with the EMU nodal discretization (EMU ND). Most known bond-based peridynamic material models have model parameters depending on the horizon of the interaction zone. The horizon of the interaction zone in the bond-based peridynamic softening model instead describes the length of the process zone associated with the material.
For this model, we showed the calibration using theoretical relations to connect the model parameter to the shear modulus and fracture toughness of Linear Elastic Fracture Mechanics (LEFM) theory in Section 2.3.2. The calibrated model parameters were validated employing the EMU ND. Here, the discrete peridynamics (PD) energy was consistent up to a significantly small error for varying neighbors inside the interaction zone with the energy prescribed by the model, see Section 3.1.1.

The EMU ND is based on neighbor searches in node clouds which is a computationally expensive task. However, to deal with very large node clouds, which are necessary for accurate simulations, the neighborhoods need to be computed in parallel. Therefore, we extended an efficient and general sorting based approach for the neighbor search on GPU in Section 4.1. The original algorithm computed the k-nearest neighbors of a node. In addition, our library FNSG computed the neighbors inside a finite spherical interaction zone. FNSG outperforms the origin single core CPU implementation in most cases. For irregular node clouds, the sub-locality of the employed Morton order as the underlying space-filling curve is taken in account.

To access the full utilization of modern super computers, different acceleration cards in conjunction with all other parts of the system are necessary. Here, we integrated the CUDA programming model for GPU into the High Performance ParallelX framework (HPX). In Section 4.2 we outlined the seamless integration of CUDA devices into HPX, which need special effort by the programmer, especially as the data transfer and the synchronization of the kernel execution for managing the heterogeneous code base is hidden from the programmer. With this abstraction level, the CUDA device is accessed the same way as a CPU in the HPX programming model. This approach outperforms the native CUDA implementation for a single partition. For streaming the data in multiple partitions, the abstraction layer needs to be optimized. Nevertheless, the easy combination of GPU and CPU for multi-physics

simulations is provided. One possible application is the coupling of FEM with PD, where the FEM code is executed on the CPUs and the PD code concurrently on GPUs.

Verification against experimental data is essential for the development of models as well as their accuracy. Possible benchmarks, like histograms of the distribution of fragment sizes after an impact damage, are available in literature. We extend existing algorithms and techniques for the extraction of fragments and waves in Section 4.3. Our algorithm extracts fragments of node-based simulations and generates histograms with the distribution of the size of the fragments. Now, the comparison with these experiments is possible. With the visualization of stress waves, the understanding of propagation and reflection of waves and their caused damage is provided. Our algorithms are applicable even for complex geometries, e.g. the Stanford bunny. For reducing the computational time, we should implement the Paraview plugins in parallel.

In Chapter 5 three numerical results for the initiation and growth of cracks were presented. The propagation waves with the Edge-On impact experiment was studied in Section 5.1. The extracted wave speed at the wave front in the simulation was compared with the one measured in the experiment for Aluminiumoxynitrid (ALON). Here, the bond based peridynamic PMB material model and the bond-based peridynamic DPMB material model were employed. For the PMB model, the wave speed was close to the measured one in the experiment for a coupled horizon $\delta = 3\Delta x$ to the nodal spacing. This relation was obtained by adjusting the dispersion curve for the PMB material model to the one measured in the experiment. For the DPMB material model, the extraction of the wave front was quite challenging and more sophisticated methods, like in Section 4.3.2 should be considered. With these experiments we have shown, that the choice of a "good" ratio of $\delta/\Delta x$ influences the convergence. With the relation $\delta = 3\Delta x$ it was possible to get close to the measured speed, but for $\Delta x \to 0$ no limit for the speed at the wave front was obtained.

From a theoretical point of view the horizon should shrink slower than the nodal spacing for convergence to the local PDE case. Therefore, we studied what a "good" choice of the ratio $\delta/\Delta x$ could be for a wide range of materials from polymethyl methacrylate (PMMA) up to titanium alloy in Section 5.2. Here, the critical traction for Mode *I* crack opening obtained in the simulation was compared with the prescribed value from LEFM theory. For most materials, a limit exists for the critical traction and differs by $\approx 5\,\%$ from the prescribed value of the LEFM theory. In addition, the critical traction depends linearly on the critical stress intensity factor

and is independent of the material density for most materials.
For the lower range PMMA and the upper range titanium alloy, a “good” choice for the nodal spacing can be found for each horizon and vice versa, if an error of $5\,\%$ is applicable. In the end, we found no consistent pattern from which a simple relation for between the horizon and the nodal spacing could be determined. All we can say is that the DPMB material model with the EMU ND without any volume correction is very robust.

In Section 5.3 our calibrated specific bond-based peridynamic softening material model was numerically verified for small deformations. First, the linearity of the displacement field and the Poisson effect inside the interaction zone were observed. Second, the material behavior of the Poisson ratio was compared with the one measured for PMMA in a real physical tensile test. The Poisson ratio in the simulation did not capture the material behavior in the experiment. The Poisson ratio and the Young modulus were for one time step in the common range of PMMA, but the strength of the material did not correspond with the one of PMMA. Our two parameter exponential function as the non-local PD potential was not able to capture the complex material behavior. With this potential, the two model parameters are not independent and the fracture toughness, as well as the shear modulus, determine the strength of the material model. Here, more complex potential functions or the state-based PD should be considered to capture the material behavior in the experiment.

In summary, we showed interesting problems for the modeling, simulation, and validation of cracks with bond-based PD material models. In general, the modeling and simulation of cracks and fractures in brittle material with the bond-based peridynamic and the EMU nodal discretization is applicable for the comparison with experimental data or LEFM theory. Undoubtedly, the choice of the pair-wise force function influences the material behavior significantly and more general functions should be considered for capturing complex material behavior. The “good” choice for the ratio $\delta/\Delta x$ for numerical simulation with bond-based PD discretized with EMU ND still remains an open question.

Outlook

Following essentials could be addressed to extend or complete the research in this thesis

- For the sorting-based approach for neighbor search on GPU in Section 4.1 the sub-optimal locality of the Morton order took into account for some node clouds $\mathbf{C}$. Here, different space-filling curves could be considered to overcome this issue.
- In Section 4.2 an overhead for the seamless integration of CUDA into the High Performance ParallelX framework was seen for multiple-partitions with streaming. In addition, to improvements to the programmability, the abstraction layer should be optimized for streaming to get the same result as for one single partition.
- Apply the new techniques, e.g. extraction of fragments in Section 4.3 for the comparison with experimental data. Here, the histograms of the distribution of the quantity of interest, like the mass of the fragments, can be compared with experimental data.
- The bond-based peridynamic softening model in Section 2.3.2 provides horizon-independent material parameters. One specific SM model was numerically verified in Section 3.1.1, but the identical material behavior as in the experiment was not captured in Section 5.3. To overcome this issue the three parameter SM model or the stated-based peridynamic SM model should be studied.

A.Appendix

A.1. Code snippets

```
1  // Copyright (c)       2015 Patrick Diehl
2  #include <hpx/include/iostreams.hpp>
3  #include <hpx/lcos/future.hpp>
4
5  #include <hpxcl/cuda.hpp>
6  #include <sstream>
7
8  // hpx_main, is the actual main called by hpx
9  int hpx_main(int argc, char* argv[]) {
10   {
11     // Get list of available CUDA Devices.
12     std::vector<hpx::cuda::device> devices = hpx::cuda::get_all_devices(1,0).get();
13
14     // Check whether there are any devices
15     if (devices.size() < 1) {
16       hpx::cerr << "No CUDA devices found!" << hpx::endl;
17       return hpx::finalize();
18     }
19
20     hpx::cout << hpx::endl << "Devices:" << hpx::endl << hpx::endl;
21
22     // Print information about every device
23     for (auto &device : devices) {
24       device.get_cuda_info();
25       hpx::cout << hpx::endl;
26     }
27   }
28   return hpx::finalize();
29 }
```

Listing A.1: Example of accessing all local and remote devices with HPXCL framework.

A.2. Results from digital image correlation

Figure A.1 shows the first picture taken by the stereo-microscope in the experiment. The small black dotted markers are mechanically manufactured to the specimen. These markers are tracked by the digital image correlation (DIC) with respect to the reference configuration to extract the quantity of interest, i.e. the displacement. With the displacement the Poisson ratio (like in Equation (5.10)) is computed and plotted over time (see Figure 5.8).

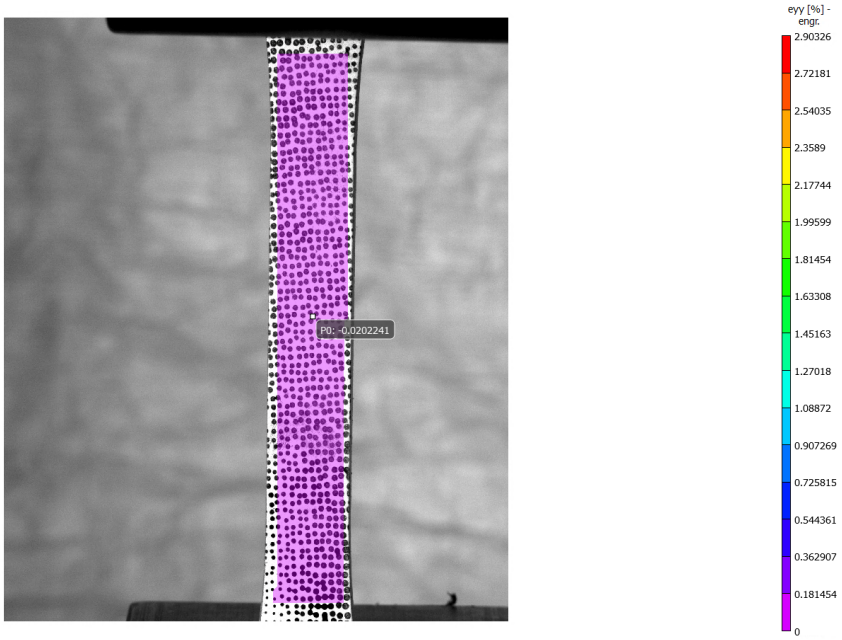

Figure A.1.: Extracted strain in y-direction of the experiment via digital image correlation.

Index of abbreviations

AGAS Active Global Address Space
ALON Aluminiumoxynitrid
API application programming interface
CCM classical continuum mechanics
CFL Courant–Friedrichs–Lewy
CUDA Compute Unified Device Architecture
CPU Central Processing Unit
DIC digital image correlation
DPMB Discrete Prototype Microelastic Material
EMU ND EMU nodal discretization
EOI Edge-On impact
FEM Finite Element Method
FLOPS floating point operation per second
FNSG Fast neighbor search on GPU
GPU Graphics Processing Unit
GPGPU general-purpose computing on graphics processing units
HPC high performance computing
HPX High Performance ParallelX framework
HPXCL HPX compute language
IEEE Institute of Electrical and Electronics Engineers
INS Institute for Numerical Simulation
LEFM Linear Elastic Fracture Mechanics
LPS linear peridynamic solid
MD molecular dynamics
MSB most significant bit
OpenCL Open Compute Language
ORNL Oak Ridge National Laboratory
PD peridynamics
PDE partial differential equation
PMB Prototype Microelastic Brittle
PMMA polymethyl methacrylate
PUM partition of unity method
SDK Software Development Kit
SFC space-filling curve

SIMT single instruction multiple threads
SM softening model
SPH smoothed particle hydrodynamics
XFEM eXtended Finite Element Method

Notation

$\lvert \cdot \rvert$	Absolute value
$a(t, X)$	Acceleration in Lagrangian coordinates $[\mathrm{m\,s^{-2}}]$
$B_\delta(X)$	Interaction zone
$\lvert B_\delta(X_i) \rvert$	Amount of neighbors inside the interaction zone B_δ
$C(\phi)$	Cauchy–Green strain tensor, also right Cauchy–Green strain tensor (2.6)
$\mathbb{C}$	Hookean tensor (2.19)
$\mathbf{C}$	Node cloud, simply Cloud $\mathbf{C} := \{X_1, \ldots, X_n \lvert X_i \in \mathbb{R}^d\}$
$\times$	Cross product
c	Stiffness constant
s_c	Critical stretch for bond failure $[\mathrm{m}]$
$\bullet$	Dot product
$\mathbb{R}^d$	d-dimensional vector space
d	Dimension $d \in \{1, 2, 3\}$
$E(\phi)$	Strain tensor (2.7)
$\lVert \cdot \rVert$	Euclidean distance
D_t	Strain matrix $D_t \in \mathbb{R}^d \times \mathbb{R}^d$ at time t
F	Positive, smooth and concave potential function (2.41)
f	Pair-wise force function
G	Strain Energy release rate, simply energy release rate $[\mathrm{J\,m^{-2}}]$

Δx Nodal spacing $[\mathrm{m}]$

$\phi(t, X)$ Deformation (2.1)

$\mathbb{I}$ Identity

id Identity map with $id(X) = X$

$J(r)$ Influence function with $0 \leq J(r) \leq M$ for $0 \leq r \leq 1$ and $J(r) = 0$ for $1 < r$

K Bulk modulus $[\mathrm{Pa}]$

K_{Ic} Critical stress intensity factor or fracture toughness (Mode I) $[\mathrm{Pa}\sqrt{\mathrm{m}}]$

$\mathcal{O}$ Bachmann–Landau notation Big Oh, see [Lan00]

o Bachmann–Landau notation Small Oh, see [Lan00]

ν Poisson's ratio

T Stress tensor (2.9)

t Time $[\mathrm{s}]$

$u(t, X)$ Displacement $[\mathrm{m}]$ (2.2)

$\mathbf{V}^2$ Circular area $\pi\delta^2$ $[\mathrm{m}^2]$

$\mathbf{V}^3$ Spherical volume $4\pi\delta^3/3$ $[\mathrm{m}^3]$

$\mathbf{V}_i$ Volume $[\mathrm{m}^3]$

$W(\mathbf{s})$ Strain energy density $[\mathrm{J\,m}^{-3}]$

X Lagrangian coordinate

$x(t, X)$ Eulerian coordinate

$\mathtt{E}$ Young's modulus $[\mathrm{Pa}]$

δ Horizon $[\mathrm{m}]$

$\varepsilon_{ij}(u)$ Linearized strain (2.17)

μ Shear modulus $[\mathrm{Pa}]$

$\Omega(t)$ Current configuration at time t

Ω_0 Reference configuration at time $t = 0$

ω Scalar micro potential

ρ Material density $[\mathrm{kg\,m^{-3}}]$

$\sigma_{ij}(u)$ Linearized stress (2.19)

$\vec{\sigma}$ Traction $[\mathrm{N\,m^{-2}}]$

$\vec{\sigma}_a(t, X_i)$ Virial stress (5.7)

$\vec{\sigma}_c$ Critical traction $[\mathrm{N\,m^{-2}}]$ (5.6)

List of Tables

List of Figures

Bibliography

[Adv12] Office of Advanced Scientific Computing Research (ASCR). *X-Stack: programming Challenges, Runtime Systems, and Tools*. 2012. URL: `http://science.energy.gov/~/media/grants/pdf/lab-announcements/2012/LAB_12-619.pdf` (cit. on p. 53).

[AGM12] A. Agwai, I. Guven, and E. Madenci. "Drop-Shock Failure Prediction in Electronic Packages by Using Peridynamic Theory." In: *Components, Packaging and Manufacturing Technology, IEEE Transactions on* 2.3 (Mar. 2012), pp. 439–447. ISSN: 2156-3950 (cit. on p. 43).

[AP11] Burak Aksoylu and Michael L Parks. "Variational theory and domain decomposition for nonlocal problems." In: *Applied Mathematics and Computation* 217.14 (2011), pp. 6498–6515 (cit. on p. 36).

[Arg+79] J.H. Argyris et al. "Finite element method — the natural approach." In: *Computer Methods in Applied Mechanics and Engineering* 17–18, Part 1 (1979), pp. 1–106. ISSN: 0045-7825 (cit. on p. 7).

[Ary+94] Sunil Arya et al. "An Optimal Algorithm for Approximate Nearest Neighbor Searching in Fixed Dimensions." In: *Fifth Annual ACM-SIAM Symposium on Discrete Algorithms* 5 (1994), pp. 573–582 (cit. on p. 44).

[AS97] Srinivas Aluru and Fatih E. Sevilgen. "Parallel Domain Decomposition and Load Balancing Using Space-Filling Curves." In: *in Proceedings of the 4th IEEE Conference on High Performance Computing*. 1997, pp. 230–235 (cit. on p. 45).

[AW59] B. J. Alder and T. E. Wainwright. "Studies in Molecular Dynamics. I. General Method." In: *The Journal of Chemical Physics* 31.2 (1959), pp. 459–466 (cit. on p. 7).

[Bad13] Michael Bader. *Space-Filling Curves – An Introduction with Applications in Scientific Computing*. Springer Berlin Heidelberg, 2013 (cit. on p. 45).

[BB87] M.J. Berger and S.H. Bokhari. "A Partitioning Strategy for Nonuniform Problems on Multiprocessors." In: *Computers, IEEE Transactions on* C-36.5 (May 1987), pp. 570–580. ISSN: 0018-9340 (cit. on p. 43).

[BB99] T. Belytschko and T. Black. “Elastic crack growth in finite elements with minimal remeshing.” In: *International Journal for Numerical Methods in Engineering* 45.5 (1999), pp. 601–620. ISSN: 1097-0207 (cit. on p. 7).

[BBK01] C. Böhm, S Berchtold, and A. D. Keim. “Searching in high-dimensional spaces: Index structures for improving the performance of multimedia databases.” In: *ACM Computing Sruveys*. 33. 2001, pp. 322–373 (cit. on p. 45).

[BD12] Florin Bobaru and Monchai Duangpanya. “A peridynamic formulation for transient heat conduction in bodies with evolving discontinuities.” In: *Journal of Computational Physics* 231.7 (2012), pp. 2764–2785. ISSN: 0021-9991 (cit. on p. 33).

[Ben92] David J. Benson. “Computational methods in Lagrangian and Eulerian hydrocodes.” In: *Computer Methods in Applied Mechanics and Engineering* 99.2–3 (1992), pp. 235–394. ISSN: 0045-7825 (cit. on p. 72).

[BFS09] R. Brannon, A. Fossum, and E. Strack. *Kayenta: Theory and User’s Guide*. Tech. rep. SAND2009-2282. Albuquerque: Sandia National Laboratories, 2009 (cit. on pp. 72, 77).

[BG04] Hans-Joachim Bungartz and Michael Griebel. “Sparse Grids.” In: *Acta Numerica* 13 (2004), pp. 1–123 (cit. on pp. 78–80).

[BH11] Florin Bobaru and Youn Doh Ha. “Adaptive refinement and multiscale modeling in 2d peridynamics.” In: *International Journal for Multiscale Computational Engineering* 9.6 (2011), pp. 635–660. ISSN: 1543-1649 (cit. on pp. 33, 92).

[BH12] Florin Bobaru and Wenke Hu. “The Meaning, Selection, and Use of the Peridynamic Horizon and its Relation to Crack Branching in Brittle Materials.” English. In: *International Journal of Fracture* 176.2 (2012), pp. 215–222. ISSN: 0376-9429 (cit. on pp. 75, 77).

[BM14] José C Bellido and Carlos Mora-Corral. “Existence for nonlocal variational problems in peridynamics.” In: *SIAM Journal on Mathematical Analysis* 46.1 (2014), pp. 890–916 (cit. on p. 36).

[Bra03] Dietrich Braess. *Finite Elemente: Theorie, schnelle Löser und Anwendungen in der Elastizitätstheorie (German Edition)*. 3., korr. u. ergänzte Aufl. Springer, Mar. 2003. ISBN: 9783540001225 (cit. on pp. 8, 12).

[Bre14] Michael Breitenfeld. “Quasi-static non-ordinary state-based peridynamics for the modeling of 3D fracture.” PhD thesis. University of Illinois at Urbana-Champaign, May 2014 (cit. on p. 60).

[CG11] X. Chen and Max Gunzburger. “Continuous and discontinuous finite element methods for a peridynamics model of mechanics.” In: *Computer Methods in Applied Mechanics and Engineering* 200.9–12 (2011), pp. 1237–1250. ISSN: 0045-7825 (cit. on p. 31).

[Cha06] Timothy M. Chan. *A minimalist's implementation of an approximate nearest neighbor algorithm in fixed dimensions*. `https://cs.uwaterloo.ca/~tmchan/sss.ps`. May 2006 (cit. on p. 48).

[CK10] Michael Connor and Piyush Kumar. *The Simple, Thread-safe Approximate Nearest Neighbor (STANN) C++ Library*. `https://sites.google.com/a/compgeom.com/stann/Home`. Nov. 2010 (cit. on p. 49).

[CY98] Robert Cook and Warren Young. *Advanced Mechanics of Materials (2nd Edition)*. 2nd ed. Prentice Hall, Sept. 1998. ISBN: 9780133969610 (cit. on pp. 80, 89).

[Die+16] Patrick Diehl et al. “Bond-based peridynamics: a quantitative study of Mode I crack opening.” In: *International Journal of Fracture* (2016), pp. 1–14. ISSN: 1573-2673 (cit. on p. 5).

[Die+ed] Patrick Diehl et al. “Extraction of fragments and waves after impact damage in particle-based simulations.” In: *Meshfree Methods for Partial Differential Equations*. Ed. by Michael Griebel and Marc Alexander Schweitzer. Springer, accepted (cit. on pp. 5, 44, 61, 62).

[Die12] Patrick Diehl. “Implementierung eines Peridynamik-Verfahrens auf GPU.” Diplomarbeit. Institute of Parallel and Distributed Systems, University of Stuttgart, 2012 (cit. on pp. 31, 75).

[DKD13] Ali Dashti, Ivan Komarov, and Roshan M. D'Souza. “Efficient Computation of k-Nearest Neighbor Graphs for Large High-Dimensional Data Sets on GPU Clusters.” In: *plosone.org*. 2013 (cit. on p. 44).

[DT15] Qiang Du and Xiaochuan Tian. “Robust Discretization of Nonlocal Models Related to Peridynamics.” English. In: *Meshfree Methods for Partial Differential Equations VII*. Ed. by Michael Griebel and Marc Alexander Schweitzer. Vol. 100. Lecture Notes in Computational Science and Engineering. Springer International Publishing, 2015, pp. 97–113. ISBN: 9783319068978 (cit. on pp. 37, 38).

[DT16] Patrick Diehl and Lukas Troska. *Fast Neighbor Search on GPUs (FNSG)*. `http://schweitzer.ins.uni-bonn.de/software/fnsg/`. Aug. 2016 (cit. on p. 4).

[Du+12a] Qiang Du et al. "A new approach for a nonlocal, nonlinear conservation law." In: *SIAM Journal on Applied Mathematics* 72.1 (2012), pp. 464–487 (cit. on p. 36).

[Du+12b] Qiang Du et al. "Analysis and approximation of nonlocal diffusion problems with volume constraints." In: *SIAM review* 54.4 (2012), pp. 667–696 (cit. on p. 36).

[Du+13a] Qiang Du et al. "A nonlocal vector calculus, nonlocal volume-constrained problems, and nonlocal balance laws." In: *Mathematical Models and Methods in Applied Sciences* 23.03 (2013), pp. 493–540 (cit. on p. 36).

[Du+13b] Qiang Du et al. "Analysis of the volume-constrained peridynamic Navier equation of linear elasticity." In: *Journal of Elasticity* 113.2 (2013), pp. 193–217 (cit. on p. 36).

[Du16a] Qiang Du. "Handbook of Peridynamic Modeling." In: ed. by Florin Bobaru et al. CRC Press, Sept. 2016. Chap. Nonlocal Calculus of Variations and Well-Posedness of Peridynamics, pp. 65–88 (cit. on p. 36).

[Du16b] Qiang Du. "Handbook of Peridynamic Modeling." In: ed. by Florin Bobaru et al. CRC Press, Sept. 2016. Chap. Local Limits and Asymptotically Compatible Discretizations, pp. 89–110 (cit. on pp. 37, 38).

[DZ11] Qiang Du and Kun Zhou. "Mathematical analysis for the peridynamic nonlocal continuum theory*." eng. In: *ESAIM: Mathematical Modelling and Numerical Analysis* 45.2 (Jan. 2011), pp. 217–234 (cit. on p. 36).

[EE72] A.Cemal Eringen and D.G.B. Edelen. "On nonlocal elasticity." In: *International Journal of Engineering Science* 10.3 (1972), pp. 233–248. ISSN: 0020-7225 (cit. on p. 8).

[EEM12] H.A. Erbay, A. Erkip, and G.M. Muslu. "The Cauchy problem for a one-dimensional nonlinear elastic peridynamic model." In: *Journal of Differential Equations* 252.8 (2012), pp. 4392–4409. ISSN: 0022-0396 (cit. on p. 36).

[EGK11] Christof Eck, Harald Garcke, and Peter Knabner. *Mathematische Modellierung (Springer-Lehrbuch) (German Edition)*. 2. überarb. Aufl. 2011. Springer, Mar. 2011. ISBN: 9783642184239 (cit. on pp. 8, 12).

[ELP13] Etienne Emmrich, Richard B. Lehoucq, and Dimitri Puhst. “Peridynamics: A Nonlocal Continuum Theory.” In: *Meshfree Methods for Partial Differential Equations VI*. Ed. by Michael Griebel and Alexander Marc Schweitzer. Berlin, Heidelberg: Springer Berlin Heidelberg, 2013, pp. 45–65. ISBN: 9783642329791 (cit. on p. 36).

[EP13] Etienne Emmrich and Dimitri Puhst. “Well-posedness of the peridynamic model with Lipschitz continuous pairwise force function.” In: *Commun. Math. Sci* 11.4 (2013), pp. 1039–1049 (cit. on p. 36).

[EW07a] E. Emmrich and O. Weckner. “The peridynamic equation and its spatial discretization.” In: *Mathematical Modelling and Analysis* 12.1 (2007), pp. 17–27 (cit. on p. 31).

[EW07b] Etienne Emmrich and Olaf Weckner. “On the well-posedness of the linear peridynamic model and its convergence towards the Navier equation of linear elasticity.” In: *Commun. Math, Sci.* Vol. 5. 4. 2007, pp. 851–864 (cit. on p. 36).

[GHM14] Georg C. Ganzenmüller, Stefan Hiermaier, and Michael May. “Improvements to the Prototype Micro-Brittle Linaear Elasticity Model of Peridynamics.” In: *Meshfree Methods for Partial Differential Equations VII*. Ed. by M. Griebel and M. A. Schweitzer. Vol. 100. Lecture Notes in Computational Science and Engineering 7. Springer, 2014 (cit. on pp. 39, 77).

[GKZ07] M. Griebel, S. Knapek, and G. Zumbusch. *Numerical Simulation in Molecular Dynamics*. Berlin, Heidelberg: Springer, 2007. ISBN: 9783540680949 (cit. on p. 44).

[GM77] R. A. Gingold and J. J. Monaghan. “Smoothed particle hydrodynamics: theory and application to non-spherical stars.” In: *Monthly Notices of the Royal Astronomical Society* 181.3 (1977), pp. 375–389 (cit. on p. 43).

[Gre16] Green Car Congress. *Initial details on fiery crash involving BYD e6 that killed 3*. `http://www.greencarcongress.com/2012/05/bydcrash-20120528.html`. Nov. 2016 (cit. on p. 1).

[Gri21] A. A. Griffith. “The Phenomena of Rupture and Flow in Solids.” In: *Philosophical Transactions of the Royal Society of London A: Mathematical, Physical and Engineering Sciences* 221.582-593 (1921), pp. 163–198. ISSN: 0264-3952 (cit. on p. 7).

[Hah76] Hans Georg Hahn. *Bruchmechanik: Einführung in die theoretischen Grundlagen (Leitfaden der angewandten Mathematik und Mechanik) (German Edition)*. B. G. Teubner, 1976. ISBN: 9783519023296 (cit. on p. 20).

[HB10] Y. D. Ha and Florin Bobaru. "Studies of dynamic crack propagation and crack branching with peridynamics." English. In: *International Journal of Fracture* 162.1-2 (2010), pp. 229–244. ISSN: 0376-9429 (cit. on pp. 82, 89).

[HB11] Y. D. Ha and Florin Bobaru. "Characteristics of dynamic brittle fracture captured with peridynamics." In: *Engineering Fracture Mechanics* 78.6 (2011), pp. 1156–1168. ISSN: 0013-7944 (cit. on pp. 82, 89).

[HHB10] W. Hu, Y. D. Ha, and F. Bobaru. *Numerical integration in peridynamics*. Tech. rep. University of Nebraska-Lincoln, Sept. 2010 (cit. on pp. 83, 89).

[HHB12] Wenke Hu, Y. D. Ha, and Florin Bobaru. "Peridynamic model for dynamic fracture in unidirectional fiber-reinforced composites." In: *Computer Methods in Applied Mechanics and Engineering* 217–220 (2012), pp. 247–261. ISSN: 0045-7825 (cit. on pp. 82, 89).

[HM16] Yile Hu and Erdogan Madenci. "Bond-based peridynamics with an arbitrary poisson's ratio." In: *57th AIAA/ASCE/AHS/ASC Structures, Structural Dynamics, and Materials Conference*. American Institute of Aeronautics and Astronautics Inc, AIAA, 2016. ISBN: 9781624103926 (cit. on pp. 98, 99).

[HS14] Steven F. Henke and Sachin Shanbhag. "Mesh sensitivity in peridynamic simulations." In: *Computer Physics Communications* 185.1 (2014), pp. 181–193. ISSN: 0010-4655 (cit. on p. 62).

[Hu+12] Wenke Hu et al. "The formulation and computation of the nonlocal J-integral in bond-based peridynamics." English. In: *International Journal of Fracture* 176.2 (2012), pp. 195–206. ISSN: 0376-9429 (cit. on p. 33).

[Jen13] Christopher Jensen. *Tesla Says Car Fire Started in Battery*. `http://wheels.blogs.nytimes.com/2013/10/02/highway-fire-of-tesla-model-s-included-its-lithium-battery/`. The New York Times – Wheels. Oct. 2013 (cit. on p. 1).

[JLL90] Richard James, Robert Lipton, and Adam Lutoborski. “Laminar Elastic Composites with Crystallographic Symmetry.” In: *SIAM Journal on Applied Mathematics* 50.3 (1990), pp. 683–702. ISSN: 00361399 (cit. on pp. 26, 27).

[Kai+15a] Hartmut Kaiser et al. “Higher-level Parallelization for Local and Distributed Asynchronous Task-based Programming.” In: *Proceedings of the First International Workshop on Extreme Scale Programming Models and Middleware*. ESPM ’15. Austin, Texas: ACM, 2015, pp. 29–37. ISBN: 9781450339964 (cit. on p. 54).

[Kai+15b] Hartmut Kaiser et al. *hpx: HPX V0.9.10: A general purpose C++ runtime system for parallel and distributed applications of any scale*. Mar. 2015 (cit. on p. 53).

[Kil08] Bahattin Kilic. “Peridynamic theory for progressive failure prediction in homogeneous and heterogeneous materials.” PhD thesis. The Univeristy Of Arizona, 2008 (cit. on p. 31).

[KM10] Bahattin Kilic and Erdogan Madenci. “Coupling of peridynamic theory and the finite element method.” In: *Journal of Mechanics of Materials and Structures* 5.5 (2010), pp. 707–733 (cit. on pp. 43, 89).

[Krö67] E. Kröner. “Elasticity theory of materials with long range cohesive forces.” In: *International Journal of Solids and Structures* 3.5 (1967), pp. 731–742. ISSN: 0020-7683 (cit. on p. 8).

[Kun11] I. A. Kunin. *Elastic Media with Microstructure I: One-Dimensional Models (Springer Series in Solid-State Sciences)*. Softcover reprint of the original 1st ed. 1982. Springer, Dec. 2011. ISBN: 9783642817502 (cit. on p. 14).

[Kun12] I. A. Kunin. *Elastic Media with Microstructure II: Three-Dimensional Models (Springer Series in Solid-State Sciences)*. Softcover reprint of the original 1st ed. 1983. Springer, Jan. 2012. ISBN: 9783642819629 (cit. on p. 14).

[Lan00] Edmund Landau. *Handbuch der Lehre von der Verteilung der Primzahlen*. American Mathematical Society, May 2000. ISBN: 9780821826508 (cit. on p. viii).

[Lea+13] R. Brian Leavy et al. “Edge on Impact Simulations and Experiments.” In: *Procedia Engineering* 58 (2013). Proceedings of the 12th Hypervelocity Impact Symposium, pp. 445–452. ISSN: 1877-7058 (cit. on p. 72).

[Lei+12] Pedro Leite et al. “Nearest Neighbor Searches on the GPU.” English. In: *International Journal of Parallel Programming* 40.3 (2012), pp. 313–330. ISSN: 0885-7458 (cit. on p. 44).

[LH12a] Wenyang Liu and Jung-Wuk Hong. “A coupling approach of discretized peridynamics with finite element method.” In: *Computer Methods in Applied Mechanics and Engineering* 245–246 (2012), pp. 163–175. ISSN: 0045-7825 (cit. on pp. 43, 89).

[LH12b] Wenyang Liu and Jung-Wuk Hong. “Discretized peridynamics for brittle and ductile solids.” In: *International Journal for Numerical Methods in Engineering* 89.8 (2012), pp. 1028–1046. ISSN: 1097-0207 (cit. on pp. 31, 43).

[Lip14] Robert Lipton. “Dynamic Brittle Fracture as a Small Horizon Limit of Peridynamics.” English. In: *Journal of Elasticity* 117.1 (2014), pp. 21–50. ISSN: 0374-3535 (cit. on p. 21).

[Lip15] R. P. Lipton. “Handbook of Peridynamic Modeling.” In: ed. by Florin Bobaru et al. Modern Mechanics and Mathematics. Chapman and H, Nov. 2015. Chap. Dynamic brittle fracture as an upscaling of unstable mesocopic dynamics, pp. 3–20 (cit. on p. 21).

[Lit10] David J Littlewood. “Simulation of dynamic fracture using peridynamics, finite element modeling, and contact.” In: *ASME 2010 International Mechanical Engineering Congress and Exposition*. American Society of Mechanical Engineers. 2010, pp. 209–217 (cit. on p. 43).

[Lub+12] Gilles Lubineau et al. “A morphing strategy to couple non-local to local continuum mechanics.” In: *Journal of the Mechanics and Physics of Solids* 60.6 (2012), pp. 1088–1102. ISSN: 0022-5096 (cit. on p. 43).

[M A03] M. A. Schweitzer. *A Parallel Multilevel Partition of Unity Method for Elliptic Partial Differential Equations*. Vol. 29. Lecture Notes in Computational Science and Engineering. Springer, 2003 (cit. on p. 45).

[MA10] David M. Mount and Sunil Arya. *ANN: A Library for Approximate Nearest Neighbor Searching Version 1.1.2*. `http://www.cs.umd.edu/~mount/ANN/`. Jan. 2010 (cit. on p. 44).

[MB96] J. M. Melenk and I. Babuska. *The Partition of Unity Finite Element Method: Basic Theory and Applications*. 1996 (cit. on p. 7).

[MD13] Tadele Mengesha and Qiang Du. “Analysis of a scalar peridynamic model with a sign changing kernel.” In: *Discrete Contin. Dynam. Systems B* 18 (2013), pp. 1415–1437 (cit. on p. 37).

[MD14a] Tadele Mengesha and Qiang Du. “Nonlocal constrained value problems for a linear peridynamic Navier equation.” In: *Journal of Elasticity* 116.1 (2014), pp. 27–51 (cit. on p. 37).

[MD14b] Tadele Mengesha and Qiang Du. “The bond-based peridynamic system with Dirichlet-type volume constraint.” In: *Proceedings of the Royal Society of Edinburgh: Section A Mathematics* 144.01 (2014), pp. 161–186 (cit. on p. 37).

[MD15] Tadele Mengesha and Qiang Du. “On the variational limit of a class of nonlocal functionals related to peridynamics.” In: *Nonlinearity* 28.11 (2015), p. 3999 (cit. on pp. 36, 37).

[MDB99] Nicolas Moës, John Dolbow, and Ted Belytschko. “A finite element method for crack growth without remeshing.” In: *International Journal for Numerical Methods in Engineering* 46.1 (1999), pp. 131–150. ISSN: 1097-0207 (cit. on p. 7).

[MG95] M. Marder and Steve Gross. “Origin of crack tip instabilities.” In: *J. Mech. Phys. Solids* (1995), pp. 1–48 (cit. on p. 7).

[Mic09] Michael Connor and Piyush Kumar. “Fast construction of k-Nearest Neighbor Graphs for Point Clouds.” In: *IEEE Transactions on Visualization and Computer Graphics*. 2009 (cit. on pp. 44, 45, 47, 48, 50).

[Mil02] Graeme W. Milton. *The Theory of Composites*. Cambridge Books Online. Cambridge University Press, 2002. ISBN: 9780511613357 (cit. on p. 26).

[ML93] M. Marder and Xiangming Liu. “Instability in lattice fracture.” In: *Phys. Rev. Lett.* 71 (15 Oct. 1993), pp. 2417–2420 (cit. on p. 7).

[MO14] Erdogan Madenci and Erkan Oterkus. “Peridynamic Theory and Its Applications.” In: ed. by Erdogan Madenci and Erkan Oterkus. Springer, 2014. Chap. Introduction, pp. 1–18 (cit. on pp. 7, 8).

[MS07] Richard W. Macek and Stewart A. Silling. “Peridynamics via finite element analysis.” In: *Finite Elements in Analysis and Design* 43.15 (2007), pp. 1169–1178. ISSN: 0168-874X (cit. on p. 89).

[MS14] M. A. Schweitzer and S. Wu. “Numerical Integration of on-the-fly-computed Enrichment Functions in the PUM.” In: *Meshfree Methods for Partial Differential Equations VII*. Ed. by M. Griebel and M. A. Schweitzer. Vol. 100. Lecture Notes in Computational Science and Engineering. Also available as INS Preprint No. 1406. Springer, 2014 (cit. on p. 43).

[MWK01] J. Mellor-Crummey, D. Whalley, and K Kennedy. “Improving memory hierarchy performance for irregular applications using data and computation reorderings.” In: *International Journal of Parallel Programming*. Vol. 29. June 2001, pp. 217–247 (cit. on p. 45).

[NN97] S.A. Nene and S.K Nayar. “A simple algorithm for nearest neighbor search in high dimensions.” In: *IEEE J PAMI* 19 (1997), pp. 989–1003 (cit. on p. 44).

[Ohn13] Alan Ohnsman. *Tesla Says Model S Driver Unhurt in Mexico Crash*. `http://www.bloomberg.com/news/articles/2013-10-28/tesla-says-model-s-driver-unhurt-in-mexico-crash`. Bloomberg. Oct. 2013 (cit. on p. 1).

[Ote+12] Erkan Oterkus et al. “Combined finite element and peridynamic analyses for predicting failure in a stiffened composite curved panel with a central slot.” In: *Composite Structures* 94.3 (2012), pp. 839–850. ISSN: 0263-8223 (cit. on p. 43).

[Owe05] J. M. Owen. “SPH and Material Failure.” In: *Proceedings from the 5LC 2005*. 2005 (cit. on p. 61).

[Par+08] Michael L. Parks et al. “Implementing peridynamics within a molecular dynamics code.” In: *Computer Physics Communications* 179.11 (2008), pp. 777–783. ISSN: 0010-4655 (cit. on pp. 15, 31, 33).

[Par+12] M. L. Parks et al. *Peridigm Users’ Guide*. Tech. rep. SAND2012-7800. Sandia National Laboratories, 2012 (cit. on p. 61).

[Pfl10] Dirk Pflüger. *Spatially Adaptive Sparse Grids for High-Dimensional Problems*. München: Verlag Dr. Hut, Aug. 2010. ISBN: 9783868535556 (cit. on p. 78).

[Pfl12] Dirk Pflüger. “Spatially Adaptive Refinement.” In: *Sparse Grids and Applications*. Ed. by Jochen Garcke and Michael Griebel. Lecture Notes in Computational Science and Engineering. Berlin Heidelberg: Springer, Oct. 2012, pp. 243–262 (cit. on p. 78).

[Pli95] S. Plimpton. “Fast Parallel Algorithms for Short-Range Molecular Dynamics.” In: *Journal of Computational Physics*. 117. 1995, pp. 1–19 (cit. on pp. 44, 82).

[PM14] P. Diehl and M. A. Schweitzer. “Efficient Neighbor Search for Particle Methods on GPUs.” In: *Meshfree Methods for Partial Differential Equations VII*. Ed. by M. Griebel and M. A. Schweitzer. Vol. 100. Lecture Notes in Computational Science and Engineering. Springer, 2014 (cit. on pp. 4, 44, 49).

[PM15] P. Diehl and M. A. Schweitzer. “Simulation of wave propagation and impact damage in brittle materials using peridynamics.” In: *Recent Trends in Computational Engineering – CE2014*. Ed. by Miriam Mehl, Manfred Bischoff, and Michael Schäfer. Lecture Notes in Computational Science and Engineering. Springer, 2015 (cit. on p. 4).

[R+07] Johnson G. R. et al. “A quantitative Assesment of computational results for behind armor Debris.” In: 23^{rd} *International Symposium On Ballistics*. Apr. 2007 (cit. on p. 61).

[Red05] J Reddy. *An Introduction to the Finite Element Method (Mcgraw Hill Series in Mechanical Engineering)*. 3rd ed. McGraw-Hill Education, Jan. 2005. ISBN: 9780072466850 (cit. on p. 7).

[Red13] J. N. Reddy. *An Introduction to Continuum Mechanics*. 2nd ed. Cambridge University Press, July 2013. ISBN: 9781107025431 (cit. on p. 8).

[RHT10] W Riedel, S. Hiermaier, and K Thoma. “Transient stress and failure analysis of impact experiments with ceramics.” In: *Materials Science and Enginnering B*. Vol. 173. ELSEVIER, 2010, pp. 139–147 (cit. on pp. 72, 77).

[Roy08] David Roylance. *Mechanical Properties of Materials*. Lecutre Notes at the Massachusetts Institute of Technology. 2008 (cit. on p. 96).

[SA05] S.A. Silling and E. Askari. “A meshfree method based on the peridynamic model of solid mechanics.” In: 83 (Mar. 2005). Ed. by ELSEVIER, pp. 1526–1535 (cit. on pp. 75, 77, 82, 85, 89).

[SA08] Erik Sintorn and Ulf Assarsson. “Fast parallel GPU-sorting using a hybrid algorithm.” In: *Journal of Parallel and Distributed Computing*. Vol. 68. 10. Oct. 2008 (cit. on p. 49).

[Sar+16] G. Sarego et al. “Linearized state-based peridynamics for 2-D problems.” In: *International Journal for Numerical Methods in Engineering* (2016). ISSN: 1097-0207 (cit. on pp. 83, 98).

[Sch39] H. Schradin. “Physikalische Vorgänge bei hohen Belastungen und Belastungsgeschwindigikeiten (Physical Processes at High Loadings and Loading Rates).” In: *Scripts for German Academy for Aeronautical Research*. Vol. 40. 1939, pp. 21–68 (cit. on pp. 71–73).

[SDP16] Pablo Seleson, Qiang Du, and Michael L. Parks. “On the consistency between nearest-neighbor peridynamic discretizations and discretized classical elasticity models.” In: *Computer Methods in Applied Mechanics and Engineering* 311 (2016), pp. 698–722. ISSN: 0045-7825 (cit. on p. 37).

[Sel+09] Pablo Seleson et al. “Peridynamics as an Upscaling of Molecular Dynamics.” In: *Multiscale Model. Simul.* Vol. 8. 1. Society for Industrial and Applied Mathematics, 2009, pp. 204–227 (cit. on p. 8).

[Sel14] Pablo Seleson. “Improved one-point quadrature algorithms for two-dimensional peridynamic models based on analytical calculations.” In: *Computer Methods in Applied Mechanics and Engineering* 282 (2014), pp. 184–217. ISSN: 0045-7825 (cit. on pp. 33, 82, 83).

[SH05] Schram; S.J. and Meyer H.W. *Simulating the formation and evolution of behind armor debris fields*. ARL-RP 109. U.S. Army Research Laboratory, 2005 (cit. on pp. 44, 60–62).

[SHG09] Nadathur Satish, Mark Harris, and Michael Garland. “Designing Efficient Sorting Algorithms for Manycore GPUs.” In: *IEEE International Symposium in Parallel and Distributed Processing*. 2009, pp. 1–10 (cit. on p. 49).

[Sil+07] S. A. Silling et al. “Peridynamic States and Constititive Modeling.” In: *Journal of Elasticity*. Vol. 88. Springer Science + Business Media B. V., 2007, pp. 151–184 (cit. on pp. 14, 39).

[Sil00] S.A. Silling. “Reformulation of elasticity theory for discontinuities and long-range forces.” In: *Journal of the Mechanics and Physics of Solids* 48.1 (2000), pp. 175–209. ISSN: 0022-5096 (cit. on pp. 8, 12).

[Sil11] Stewart A. Silling. “A coarsening method for linear Peridynamics.” In: *International Journal for Multiscale Computational Engineering* 9.6 (2011), pp. 609–622. ISSN: 1543-1649 (cit. on pp. 38, 75, 77, 82, 85, 89).

[Sil16a] Stewart A. Silling. “Handbook of Peridynamic Modeling.” In: ed. by Florin Bobaru et al. CRC Press, Sept. 2016. Chap. Introduction to Peridynamics, pp. 26–58 (cit. on pp. 12, 14, 99).

[Sil16b] Stewart A. Silling. “Handbook of Peridynamic Modeling.” In: ed. by Florin Bobaru et al. CRC Press, Sept. 2016. Chap. Why Peridynamics, pp. 3–22 (cit. on p. 14).

[SL08] S. A. Silling and R. B. Lehoucq. “Convergence of Peridynamics to Classical Elasticity Theory.” In: *Journal of Elasticity* 93.1 (2008), pp. 13–37. ISSN: 1573-2681 (cit. on p. 14).

[SL10] SA Silling and RB Lehoucq. “Peridynamic theory of solid mechanics.” In: *Advances in Applied Mechanics* 44 (2010), pp. 73–168 (cit. on p. 36).

[SP16] Pablo Seleson and Michael L. Parks. “Handbook of Peridynamic Modeling.” In: ed. by Florin Bobaru et al. CRC Press, Sept. 2016. Chap. Links between Peridynamic and Atomistic Models, pp. 181–202 (cit. on p. 8).

[SSL13] Yaroslav D. Sergeyev, Roman G. Strongin, and Daniela Lera. *Introduction to Global Optimization Exploiting Space-Filling Curves*. Springer, 2013, p. 136 (cit. on p. 45).

[Ste16] Ste||ar Group. *HPXCL*. `https://github.com/STEllAR-GROUP/hpxcl`. Nov. 2016 (cit. on p. 4).

[Str+05] E. Strassburger et al. “Visualization of wave propagation and impact damage in a polycrystalline transparent ceramic - AlON.” In: *22nd International Symposium on Ballistics*. 2. DEStech Publications, Nov. 2005, pp. 769–776 (cit. on pp. 73, 74, 77).

[Str+06] E. Strassburger et al. “High-Speed Photographic Study Of Wave Propagation And Iimpact Damage In Fused Silcia And Alon Using The Edge-On Impact (EOI) Method.” In: *AIP Conf. Proc.* 892 (2006) (cit. on pp. 73, 74, 77).

[Str04] E. Strassburger. “Visualization of Impact Damage in Ceramics Using the Edge-On Impact Technique.” In: *International Journal of Applied Ceramic Technology*. Vol. 1. 2004, 1:235–242 (cit. on pp. 71–73).

[SW14] M. A. Schweitzer and S. Wu. “A Moving Least Squares Approach to the Construction of Discontinuous Enrichment Functions.” In: *Singular Phenomena and Scaling in Mathematical Models*. Ed. by Michael Griebel. Springer International Publishing, 2014, pp. 347–360. ISBN: 9783319007854 (cit. on p. 43).

[TD13] Xiaochuan Tian and Qiang Du. “Analysis and Comparison of Different Approximations to Nonlocal Diffusion and Linear Peridynamic Equations.” In: *SIAM Journal on Numerical Analysis* 51.6 (2013), pp. 3458–3482 (cit. on pp. 38, 78, 85).

[TD14] Xiaochuan Tian and Qiang Du. “Asymptotically compatible schemes and applications to robust discretization of nonlocal models.” In: *SIAM Journal on Numerical Analysis* 52.4 (2014), pp. 1641–1655 (cit. on pp. 37, 38).

[TH81] H. Tropf and H. Herzog. “Multidimensional Range Search in Dynamically Balanced Trees.” In: *Angewandte Informatik (Applied Informatics)*. Vieweg Verlag, Feb. 1981, pp. 71–77 (cit. on pp. 44, 46).

[TPM09] Aidan P. Thompson, Steven J. Plimpton, and William Mattson. “General formulation of pressure and stress tensor for arbitrary many-body interaction potentials under periodic boundary conditions.” In: *The Journal of Chemical Physics* 131.15, 154107 (2009) (cit. on p. 81).

[Vog+03] Tracy J. Vogler et al. “Fragmentation of Materials In Expanding Tube Experiments.” In: *International Journal of Impact Engineering* 29.1–10 (2003). Hypervelocity Impact, pp. 735–746. ISSN: 0734-743X (cit. on pp. 44, 60–62).

[WE05] Olaf Weckner and Etienne Emmrich. “Numerical simulation of the dynamics of a nonlocal, inhomogeneous, infinite bar.” In: *Journal of Computational and Applied Mechanics* 6.2 (2005), pp. 311–319 (cit. on p. 31).

[Wen11] Wen-mei W. *GPU Computing Gems Emerald Edition (Applications of GPU Computing Series)*. 1st ed. Morgan Kaufmann, Feb. 2011 (cit. on p. 49).

[WS93] M. S. Warren and J. K. Salmon. “A Parallel Hashed Oct-Tree N-body Algorithm.” In: *Proceedings of the 1993 ACM/IEEE Conference on Supercomputing*. Supercomputing ’93. Portland, Oregon, USA: ACM, 1993, pp. 12–21. ISBN: 0818643404 (cit. on p. 45).

[WSR89] S. Winkler, H. Senf, and H. Rothenhausler. *Wave and Fracture Phenomena in Impacted Ceramics*. EMI-Report V5/89. Fraunhofer-Institut für Werkstoffmechanik Freiburg, 1989 (cit. on pp. 60, 71, 72).

[ZD10] Kun Zhou and Qiang Du. "Mathematical and numerical analysis of linear peridynamic models with nonlocal boundary conditions." In: *SIAM Journal on Numerical Analysis* 48.5 (2010), pp. 1759–1780 (cit. on pp. 36, 37).

[ZJH11] Xiaotian ZHANG, Guanghui JIA, and Hai HUANG. "Fragment Identification and Statistics Method of Hypervelocity Impact SPH Simulation." In: *Chinese Journal of Aeronautics* 24.1 (2011), pp. 18–24. ISSN: 1000-9361 (cit. on p. 61).

[ZM02] Bazant Z.P. and Jirasèk M. "Nonlocal Integral Formulations of Plasticity and Damage: Survey of Progress." In: *Journal of Engineering Mechanics* 128.11 (2002), pp. 1119–1149 (cit. on p. 8).

Index